

中国科学技术大学

博士学位论文



利用 ATLAS 探测器上 ZZ 玻色子到全 轻子通道的衰变事例进行电弱对称性破 缺的研究

作者姓名： 祝鹤龄

学科专业： 粒子与原子核物理

导师姓名： 赵政国 马宏

完成时间： 二〇二〇年六月二十六日

University of Science and Technology of China
A dissertation for doctor's degree



**Study of Electroweak Symmetry
Breaking in ZZ Production in Purely
Leptonic Decay with ATLAS Detector**

Author: Heling Zhu

Speciality: Particle and Nuclear Physics

Supervisors: Zhengguo Zhao, Hong Ma

Finished time: June 26, 2020

中国科学技术大学学位论文原创性声明

本人声明所呈交的学位论文，是本人在导师指导下进行研究工作所取得的成果。除已特别加以标注和致谢的地方外，论文中不包含任何他人已经发表或撰写过的研究成果。与我一同工作的同志对本研究所做的贡献均已在论文中作了明确的说明。

作者签名：_____

签字日期：_____

中国科学技术大学学位论文授权使用声明

作为申请学位的条件之一，学位论文著作权拥有者授权中国科学技术大学拥有学位论文的部分使用权，即：学校有权按有关规定向国家有关部门或机构送交论文的复印件和电子版，允许论文被查阅和借阅，可以将学位论文编入《中国学位论文全文数据库》等有关数据库进行检索，可以采用影印、缩印或扫描等复制手段保存、汇编学位论文。本人提交的电子文档的内容和纸质论文的内容相一致。

保密的学位论文在解密后也遵守此规定。

公开 保密（____ 年）

作者签名：_____

导师签名：_____

签字日期：_____

签字日期：_____

摘要

中文摘要

关键词:

ABSTRACT

English abstract.

Key Words:

Acknowledgments

Contents

Acknowledgments	III
Chapter 1 Introduction	1
Chapter 2 Theory	3
2.1 The Standard Model of Particle Physics	3
2.1.1 Elementary particles in the Standard Model	3
2.1.2 Electroweak theory	5
2.1.3 Higgs mechanism and Electroweak symmetry breaking	6
2.2 Phenomenology of Large Hadron Collider	9
2.2.1 Physics at hadronic collision	9
2.2.2 Higgs physics at the LHC	12
2.2.3 Diboson physics	13
Chapter 3 The Large Hadron Collider and the ATLAS Detector	18
3.1 The Large Hadron Collider	18
3.1.1 Operation history and machine layout	18
3.1.2 Luminosity and pile-up	21
3.2 ATLAS detector	22
3.2.1 Detector overview	22
3.2.2 Physics requirement	24
3.2.3 Magnet system	25
3.2.4 Inner detector	26
3.2.5 Calorimeters	28
3.2.6 Muon spectrometer	30
3.2.7 Trigger system	32
Chapter 4 Simulation and Event Reconstruction for the ATLAS Experiment	36
4.1 Event simulation	36
4.2 Event reconstruction	39
4.2.1 Track	39
4.2.2 Primary vertex	41
4.2.3 Electron	42
4.2.4 Muon	46

4.2.5	Jets	52
4.2.6	Missing transverse energy	55
Chapter 5	Observation of electroweak $Z Z$ production and measurement of the SM $Z Z$ cross section in the $\ell \ell \ell \ell$ final state using pp collisions data collected by ATLAS detector from 2015–2018	58
5.1	Introduction	58
5.2	Data and MC samples	59
5.2.1	Data samples	59
5.2.2	MC simulations	60
5.3	Objects and Event selection	61
5.3.1	Objects selection	61
5.3.2	Event selection in reconstruction level	62
5.4	Background estimation	63
5.4.1	QCD backgrounds	64
5.4.2	Reducible backgrounds	64
5.5	Systematics	69
5.5.1	Theoretical systematics	69
5.5.2	Experimental systematics	70
5.6	Measurement of fiducial cross section	73
5.6.1	Calculation of C-factor	73
5.6.2	Result of fiducial cross section	74
5.7	Search for EW- $Z Z jj$	74
5.7.1	MD discriminant	74
5.7.2	Profile likelihood ratio method	76
5.7.3	Fitting procedure	77
5.7.4	Result of statistical fit	78
5.8	Prospect study of EW- $Z Z jj$ production in HL-LHC	78
5.8.1	Introduction	78
5.8.2	The ATLAS detector at HL-LHC	80
5.8.3	Simulation	80
5.8.4	Event selection	81
5.8.5	Systematics	82
5.8.6	Results	84
5.9	Conclusion	86

Chapter 6	Search for heavy ZZ resonances in the $\ell\ell\ell\ell$ final state using pp collisions data collected by ATLAS detector from 2015–2018	87
6.1	Introduction	87
6.2	Data and MC samples	88
6.2.1	Data samples	88
6.2.2	Background MC simulations	88
6.2.3	Signal MC simulations	89
6.3	Analysis selections	90
6.3.1	Objects selection	90
6.3.2	Event selection	91
6.3.3	Event categorizations	93
6.3.4	Signal acceptance	99
6.4	Background estimation	100
6.4.1	Irreducible backgrounds	101
6.4.2	Reducible backgrounds	102
6.5	Signal modelling	106
6.5.1	Modelling of narrow-width signal	106
6.5.2	Modelling of large-width signal	109
6.5.3	Modelling of interference	110
6.5.4	Modelling of spin-2 RS Graviton signal	115
6.6	Systematic uncertainties	117
6.6.1	Theoretical uncertainties	117
6.6.2	Experimental systematics	119
6.7	Results in $\ell\ell\ell\ell$ channel	119
6.7.1	Statistical procedure	119
6.7.2	Likelihood fit under background-only hypothesis for DNN-based analysis	120
6.7.3	Interpretations	123
6.8	Conclusion	128
	Bibliography	129

Contents

test

Chapter 1 Introduction

The goal of particle physics is to understand how our universe works at its most fundamental level. It can be accomplished by pursuing the mysteries of the basic construction of matter and energy, probing the interactions between elementary particles, and exploring the basic nature of space and time itself.

Elementary particles

From around the 6th century BC, ancient Greek philosophers Leucippus, Democritus, and Epicurus brought up a philosophical idea that everything is composed of "uncuttable" elementary particles. In the 19th century, John Dalton, through his work on stoichiometry, concluded that each element of nature was composed of a single, unique type of particle. The particle was named as "atom" after the Greek word atomos, with the meaning of "in-divisible". However this Dalton's atom theory was strongly challenged later. Near the end of 19th century, physicists discovered that Dalton's atoms are not, in fact, the fundamental particles of nature, but conglomerates of even smaller particles. Electron was discovered by J. J. Thomson in 1897, and then its charge was carefully measured by Robert Andrews Millikan and Harvey Fletcher in their "oil drop experiment" of 1909. In early 20th-century, Rutherford's "gold foil experiment" showed that the atom is mainly empty space, with almost all its mass concentrated in a tiny positive charge atomic nucleus. Then the discoveries of anti-particles (the positron in 1932) and other particles (e.g. the muon in 1936) shows that more discoveries could be expected in future experiments.

Starting from 1950s, more accelerator facilities were put into service. Throughout the 1950s and 1960s, a bewildering variety of particles were found in collisions of particles from increasingly high-energy beams. It was referred to informally as the "particle zoo". In 1964, the quark model was independently proposed by physicists Murray Gell-Mann and George Zweig, and experimentally confirmed of their existence in mid-1970s. In 1970s, the establishment of quantum chromodynamics (QCD) postulated the fundamental strong interaction, experienced by quarks and mediated by gluons.

The well-known Standard model (SM) was developed in stages throughout the latter half of the 20th century. Since then, confirmation of the top quark (1995), the tau neutrino (2000), and the Higgs boson (2012) have added further credence to the Standard Model. Now, the quarks, leptons and gauge bosons are the elementary constituents in a framework of Standard Model of particle physics, which theoretically describes three of the four known fundamental forces (the electromagnetic, weak, and strong interactions,

and not including the gravitational force) in the universe, as well as classifies all known elementary particles.

Higgs mechanics and electroweak symmetry breaking

In 1961, Sheldon Glashow brought forward a unified electroweak theory to combine the electromagnetic and weak interactions. In the standard model, at energy high enough that electroweak symmetry is unbroken, all elementary particles are massless. But measurements show the fact that the W and Z bosons actually have masses. Later on, the Higgs mechanics resolves this conundrum. The simplest description of the mechanism adds a Higgs field that permeates all space to the Standard Model. Below some extremely high energy, the field causes spontaneous symmetry breaking during interactions. All massive particles in the Standard Model, including the W and Z bosons, interact with Higgs boson to acquire their mass.

Over the past few decades, with the combination of electroweak theory, Higgs mechanics and strong interactions has been widely accepted. But the Higgs boson, which is essential to explain the mechanics of the property "mass" for gauge bosons and fermions, had been the final missing piece in the Standard Model of particle physics for the time being. The mass of Higgs boson was not be specifically predicted, and it has been searched in several large experiments (eg. LEP at CERN, Tevatron at Fermilab, and LHC at CERN). In 2012, the discovery of Higgs boson was finally announced by the ATLAS and CMS collaborations at the Large Hadron Collider (LHC) with its mass round 125 GeV. Peter Higgs and Francois Englert were award the 2013's Nobel Prize in Physics for their theoretical discovery of a mechanism that contributes to our understanding of the origin of mass of subatomic particles.

Contents of this thesis

This thesis is organized as follows. Section 2 briefly introduces the Standard Model of particle physics, the Higgs mechanism related to the thesis and the LHC phenomenology. Section 3 gives an overview of the LHC and the ATLAS detector. The detector simulation and the reconstruction of physics objects are described in section 4. Section 5 focuses on the Standard model ZZ production cross section measurement in $ZZ \rightarrow 4l$ channel, and the observation of its electroweak component as well as its further prospects in High luminosity LHC (HL-LHC). Section 6 present the search of possible heavy Higgs in $H \rightarrow ZZ \rightarrow 4l$ channel. In the end, section 7 gives the summary and outlook for future physics in LHC.

Chapter 2 Theory

2.1 The Standard Model of Particle Physics

The standard model (SM) reflects our current understanding of elementary particles and several basic interactions. It is a gauge quantum field theory containing the internal symmetries of the unitary product group $SU(3) \times SU(2) \times U(1)$, in which the color group $SU(3)$ presents the strong interaction, and $SU(2) \times U(1)$ describes the electroweak interactions. Over the past decades, the SM has been widely tested through various experiments with extremely high precision.

2.1.1 Elementary particles in the Standard Model

The elementary particles in SM can be classified into 3 class: *fermions*, *gauge bosons* and the *Higgs boson* as shown in Figure 2.1.

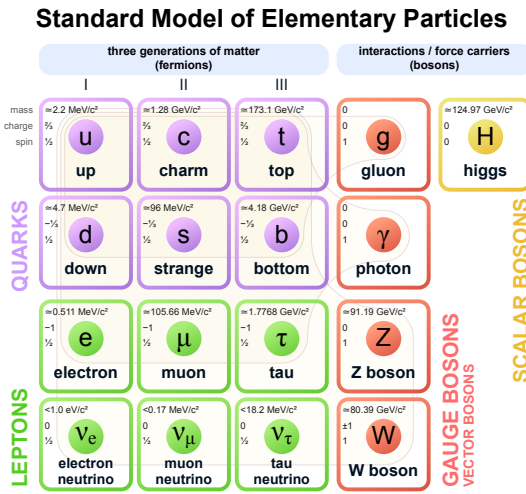


Fig. 2.1 The elementary particles of the Standard Model.

Fermions The Standard Model includes 12 elementary particles of spin- $\frac{1}{2}$ obeying the Fermi-Dirac statistics, known as fermions. They are classified into two types: *leptons* and *quarks* according to their interactions. The *leptons* include three generations: electron (e) and electron neutrino (ν_e); muon (μ) and muon neutrino (ν_μ); tau (τ) and tau neutrino (ν_τ). The e , μ and τ carry electric charge of -1 and three neutrinos are electrically neutral. All the leptons can participate in electroweak interactions. Also there are three generations of *quarks*: up (u) and down (d); charm (c) and strange (s); top (t) and bottom (b). The defining property of the quarks is that they carry color charge (while leptons don't), and hence interact via the strong interaction, letting them to be strongly bound from one to

another, forming color-neutral composite particles (hadrons) containing either a quark and an antiquark (mesons) or three quarks (baryons). In the meantime, u, c and t-quark carry electric charge of $2/3$, and d, s and b-quark carry electric charge of $-1/3$. Hence they interact via all three interactions described in SM. Each fermion also has a corresponding antiparticles.

Gauge bosons act as force carriers that mediate the strong, weak, and electromagnetic interactions in SM. They are spin-1 particles obeying the Bose-Einstein statistics. There are three types of gauge bosons:

- The eight massless *gluons* mediate the strong interactions between color charged particles (the quarks).
- The massless *photons* mediate the electromagnetic force between electrically charged particles.
- The W^+, W^- and Z bosons mediate the weak interactions between particles of different flavors (all quarks and leptons). All these three bosons are massive, the W^\pm carries an electric charge of $+1$ and -1 and couples to the electromagnetic interaction. Z boson is electrically neutral.

Figure 2.2 shows the Feynman diagrams of corresponding interactions in SM.

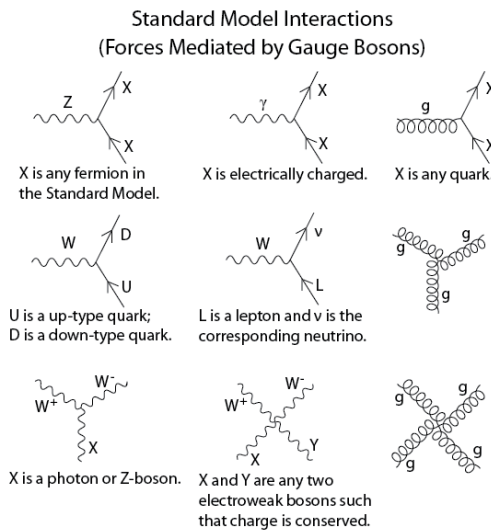


Fig. 2.2 The Feynman diagrams of interactions that form the basis of the standard model.

Higgs boson is a massive scalar elementary particle with spin-0. It plays a unique role in the SM by explaining the origin of masses of massive gauge bosons (W^\pm and Z) and fermions. And it is the last discovered particle in SM.

2.1.2 Electroweak theory

The electroweak interaction is the unified description of two of the four known fundamental interactions of nature: electromagnetism and the weak interaction. It is based on the gauge group of $SU(2)_L \times SU(1)_Y$, in which L is the left-handed fields and Y is the weak hypercharge^[1]. It follows the Lagrangian of

$$L_{EW} = L_{gauge} + L_{Higgs} + L_{fermion} + L_{Yukawa} \quad (2.1)$$

L_{gauge} is the **gauge term** part

$$L_{gauge} = -\frac{1}{4}W_{\mu\nu}^i W^{\mu\nu i} - \frac{1}{4}B_{\mu\nu} B^{\mu\nu} \quad (2.2)$$

where W_μ^i and B_μ respectively present the $SU(2)_L$ and $SU(1)_Y$ gauge fields, with the corresponding field strength tensors of

$$\begin{aligned} B_{\mu\nu} &= \partial_\mu B_\nu - \partial_\nu B_\mu \\ W_{\mu\nu}^i &= \partial_\mu W_\nu^i - \partial_\nu W_\mu^i - g\epsilon_{ijk}W_\mu^j W_\nu^k \end{aligned} \quad (2.3)$$

In the equations above, g is the $SU(2)_L$ gauge coupling and ϵ_{ijk} is the totally antisymmetric tensor. The gauge Lagrangian has three and four-point self interactions of W^i , which result in triple and quartic gauge boson couplings.

The second term of the Lagrangian is the **scalar part**:

$$L_{Higgs} = (D^\mu \phi)^\dagger D_\mu \phi - V(\phi) \quad (2.4)$$

where $\phi = \begin{pmatrix} \phi^+ \\ \phi^0 \end{pmatrix}$ is a complex Higgs scalar, and $V(\phi)$ is the Higgs potential which is restricted into the form of

$$V(\phi) = +\mu^2 \phi^\dagger \phi + \lambda (\phi^\dagger \phi)^2 \quad (2.5)$$

due to the combination of $SU(2)_L \times SU(1)_Y$ invariance and renormalizability. In Eq. 2.5, μ is a mass-dependent parameter and λ is the quartic Higgs scalar coupling, which represents a quartic self-interaction between the scalar fields. When $\mu^2 < 0$, there will be spontaneous symmetry breaking (more details in section 2.1.3). To maintain vacuum stability, $\lambda > 0$ is required. And in Eq. 2.4, the gauge covariant derivative is defined as

$$D_\mu \phi = \left(\partial_\mu + ig \frac{\tau^i}{2} W_\mu^i + \frac{ig'}{2} B_\mu \right) \phi \quad (2.6)$$

in which τ^i represents the Pauli matrices, and g' is the $U(1)_Y$ gauge coupling. The square

of the covariant derivative results in three and four-point interactions between the gauge and scalar fields.

The third term of the Lagrangian is the **fermion part**

$$L_{fermion} = \sum_{m=1}^F (\bar{q}_{mL}^0 \gamma_\mu D_\mu q_{mL}^0 + \bar{l}_{mL}^0 \gamma_\mu D_\mu l_{mL}^0 + \bar{u}_{mR}^0 \gamma_\mu D_\mu u_{mR}^0 + \bar{d}_{mR}^0 \gamma_\mu D_\mu d_{mR}^0 + \bar{e}_{mR}^0 \gamma_\mu D_\mu e_{mR}^0 + \bar{\nu}_{mR}^0 \gamma_\mu D_\mu \nu_{mR}^0) \quad (2.7)$$

In Eq. 2.7, m is the family index of fermions, F is the number of families. The subscripts L(R) stand for the left (right) chiral projection $\psi_{L(R)} \equiv (1 \mp \gamma_5) \psi/2$.

$$q_{mL}^0 = \begin{pmatrix} u_m^0 \\ d_m^0 \end{pmatrix}_L \quad l_{mL}^0 = \begin{pmatrix} v_m^0 \\ e_m^{-0} \end{pmatrix}_L \quad (2.8)$$

are the $SU(2)$ doublets of left-hand quarks and leptons, while u_{mR}^0 , d_{mR}^0 , e_{mR}^{-0} and ν_{mR}^0 are the right-hand singlets.

The last term in Eq. 2.1 is **Yukawa term**

$$L_{Yukawa} = - \sum_{m,n=1}^F [\Gamma_{mn}^u \bar{q}_{mL}^0 \tilde{\phi} u_{nR}^0 + \Gamma_{mn}^d \bar{q}_{mL}^0 \phi d_{nR}^0 + \Gamma_{mn}^e \bar{l}_{mL}^0 \phi e_{nR}^0 + \Gamma_{mn}^\nu \bar{l}_{mL}^0 \tilde{\phi} \nu_{nR}^0] + h.c. \quad (2.9)$$

the matrices Γ_{mn} refer to the Yukawa couplings between single Higgs doublet (ϕ) and the various flavors of quarks (m) and leptons (n).

2.1.3 Higgs mechanism and Electroweak symmetry breaking

As shown in previous subsection, the Lagrangian L_{gauge} does not involve any mass term due to the requirement of gauge invariance. So all the W and B bosons should be massless. But experimental observations show that the gauge bosons are massive. Therefore, the gauge invariance must be broken spontaneously. The Higgs field is introduced to break the $SU(2)_L \times U(1)_Y$ symmetry and gauge bosons and fermions can interact with Higgs field to acquire their masses. And this specific process is named *Higgs mechanism* in SM.

The Higgs field ϕ is a doublet and can be written in a Hermitian basis as

$$\phi = \begin{pmatrix} \phi^+ \\ \phi^0 \end{pmatrix} = \frac{1}{\sqrt{2}} \begin{pmatrix} \phi_1 - i\phi_2 \\ \phi_3 - i\phi_4 \end{pmatrix} \quad (2.10)$$

where $\phi_i = \phi_i^+$ stand for four Hermitian field. In this new basis, the Higgs potential in

Eq. 2.5 can be expressed as:

$$V(\phi) = \frac{1}{2}\mu^2 \left(\sum_{i=1}^4 \phi_i^2 \right) + \frac{1}{4}\lambda \left(\sum_{i=1}^4 \phi_i^2 \right)^2 \quad (2.11)$$

To simplify the situation, the axis in this four-dimensional space can be chosen to satisfy $\langle 0 | \phi_i | 0 \rangle = 0$ for $i = 1, 2, 4$, and $\langle 0 | \phi_3 | 0 \rangle = v$. Thus,

$$V(\phi) \rightarrow V(v) = \frac{1}{2}\mu^2 v^2 + \frac{1}{4}\lambda v^4 \quad (2.12)$$

The minimization of this potential depends on the sign of μ^2 as shown in figure 2.3. When $\mu^2 > 0$ the minimum occurs at $v = 0$, namely the vacuum is empty space and $SU(2)_L \times U(1)_Y$ symmetry is unbroken. In the case of $\mu^2 < 0$, the $v = 0$ symmetric point is no longer stable and the minimum occurs at nonzero value of $v = (-\mu^2/\lambda)^{1/2}$ which breaks the $SU(2)_L \times U(1)_Y$ symmetry. Thus, the classical vacuum ϕ_0 of Higgs doublet can be

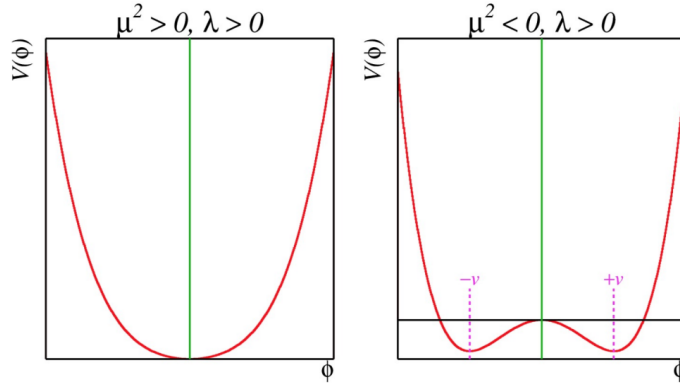


Fig. 2.3 The Higgs potential $V(\phi)$ with $\mu^2 > 0$ (left) and $\mu^2 < 0$ (right).

expressed by

$$\phi_0 = \frac{1}{\sqrt{2}} \begin{pmatrix} 0 \\ v \end{pmatrix} \quad (2.13)$$

And to quantize around the classical vacuum in a general form:

$$\phi = \frac{1}{\sqrt{2}} \begin{pmatrix} 0 \\ v + H \end{pmatrix} \quad (2.14)$$

Where H is a Hermitian field for physical Higgs scalar. In this gauge, the Lagrangian

L_{Higgs} in Eq. 2.4 takes a simple form

$$\begin{aligned} L_{Higgs} &= (D^\mu \phi)^\dagger D_\mu \phi - V(\phi) \\ &= M_W^2 W^{\mu+} W_\mu^- \left(1 + \frac{H}{v}\right)^2 + \frac{1}{2} M_Z^2 Z^\mu Z_\mu \left(1 + \frac{H}{v}\right)^2 \\ &\quad + \frac{1}{2} (\partial_\mu H)^2 - V(\phi) \end{aligned} \quad (2.15)$$

where the W and Z fields are

$$\begin{aligned} W^\pm &= \frac{1}{\sqrt{2}} (W^1 \mp iW^2) \\ Z &= -\sin\theta_W B + \cos\theta_W W^3 \end{aligned} \quad (2.16)$$

Therefore, in Eq. 2.15 spontaneous symmetry breaking brings out masses for the W and Z gauge bosons

$$\begin{aligned} M_W &= \frac{gv}{2} \\ M_Z &= \sqrt{g^2 + g'^2} \frac{v}{2} = \frac{M_W}{\cos\theta_W} \end{aligned} \quad (2.17)$$

where θ_W is the weak angle defined as

$$\sin\theta_W = \frac{g'}{\sqrt{g^2 + g'^2}} \quad \cos\theta_W = \frac{g}{\sqrt{g^2 + g'^2}} \quad \tan\theta_W = \frac{g'}{g} \quad (2.18)$$

Then another gauge boson photon remains massless with the field of

$$A = \cos\theta_W B + \sin\theta_W W^3 \quad (2.19)$$

After the symmetry breaking, the Higgs potential in unitary gauge can be written into

$$V(\phi) = -\frac{\mu^4}{4\lambda} - \mu^4 H^2 + \lambda v H^3 + \frac{\lambda}{4} H^4 \quad (2.20)$$

The first term in V is a constant, while the second term denotes a (tree-level) mass of Higgs boson

$$M_H = \sqrt{-2\mu^2} = \sqrt{2\lambda}v \quad (2.21)$$

Due to the unknown of quartic Higgs coupling λ , the Higgs mass is not predicted. The third and fourth terms in the Higgs potential V denote the induced cubic and quartic interactions of the Higgs scalar.

Through the Higgs mechanism, fermions can also acquire their masses. In the unitary

gauge, Yukawa Lagrangian (L_{Yukawa}) can be written as a simple form of^[2]

$$L_{Yukawa} = - \left(1 + \frac{H}{v} \right) (m_d \bar{d}d + m_u \bar{u}u + m_l \bar{l}l) \quad (2.22)$$

in which $m_f = \frac{y_f v}{\sqrt{2}}$ for $f = d, u, l$.

2.2 Phenomenology of Large Hadron Collider

The Large Hadron Collider (LHC) was built as a bridge between the theories and the experiment. Physicists hope that the LHC can help to answer some of the fundamental open questions in physics, concerning the basic laws of interactions and forces among the elementary particles, the deep structure of space and time, and in particular the interrelation between quantum mechanics and general relativity. This section will talk about firstly the general introduction of Physics inside hadronic collision, then followed by two important LHC phenomenology of the Higgs physics and Diboson physics which is related closely to this thesis.

2.2.1 Physics at hadronic collision

Protons are not the elementary particle, which actually be composed of quarks and gluons. So in proton-proton (pp) collision at the LHC, it is not protons themselves interact but quarks and gluons. Scattering processes can then be further classified into either *hard* or *soft* processes according to the momentum transfer during the interaction^[3]. QCD, as an underlying theory for both two process, its approach and level of understandings in two cases are quite different. For hard process, eg. Higgs, vector bosons and jets production, the rates and event properties can be precisely predicted based on perturbation theory. However, for soft processes like total cross-section, the underlying events, the rates and properties are dominated by non-perturbative QCD effects that are less understood. For many hard processes, the hard interactions are accompanied by soft ones. A example of the hadronic collision is illustrated in figure 2.4. and the typical features are summarized as below:

- **Parton Distribution Function (PDF):** $f_i(x, Q^2)$ gives the probability of a parton with flavor i (quark or gluon), carrying a momentum fraction of x and at the energy of Q in a proton. Parton distribution function cannot be fully calculated by perturbative QCD because of the inherent non-perturbative nature of partons. There are many different sets of PDFs that are determined by a fit to data from experimental observables in various processes. As an example, figure 2.5 shows

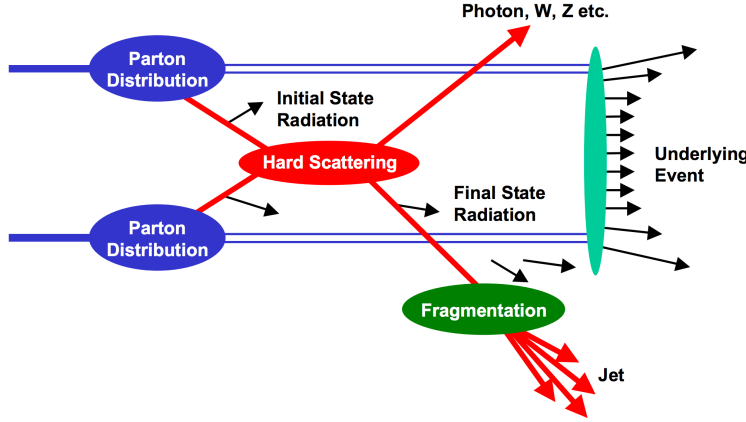


Fig. 2.4 Schematic view of a hadron-hadron collision [4].

the *PDF4LHC15 NLO PDFs*, which is based on the combination of the *CT14*, *MMHT14* and *NNPDF3.1 NNLO* PDF sets^[5].

- **Fragmentation and hadronization:** The processes to produce final state particles (or jets) from the partons produced in hard scattering.
- **Initial/Final state radiation:** The incoming and outgoing partons that carry color charge can emit QCD radiation, which gives rise to additional jets. Also the charged incoming and outgoing particles can emit Quantum Electrodynamics (QED) radiations with photons.
- **Underlying events:** Products from soft processes (not come from the primary hard scattering) as the remnants of scattering interactions.

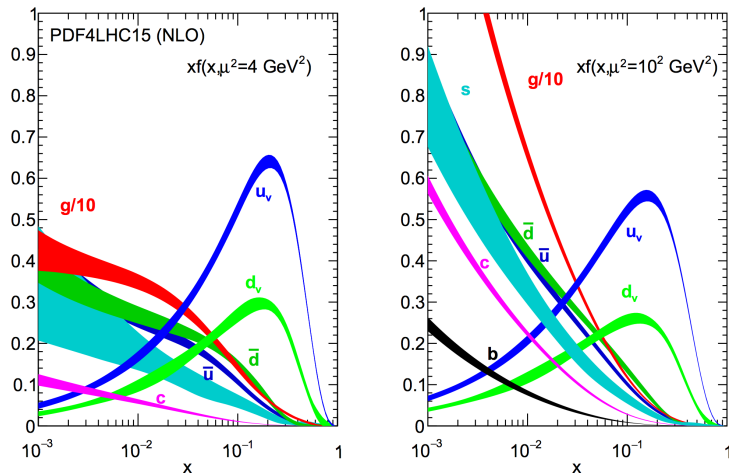


Fig. 2.5 The PDF4LHC15 NLO PDFs at a low scale $\mu^2 = Q^2 = 4 \text{ GeV}^2$ (left) and at $\mu^2 = Q^2 = 100 \text{ GeV}^2$ (right) as a function of x .

Cross section of hard scattering

According to *QCD factorization theorems*^[6], the perturbative calculations can be ap-

plied to many important hard processes involving hadrons. The basic problem addressed by factorization theorems is how to calculate high energy cross sections. Consider the process of scattering between two hardons A and B to produce a final state X, the cross section σ can be obtained by summing over all the subprocess cross section $\hat{\sigma}$ ^[7]

$$\sigma_{AB} = \int dx_a dx_b f_{a/A}(x_a) f_{b/B}(x_b) \hat{\sigma}_{ab \rightarrow X} \quad (2.23)$$

where $f_{q/A}(x_q)$ is the parton distribution functions of parton q . Taking into account the leading order correction:

$$\sigma_{AB} = \int dx_a dx_b f_{a/A}(x_a Q^2) f_{b/B}(x_b Q^2) \hat{\sigma}_{ab \rightarrow X} \quad (2.24)$$

where Q^2 represents large momentum scale that characterizes the hard scattering. Later on, since the finite corrections were not universal and had to be calculated separately for each process, the perturbative $O(\alpha_S^n)$ corrections to the leading logarithm cross section in Eq. 2.24 need to be applied, one can get:

$$\sigma_{AB} = \int dx_a dx_b f_{a/A}(x_a \mu_F^2) f_{b/B}(x_b \mu_F^2) \hat{\sigma}_{ab \rightarrow X}(\alpha_S, \mu_R, \mu_F) \quad (2.25)$$

in which μ_F is *factorization scale* which can represent the scale that separates the long- and short-distance physics, and μ_R is the *renormalization scale* for QCD running coupling. $\hat{\sigma}_{ab \rightarrow X}$ is the parton-level hard scattering cross section that can be calculated perturbatively in QCD with the form of

$$\hat{\sigma}_{ab \rightarrow X}(\alpha_S, \mu_R, \mu_F) = (\alpha_S)^n \left[\hat{\sigma}^{(0)} + (\alpha_S/2\pi) \hat{\sigma}^{(1)}(\mu_R, \mu_F) + (\alpha_S/2\pi)^2 \hat{\sigma}^{(2)}(\mu_R, \mu_F) + \dots \right] \quad (2.26)$$

where $\hat{\sigma}^{(0)}$ stands for the leading-order (LO) partonic cross section, while $\hat{\sigma}^{(1)}$ and $\hat{\sigma}^{(2)}$ are the next-to-leading-order (NLO) and next-to-next-to-leading-order (NNLO) cross section.

μ_R and μ_F depend on the order of truncation in Eq. 2.26. In principle, if cross section is calculated to all orders, it is invariant under changes in these parameters. The choices of μ_R and μ_F are arbitrary. To avoid unnaturally large logarithms reappearing in the perturbation series, it is sensible to choose μ_R and μ_F values of the order of the typical momentum scales of the hard scattering process and $\mu_R = \mu_F$ is also often assumed. Take Drell–Yan process as an example, the standard choice is $\mu_R = \mu_F = m_{ll}$, where m_{ll} is the invariant mass of di-lepton pair.

2.2.2 Higgs physics at the LHC

One important physics purpose of the LHC is searching for the Higgs boson, which was the last missing part in the SM. This section will talk about both the production and decay modes of the SM Higgs boson in proton-proton collision.

Higgs productions

The Higgs boson can be produced through several processes. There are 4 main production modes at the LHC: gluon-gluon fusion (ggF), vector boson fusion (VBF), associated production with vector-bosons (also called the Higgs Strahlung) (VH) and associated production with a pair of top/anti-top quarks (ttH)^[8]. Figure 2.6 shows the corresponding Feynman diagrams of each process (at LO). For pp collision, the cross section of produc-

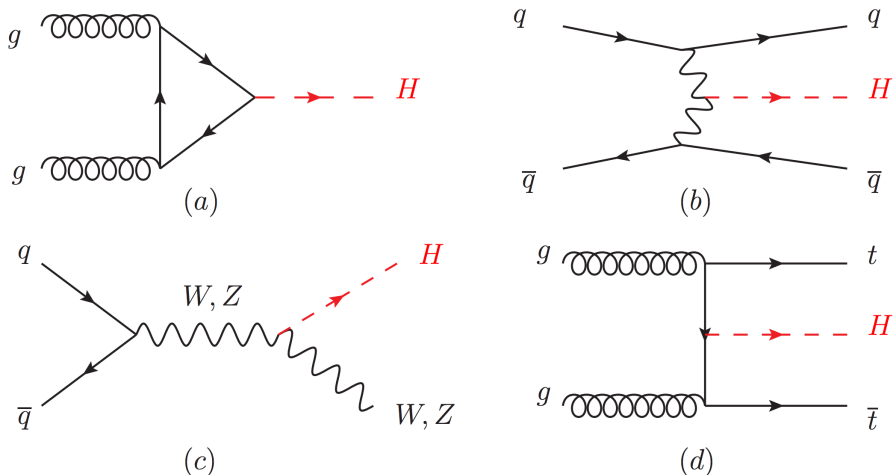


Fig. 2.6 Feynman diagrams of the Higgs production modes: (a) ggF ; (b) VBF ; (c) VH ; (d) ttH .

tions of Higgs boson is as a function of center-of-mass-energy \sqrt{s} . Figure 2.7 summarizes the cross section for SM Higgs with mass of 125 GeV.

Figure 2.8 summarizes the prospect of different Higgs boson production cross sections as a function of Higgs mass for pp collision center-of-mass-energy at 13 TeV and 14 TeV^[9].

Higgs decays

The Higgs boson can interact with gauge bosons and fermions through gauge coupling and the Yukawa coupling as introduced in section 2.1.3. Figure 2.9 depicts Feynman diagrams of possible Higgs decay channels. The branching ratio of Higgs boson decaying into different final states as a function of Higgs mass is shown in figure 2.10.

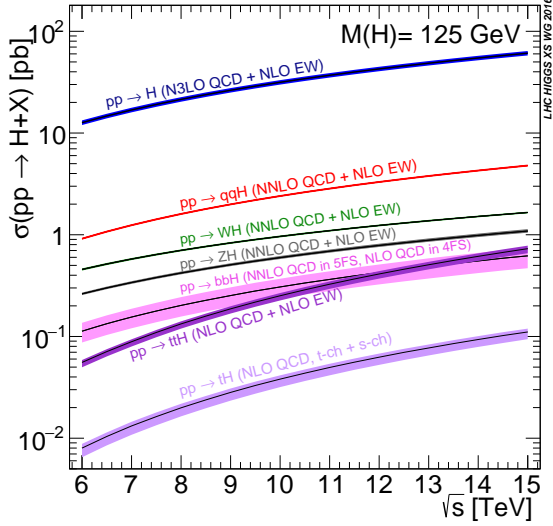


Fig. 2.7 The SM Higgs boson production cross sections as a function of the center-of-mass-energy for pp collision.

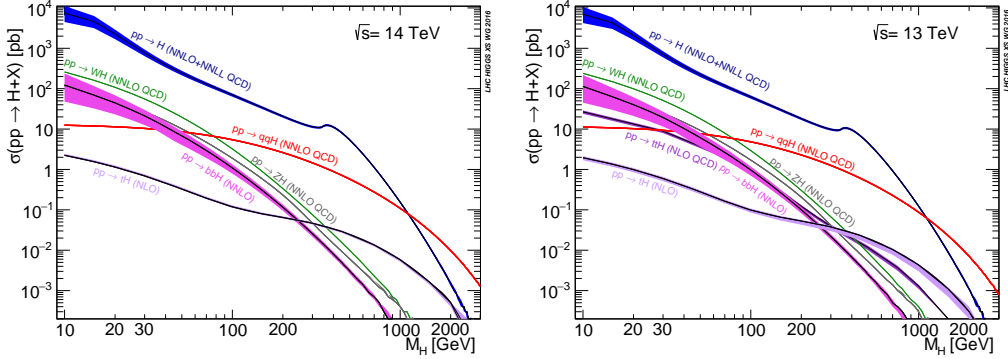


Fig. 2.8 Higgs boson production cross section for various production modes as a function of the Higgs mass for $\sqrt{s} = 13$ TeV (left) and 14 TeV (right) for pp collision.

2.2.3 Diboson physics

The study of diboson physics is another important test for SM of particle physics in electroweak sector, in which vector boson scattering is a key process for probing the mechanism of the electroweak symmetry breaking (EWSB). In the meantime, the non-resonant diboson productions are crucial backgrounds for Higgs studies at the LHC, which make the precise measurement of their cross section becomes very important.

Diboson productions

About 90% of diboson productions at hadron collider is from quark-antiquark annihilation, while others are contributed from gluon initiated process. Figure 2.11 shows the tree-level Feynman diagrams of diboson production. Then figure 2.12 illuminates the total production cross-section presented by ATLAS as a function of centre-of-mass energy \sqrt{s} from 7 to 13 TeV for several diboson processes comparing to some other major

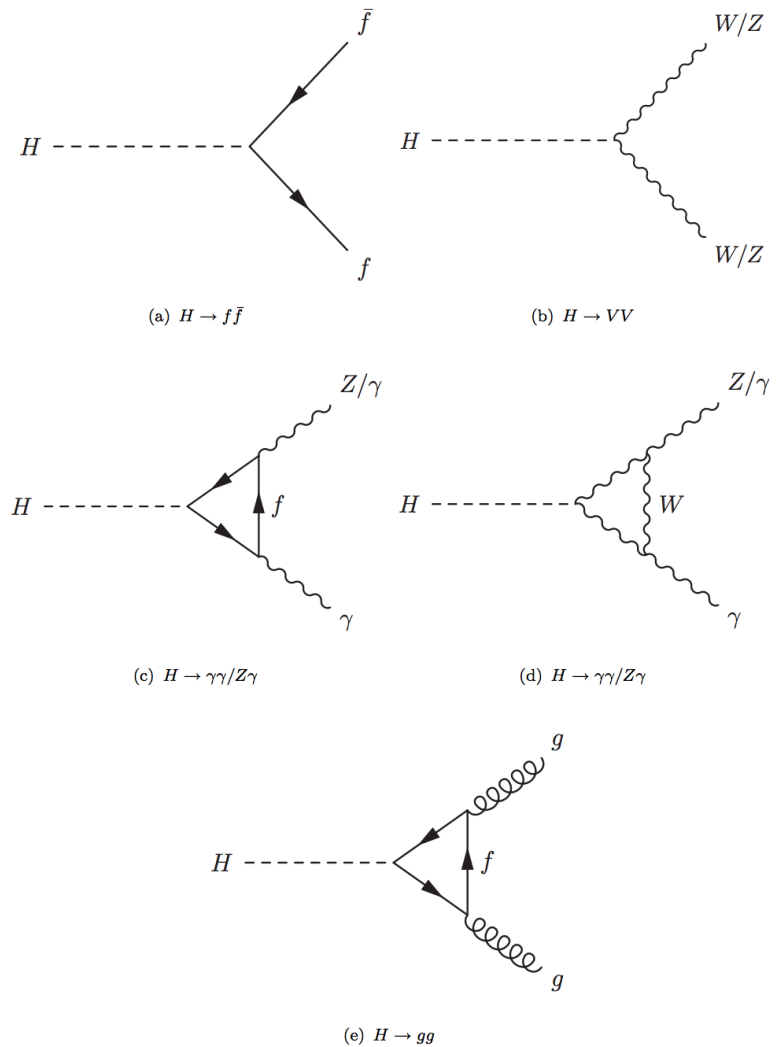
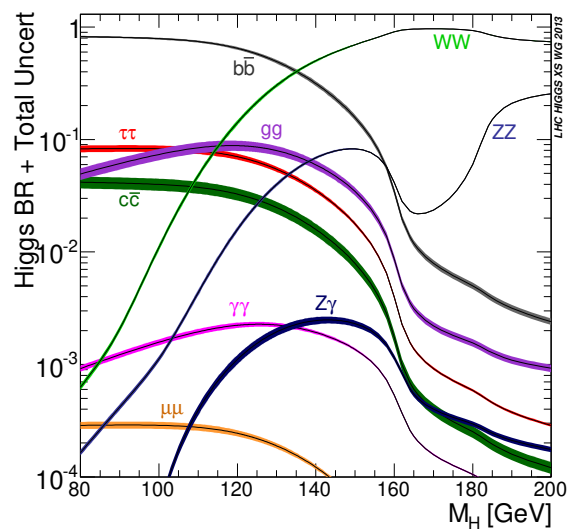


Fig. 2.9 SM Higgs decay channels.


 Fig. 2.10 Branching ratio of Higgs decays^[10].

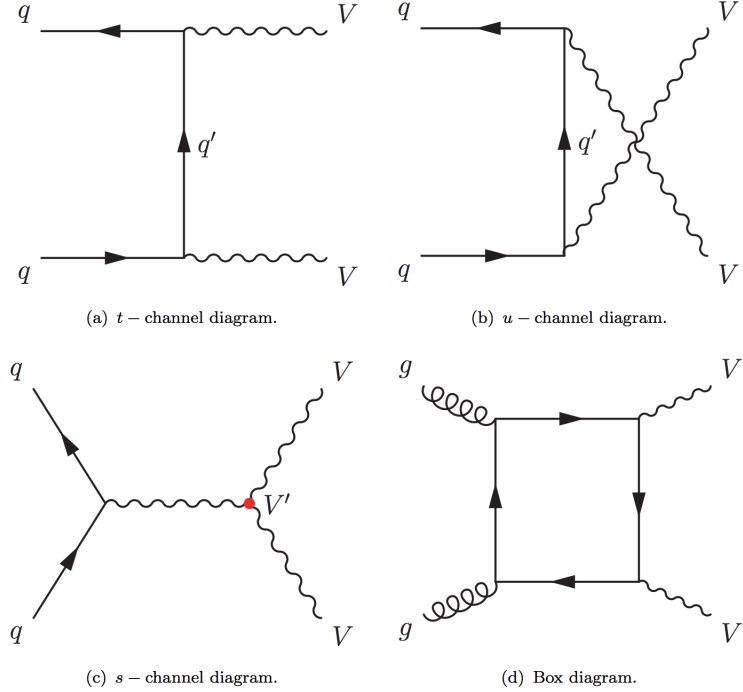


Fig. 2.11 The tree-level Feynman diagrams of diboson production at the LHC.

processes in hadron collision. The cross section for diboson processes are measured at next-to-next leading order (NNLO).

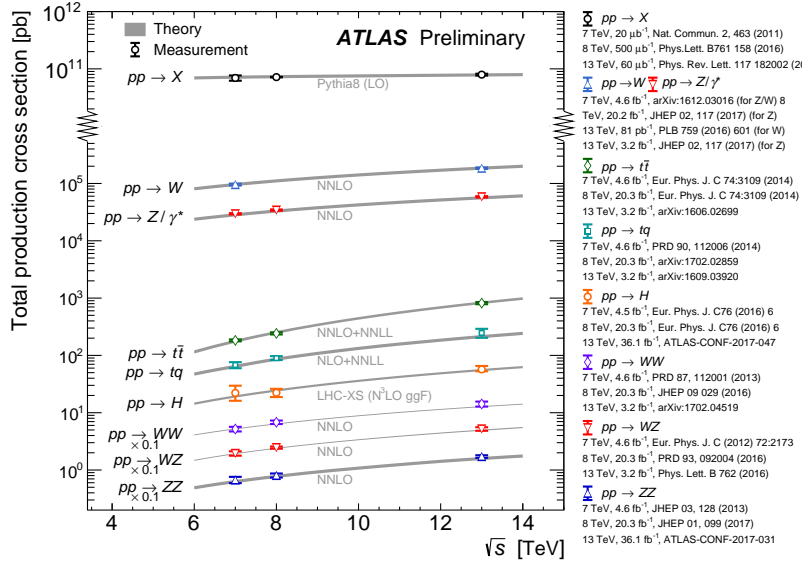


Fig. 2.12 Total production cross-section presented by ATLAS as a function of centre-of-mass energy \sqrt{s} from 7 to 13 TeV for some selected processes, the diboson measurements are scaled by a factor 0.1 to allow a presentation without overlaps.

Vector boson scattering

The $SU(2)_L \times U(1)_Y$ structure in SM predicts self-interactions between electroweak gauge bosons. Those self-couplings can involve either three or four gauge bosons at a single vertex, known as triple gauge coupling (TGC) and quartic gauge couplings (QGC),

respectively. Vector boson scattering or fusion (*VBS* or *VBF*) is carried out by four electroweak vector bosons, namely Z , W^\pm and photon (γ) as the Feynman diagrams shown in figure 2.13. And the vertexes include either those self-interactions or the interactions with the Higgs boson described in figure 2.14.

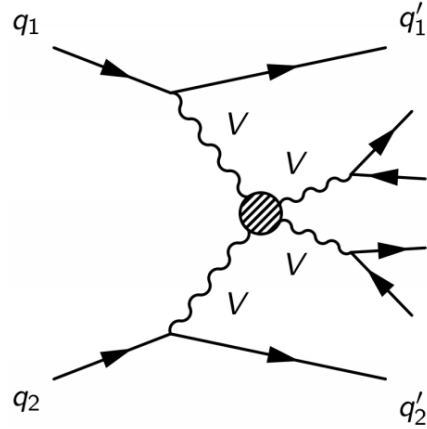


Fig. 2.13 Feynman diagrams of the vector boson scattering.

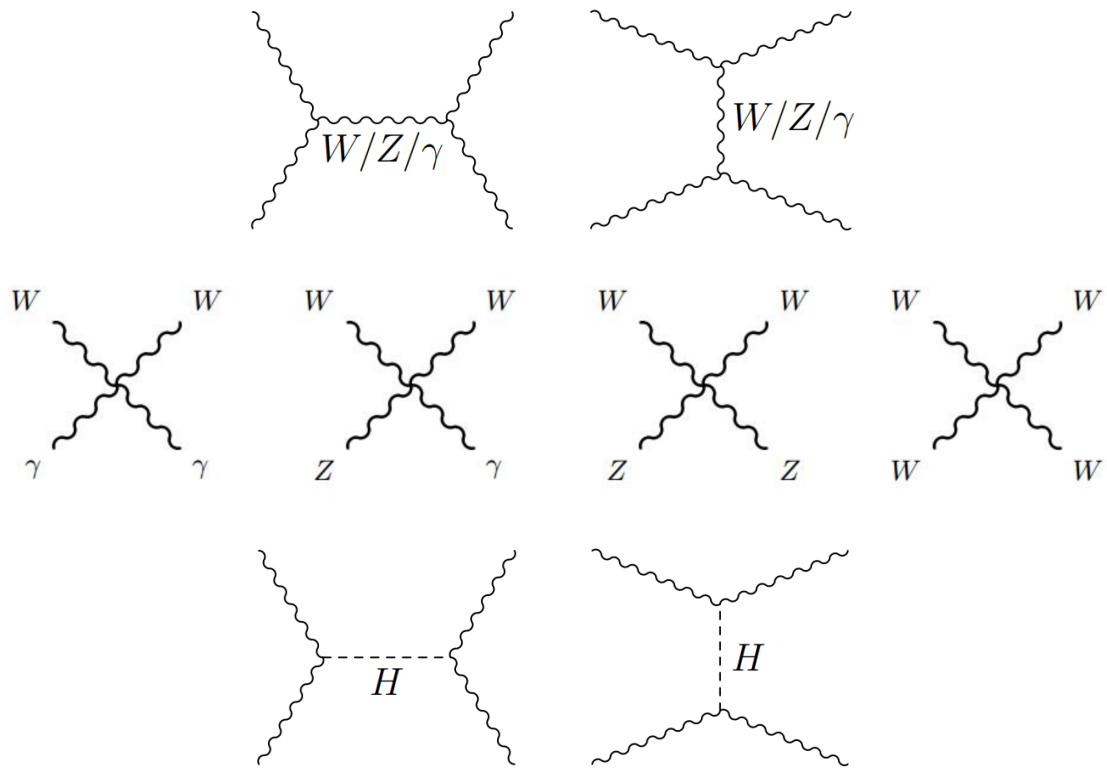


Fig. 2.14 Feynman diagrams of vertexes involving QGC, TGC and Higgs.

The amplitudes of leading-order (LO) VBS can be expressed as^[11]:

$$\begin{aligned} iM_{TGC}^{s-channel} &= -i \frac{g_1^2}{4m_W^4} [s(t-u) - 3m_W^2(t-u)] \\ iM_{TGC}^{t-channel} &= -i \frac{g_1^2}{4m_W^4} \left[(s-u)t - 3m_W^2(s-u) + \frac{8m_W^2}{s} u^2 \right] \end{aligned} \quad (2.27)$$

$$iM_{QGC} = i \frac{g_1^2}{4m_W^4} \left[s^2 + 4st + t^2 - 4m_W^2(s+t) - \frac{8m_W^2}{s} ut \right] \quad (2.28)$$

$$\begin{aligned} iM_{Higgs} &= -i \frac{C_v^2 g_1^2}{4m_W^2} \left[\frac{(s-2m_W^2)^2}{s-m_H^2} + \frac{(t-2m_W^2)^2}{t-m_H^2} \right] \\ &\simeq -i \frac{C_v^2 g_1^2}{4m_W^2} (s+t) \end{aligned} \quad (2.29)$$

Combining s- and t-channel of TGC in Eq. 2.27 and the QGC term in Eq. 2.28:

$$iM_{TGC} + iM_{QGC} = i \frac{g_1^2}{4m_W^2} (s+t) + O((s/m_W^2)^0) \quad (2.30)$$

In Eq. 2.30, the amplitude grows as a function of center-of-mass energy (\sqrt{s}), which violates the unitarity in the TeV region. Considering the Higgs term in Eq. 2.29 perfectly cancels out this growing, and the remaining term $O((s/m_W^2)^0)$ depends on the total amplitude in SM.

In conclusion, the Higgs boson acts as "moderator" to unitarize high-energy longitudinal vector boson scattering by restoring unitarity of total amplitude in high energy region.

Chapter 3 The Large Hadron Collider and the ATLAS Detector

3.1 The Large Hadron Collider

Located near the French-Swiss border at the European Organization for Nuclear Research (CERN), the Large Hadron Collider (LHC) is the world's largest and most powerful particle collider. It's the proton-proton collider with center-of-mass energy up to 14 TeV. The beams inside the LHC are made to collide at four locations around its 27-kilometer accelerator ring, corresponding to the positions of four particle detectors - ATLAS, CMS, ALICE and LHCb. With its unprecedented energy, the LHC is designed to observe physics that involve highly massive particles which have never been observable in earlier lower energy accelerators.

3.1.1 Operation history and machine layout

Operation history

The LHC^[12-15] is a two-ring-superconducting-hadron accelerator and collider lies in a tunnel 27 kilometres in circumference and as deep as 175 metres. It's designed to provide proton-proton (pp) collisions at the center-of-mass energy (\sqrt{s}) up to 14 TeV with a unprecedented luminosity of $10^{34} \text{ cm}^{-2} \text{ s}^{-1}$. In the meantime, it can also collide heavy (Pb) ions with an energy of 2.8 TeV per nucleon and a peak luminosity of $10^{27} \text{ cm}^{-2} \text{ s}^{-1}$. Table 3.1 shows the main design parameters of the LHC for proton-proton collisions.

The LHC was built from 1998 to 2008. It started its first beam in September 2008, but then was interrupted by a quench incident only after a few days running. Then it resumed the operation in November 2009 with a low energy beams. From March 2010, physics runs took place at the energy of 7 TeV, Later on, this energy was increased in 2012 to $\sqrt{s} = 8 \text{ TeV}$, with an integrated luminosity of 20.3 fb^{-1} , and this period is called "Run-1". After run-1, the LHC was shut down for two years for hardware maintenance and upgrade, starting from February 2013.

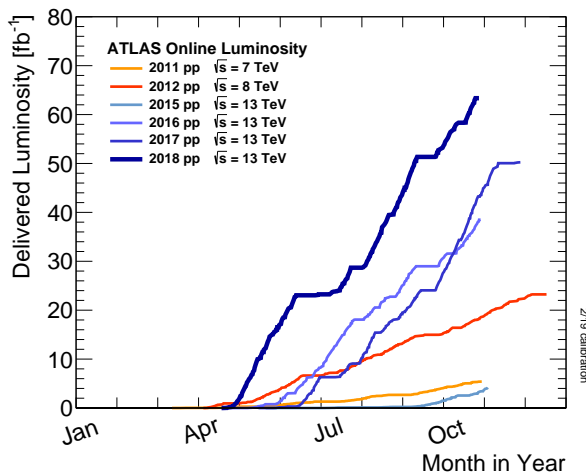
The second operation period with higher center-of-mass energy at 13 TeV started from 2015 called "run-2". And it continued to the end of 2018 with total integrated luminosity reaching about 147 fb^{-1} for ATLAS. Figure 3.1 shows the cumulative luminosity versus month delivered to ATLAS during stable beams at each years from 2011 to 2018.

Machine layout

The layout of CERN accelerator complex is shown in figure 3.2. The protons are

Table 3.1 Summary of design parameters of the LHC for pp collisions.

Circumference	26.7 km
Beam energy at collision	7 TeV
Beam energy at injection	0.45 TeV
Dipole field at 7 TeV	8.33 T
Luminosity	$10^{34} \text{ cm}^{-2} \text{s}^{-1}$
Beam current	0.56 A
Protons per bunch	1.1×10^{11}
Number of bunches	2808
Nominal bunch spacing	24.95 ns
Normalized emittance	$3.75 \mu\text{m}$
Total crossing angle	$300 \mu\text{rad}$
Energy loss per turn	6.7 keV
Critical synchrotron energy	44.1 eV
Radiated power per beam	3.8 kW
Stored energy per beam	350 MJ
Stored energy in magnets	11 GJ
Operating temperature	1.9 K

**Fig. 3.1 Cumulative luminosity versus time in ATLAS.**

accelerated by a series of machines before being injected into the main cavity. At beginning, the 50 MeV protons are produced in the linear particle accelerator LINAC2, and then further accelerated to 1.4 GeV in Proton Synchrotron Booster (PSB). The protons are then injected into the Proton Synchrotron (PS) to gain the energy of 26 GeV and further accelerated to 450 GeV in Super Proton Synchrotron (SPS). At the end, they are injected

into the main ring, and can reach a maximum energy of 7 TeV.

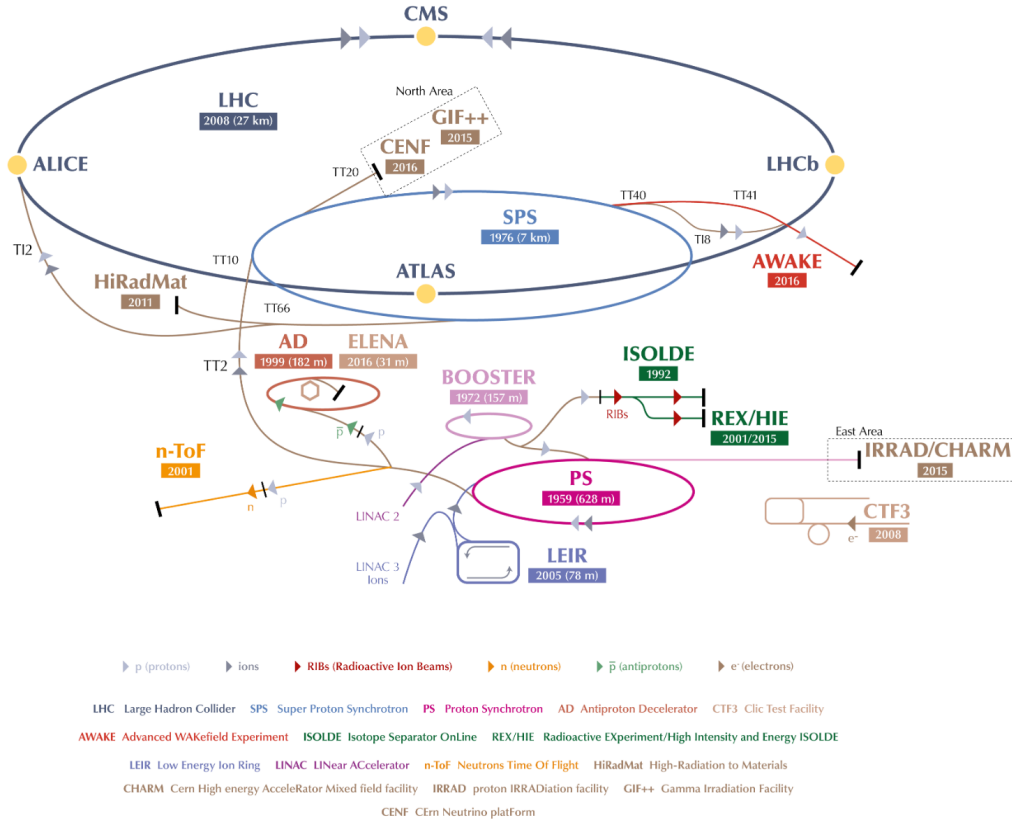


Fig. 3.2 CERN accelerator complex^[16].

The collisions can occur in 4 points, with corresponding 4 major detector experiments that are briefly described as follows:

- **ATLAS:** A Toroidal LHC ApparatuS, one of the two general-purpose particle detector experiments and detector with largest volume at the LHC. It is designed to search for the Higgs boson, test the stardand model of particle physics and search for possible beyond SM physics.
- **CMS:** Compact Muon Solenoid, another large general-purpose particle physics detector, with the same physics goal (also cross check) as ATLAS.
- **ALICE:** A Large Ion Collider Experiment, it is optimized to study heavy-ion (Pb-Pb nuclei) collisions at a centre of mass energy of 2.76 TeV per nucleon pair.
- **LHCb:** Large Hadron Collider beauty, it is a specialized b-physics experiment, designed primarily to measure the parameters of CP violation in the interactions of b-hadrons.

3.1.2 Luminosity and pile-up

Luminosity

In beam-beam collisions, the event rate for a given process is given by^[15]:

$$N = L\sigma \quad (3.1)$$

where σ is the cross section of the process, and L is the luminosity. For the studies of rare events, L must be as high as possible. The luminosity only depends on the beam parameters, and can be written as:

$$L = \frac{N_b^2 n f_r \gamma}{4\pi \epsilon_n \beta^*} \quad (3.2)$$

where N_b denotes the number of particles per bunch, n is the number of bunches per beam, f_r is the revolution frequency, γ represents relativistic γ factor, ϵ_n is the normalized transverse emittance and β^* denotes the β function at the collision point. To reduce the beam-beam interaction effects, the bunches must have a crossing angle, which produces a geometrical luminosity reduction factor F :

$$F = 1/\sqrt{1 + \left(\frac{\theta_c \sigma_Z}{2\sigma^*}\right)} \quad (3.3)$$

where θ_c denotes the crossing angle at the interaction point, σ_Z is the root mean square (RMS) bunch length and σ^* is the transverse RMS beam size at crossing point.

The luminosity expressed in Eq. 3.2 is normally the instantaneous luminosity. In fact the running conditions usually vary with time, so the luminosity can change as well. To take into account the time dependence, integrated luminosity is imported, which is the integral over time:

$$L = \int \mathcal{L}(t) dt \quad (3.4)$$

The unit of integrated luminosity we commonly use is b^{-1} ($1b^{-1} = 10^{24} cm^{-2}$). Figure 3.3 shows integrated luminosity versus time delivered to ATLAS (green), recorded by ATLAS (yellow), and certified to be good quality data (blue) during run-2 pp collisions.

Pile-up

In collisions, multiple interactions can happen in one single bunch crossing, which is called "pile-up". The variable μ , which represents the average number of interactions per bunch crossing, is defined to describe pile-up effect:

$$\langle \mu \rangle = \frac{L_{bunch} \sigma}{f_r n_{bunch}} \quad (3.5)$$

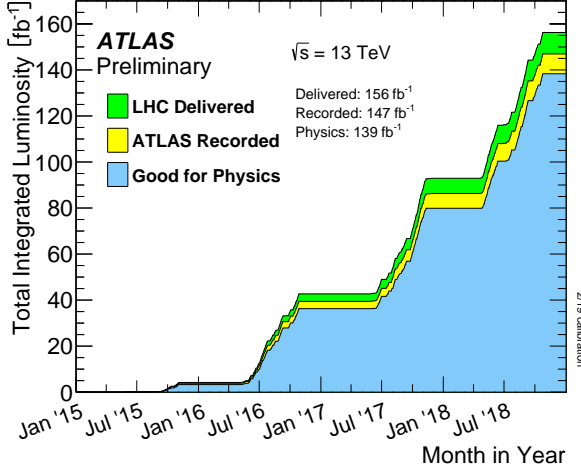


Fig. 3.3 Integrated luminosity in ATLAS.

where L_{bunch} is the instantaneous luminosity for each bunch, σ the inelastic cross section, f_r the LHC revolution frequency and n_{bunch} the number of colliding bunches. Normally, with increasing luminosity, the pile-up becomes more significant. Figure 3.4 shows the luminosity-weighted distribution of the mean number of interactions per crossing for pp collision data from 2015 to 2018 (full run-2), the challenge of pile-up increased in each year.

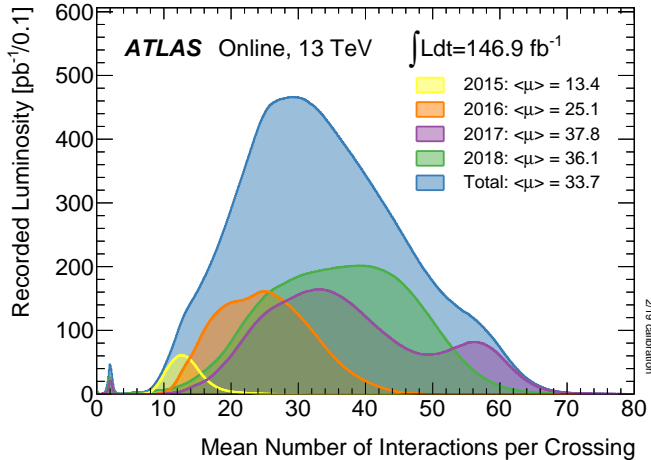


Fig. 3.4 Number of Interactions per Crossing from 2015-2018 in ATLAS.

3.2 ATLAS detector

3.2.1 Detector overview

ATLAS (A Toroidal LHC ApparatuS) is the largest volume detector ever constructed for a particle collider. It has the dimensions of a cylinder with 46 meters long, 25 meters in diameter, and sits in a cavern 100 meters below ground. The detector contains about

3000km of cables and it weights 7000 tonnes.

This paragraph briefly summarizes the coordinate system and nomenclature used to describe the ATLAS detector^[17]. As shown in figure 3.5, we define the nominal interaction point as the origin of the coordinate system, the beam direction as the z -axis and the x - y plane is transverse to the beam direction. The positive x -axis is defined to be the direction pointing to the center of the LHC ring, while the positive y -axis is pointing upwards. There are two sides of detector A and C, in which A(C)-side is defined as with

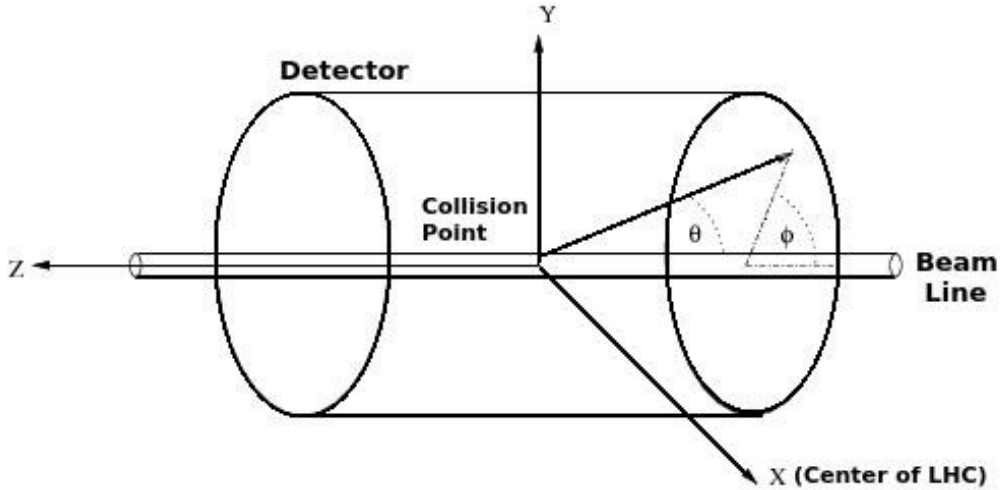


Fig. 3.5 Coordinate system used by the ATLAS experiment at the LHC^[18].

positive (negative) z . The azimuthal angle ϕ is measured as usual around the beam axis, while the polar angle θ is the angle from the beam axis. In physics analysis, we usually use the pseudorapidity instead of θ angle, which is designed as $\eta = -\ln[\tan(\frac{\theta}{2})]$. For massive objects (eg. jets), the rapidity $y = \frac{1}{2}\ln[\frac{E+p_z}{E-p_z}]$ is used. In addition, the *transverse* momentum p_T , *transverse* energy E_T and the missing *transverse* energy E_T^{miss} are defined in x - y plane. The commonly used distance measurement ΔR , is defined in the pseudorapidity-azimuthal angle space as $\Delta R = \sqrt{\Delta\eta^2 + \Delta\phi^2}$.

The overall ATLAS layout is shown in figure 3.6, which is forward-backward symmetric with respect to the interaction point. The magnet configuration comprises a thin superconducting solenoid surrounding the inner-detector cavity, and three large superconducting toroids (one barrel and two end-caps) arranged with an eight-fold azimuthal symmetry around the calorimeters.

The inner detector, which is the innermost part of ATLAS, is immersed in a 2 T solenoidal magnetic field. It's used for pattern recognition, momentum and vertex measurements and electron identification, with the combination of tracking system.

The calorimeter is outside the inner detector, for electromagnetic and hadronic energy measurements. High granularity liquid-argon (LAr) electromagnetic sampling

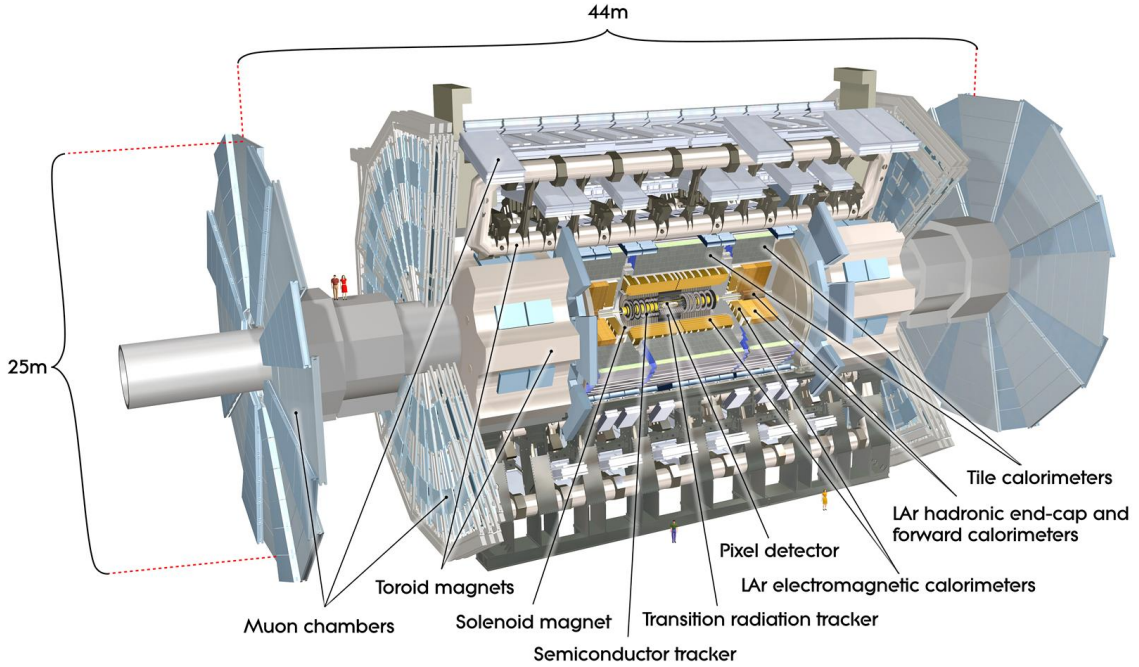


Fig. 3.6 Cut-away view of the ATLAS detector^[19].

calorimeters is used to measure energy and position resolution with range up to $|\eta| < 3.2$ for electrons and photons. For hadronic calorimetry, a scintillator-tile calorimeter is used in the range of $|\eta| < 1.7$. The LAr forward calorimeters provide both electromagnetic and hadronic energy measurements with the coverage up to $|\eta| = 4.9$.

The muon spectrometer is in the outermost side. The air-core toroid system, with a long barrel and two inserted end-cap magnets, provides strong bending power in a large volume within a light and open structure. Multiple-scattering effects are minor, and excellent muon momentum resolution can be achieved.

3.2.2 Physics requirement

As mentioned previously, ATLAS is one of two general-purpose particle detector experiment at the LHC. It's designed to take advantage of the unprecedented energy at the LHC. The Higgs boson was discovered as one of its benchmark, and lots of precise tests and measurements of SM is on going. In the meantime, ATLAS is also designed to observe the phenomena that involve highly massive particles, such as heavy beyond standard model (BSM) gauge bosons Z' and W' . It can also explore the possibility of extra dimensions proposed by several models in TeV region. To fulfil many diverse physics goals, a set of general requirements are needed:

- The speed-fast and radiation-hard electronics are required due to the experimental

conditions at the LHC.

- High detector granularity is needed to reduce the overlapping events and handle the particle fluxes.
- Large acceptance in pseudorapidity and azimuthal angle coverage is needed.
- For inner detector, good charged-particle momentum resolution and reconstruction efficiency are crucial. And the vertex detectors close to the interaction region are required to be able to observe secondary vertices for offline tagging of τ -lepton and b -jets.
- Good electromagnetic (EM) calorimetry for electron and photon, as well as full-coverage hadronic calorimetry for accurate jet and missing transverse energy measurements, are importantly required, since these measurements form the basis of many studies.
- Good muon spectrometer is also required for muon identification and momentum resolution measurement over a wide range of momenta.
- Highly efficient but with sufficient background rejection triggers are also needed and extremely important for objects with low transverse-momentum.

More detailed descriptions of each sub-system will be given in the following subsections.

3.2.3 Magnet system

A strong magnetic field is required for precise measurement of charged particle momenta. The ATLAS detector uses two large superconducting magnet systems, a hybrid system of a central superconducting solenoid and three outer superconducting toroids, to bend charged particles^[20]. The total magnet system is 22m in diameter and 26m in length as shown in figure 3.7.

The central solenoid produces two tesla magnetic field surrounding the inner Detector. When obtaining such high field strength, at the same time, the solenoid needs to be thin in order to reduce the material in front of the calorimeter.

The outer toroid system comprises one barrel superconducting toroid and two end-caps. The barrel one is composed of eight coils encased in individual racetrack-shaped, stainless-steel vacuum vessels and produces the magnetic field in the cylindrical volume surrounding the calorimeters. Each end-cap toroid consists of a single cold mass built up from eight flat, square coil units and eight keystone wedges and provides a magnetic field of approximately 1 T for the muon detectors in the end-cap regions.

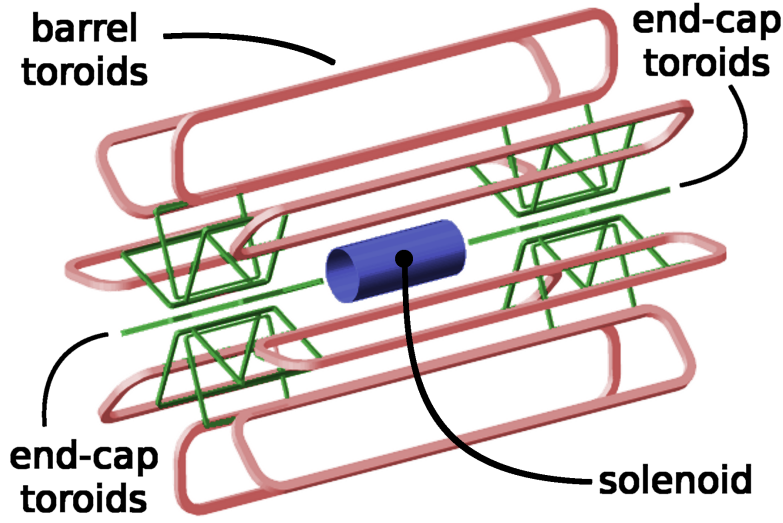


Fig. 3.7 Schematic diagram of the ATLAS magnet system.

3.2.4 Inner detector

The inner detector, as shown in figure 3.8, is the detector closest to beam pipe. It's used to measure the position of charged particle tracks in high precision together with good momentum resolution, in which the measurement of primary and secondary vertices and electron identification are especially important. Due to the extremely high luminosity produced by the LHC, the precise measurements of vertex and momentum becomes tough and fine-granularity detectors are crucial. The inner detector consists of three subdetectors that will be described as below.

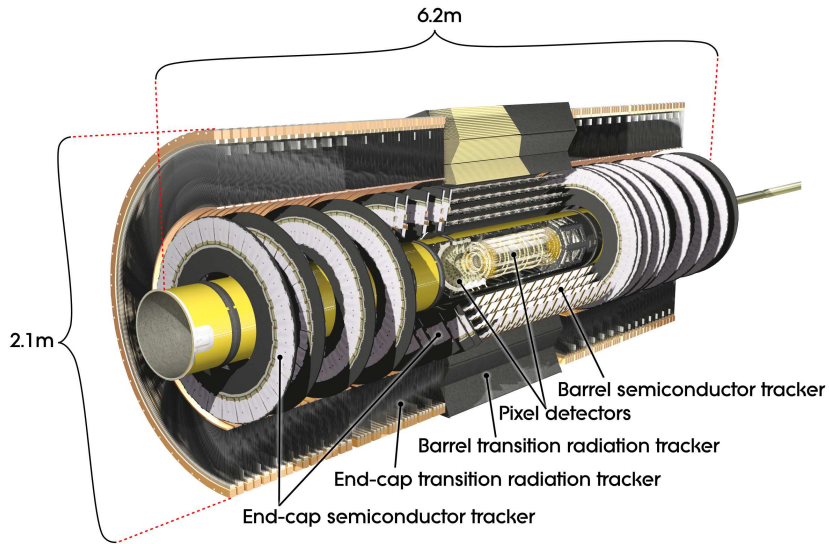


Fig. 3.8 Schematic diagram of the ATLAS inner detector^[21].

Pixel detector

The pixel detector is the innermost part of ATLAS tracking system. With finest gran-

ularity of materials, it has the best spatial resolution and 3-dimensional space-point measurement in inner detector. ATLAS Pixel Detector for the LHC run-2 is composed of 4 layers of barrel pixel detector and two end-caps with three pixel disks each, as shown in figure 3.9. There are three outer layers that originally installed for run-1 and one additional layer called Insertable B-Layer (IBL) that newly constructed in run-2^[22]. Now the 4-layer pixel detector has very good reconstruction of primary and secondary vertices, which is even crucial for long-lived particles like τ -lepton and b-quark.

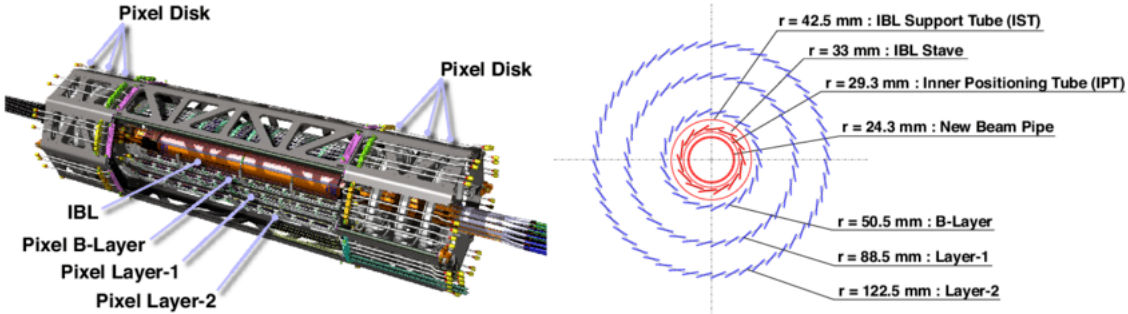


Fig. 3.9 Schematic diagram of the ATLAS 4-Layer Pixel Detector.

Semiconductor Tracker

The Semiconductor Tracker (SCT) is the middle component of the inner detector that outside the pixel detector. It has similar function as pixel detector but with long and narrow strips instead of small pixels, which makes a much larger coverage than pixel detector. The SCT consists of 4088 modules, it contains four concentric layers in barrel (2112 modules) and nine disks in each of the two end-caps (1976 modules) as shown in figure 3.10. And it measures particles over a large area with 6.3 million readout channels and a total area of 61 square meters. The SCT is the most critical part of the inner detector for 2D track hit reconstruction. In barrel, the hit precision is $17 \mu\text{m}$ in the $r\text{-}\phi$ coordinate and $580 \mu\text{m}$ in z coordinate. In end-caps, it have accuracies of $17 \mu\text{m}$ in the $z\text{-}\phi$ coordinate and $580 \mu\text{m}$ in r coordinate.

Transition radiation tracker

The transition radiation tracker (TRT)^[24] is the outermost part of inner detector. It has a very different design with the two previously sub-detectors. It's composed of thin-walled drift tubes called straw, also in three parts: a barrel and two end-cap regions. There are 73 barrel layers and 224 end-cap layers (112 in each) with 372000 straws in total, and about 351000 readout channels for TRT. The TRT provides better z resolution but much worse $r\text{-}\phi$ resolution (about $130 \mu\text{m}$) compared to the pixel detector and SCT per straw. But the straw hits still make significant contributions to momentum measurement, since its lower precision per point (compared to silicon) can be compensated by the large number

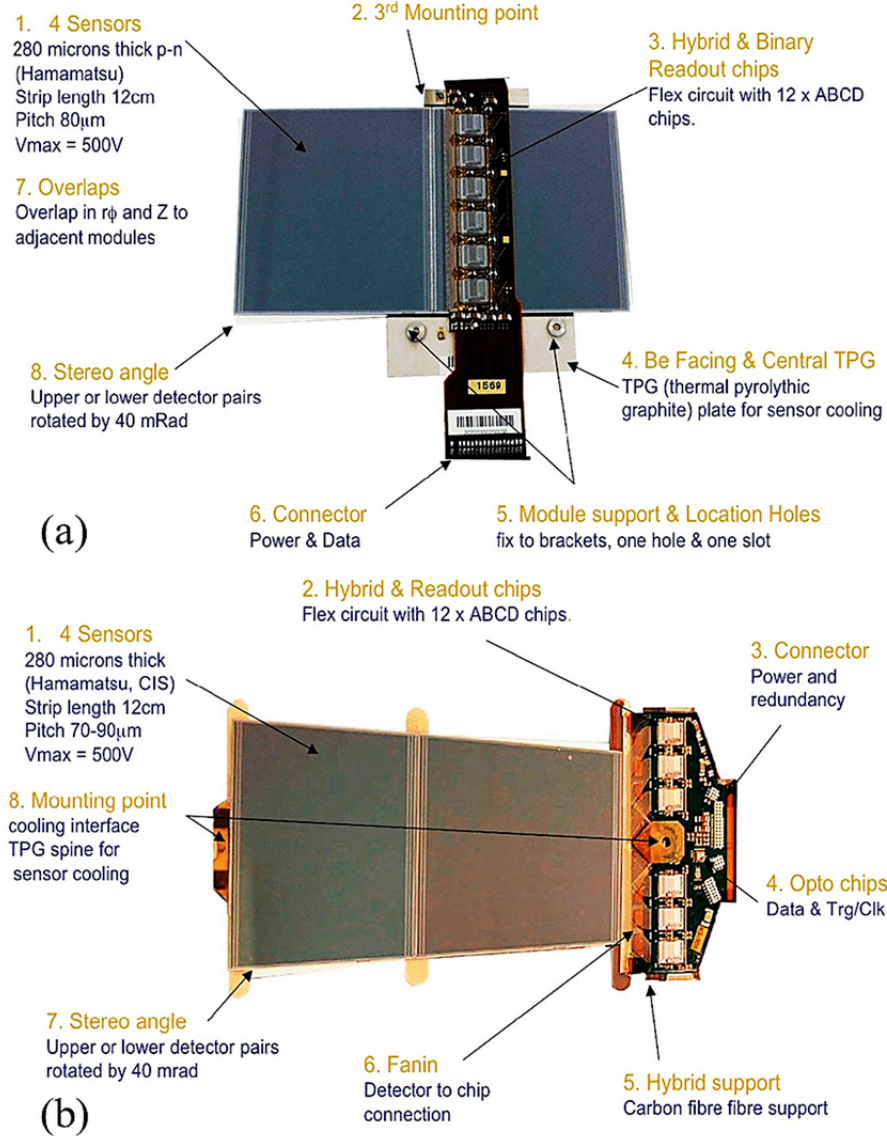


Fig. 3.10 SCT (a) barrel module and (b) end-cap^[23].

of measurements and long track length.

3.2.5 Calorimeters

The calorimeters are designed to measure the energy from particles by absorbing them. They are located outside the solenoidal magnet that surrounds the inner detector. The ATLAS calorimeters are comprised of a number of sampling calorimeters with full ϕ -symmetry and the pseudorapidity range of $|\eta| < 4.9$. Figure 3.11 shows the layout of the ATLAS calorimeter system. As mentioned in overview section, there are two basic calorimeter systems: an inner electromagnetic (EM) calorimeter and an outer hadronic calorimeter. The EM calorimeter is designed for precise measurements for electrons and photons, so that with fine granularity; while the hadronic one with relative coarser gran-

ularity but satisfied the physics requirements for jets reconstructions and E_T^{miss} measurements. Two different sampling techniques are used, the EM calorimeter is purely based on liquid-argon (LAr) technology, hadronic calorimeter use both LAr and scintillating tiles calorimeters. More details are described as below.

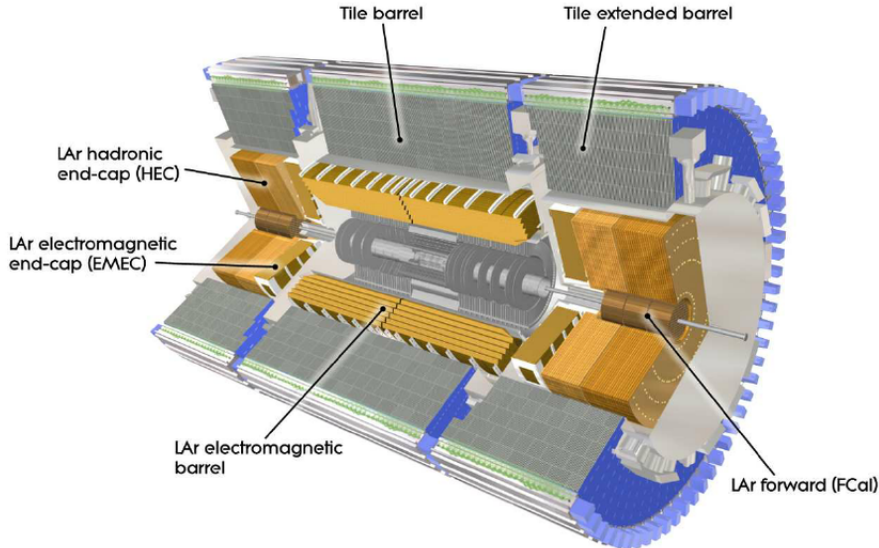


Fig. 3.11 Cut-away view of the ATLAS calorimeters. The LAr calorimeters are seen inside the scintillator- based Tile hadronic calorimeters^[25].

Liquid Argon calorimeter

The LAr calorimeter is the one uses liquid-argon as active medium. The Liquid Argon sampling calorimeter technique with "accordion-shaped" electrodes is used for all electromagnetic calorimetry covering the pseudorapidity range of $|\eta| < 3.2$; and for hadronic calorimetry from $|\eta| = 1.4$ up to the acceptance limit $|\eta| = 4.9$ ^[26]. Figure 3.12 shows the shape of a barrel module as accordion geometry. For barrel EM calorimeter, the absorbing material is lead-liquid argon, while the hadronic end-cap calorimeter use copper plates as the absorbing material. In addition, the forward calorimeter is split into three parts, an EM sector in which copper is used as absorbing material and two hadronic sectors using tungsten outside the EM sector.

Tile calorimeter

Tile calorimeter is a sampling calorimeter that use scintillating plates as active medium and steel as absorber. It consists of three sections: the central barrel with the pseudorapidity range of $|\eta| < 1.0$ and two extended barrels with $0.8 < |\eta| < 1.7$. Figure 3.13 shows the design of one tile calorimeter module. It's used for energy reconstruction of jets and E_T^{miss} measurement by combining with the forward and end-cap hadronic calorimeter.

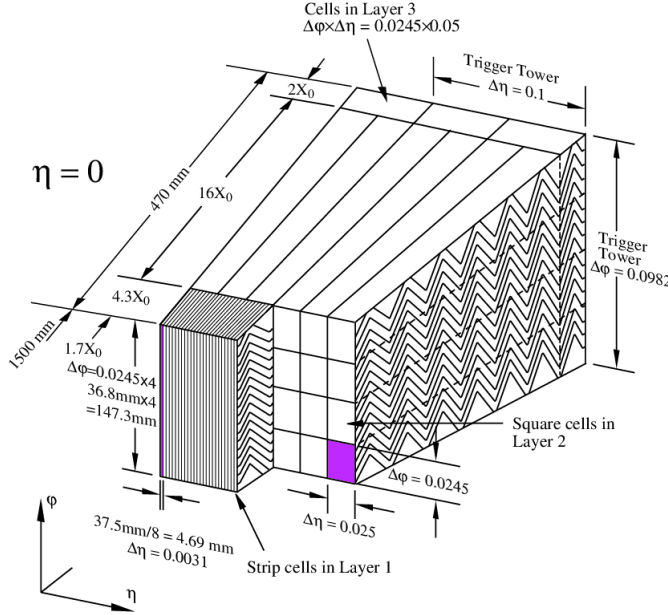


Fig. 3.12 Schematic diagram of a LAr EM calorimeter barrel module.

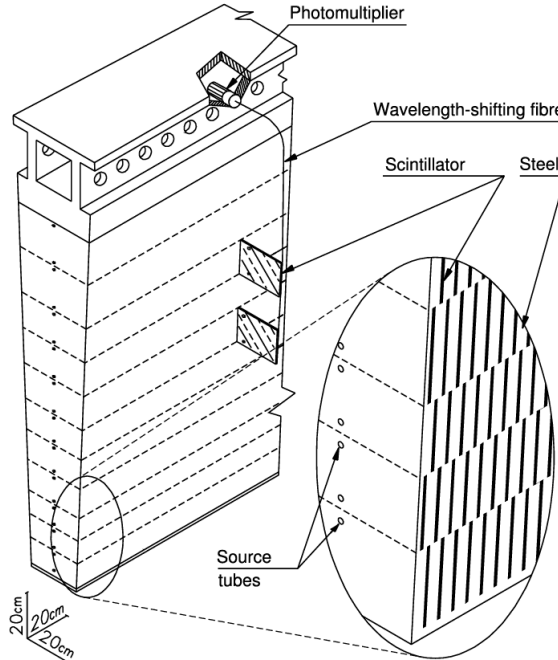


Fig. 3.13 Schematic diagram of tile calorimeter module [27].

3.2.6 Muon spectrometer

Muon spectrometer is the outermost part of the ATLAS detector with an extremely large tracking system. It measures a large range of muon momentum, and the accuracy can be about 3% at 100 GeV and 10% at 1 TeV. The muon spectrometer is comprised of three main parts: a magnetic field produced by three toroidal magnets; a set of chambers measuring the tracks of muons with high spatial precision; and triggering chambers with accurate time-resolution. Figure 3.14 shows the schematic of ATLAS muon spectrometer,

from which you can see four types of muon chambers (*MDT, CSC, RPC, TGC*) as well as the magnet systems (barrel and end-cap toroid).

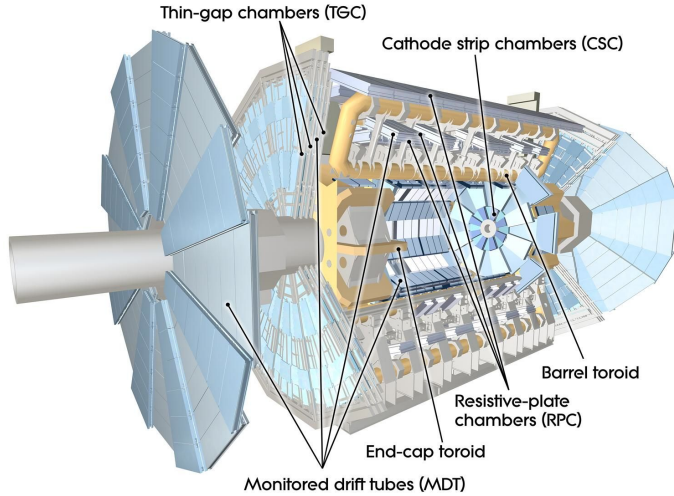


Fig. 3.14 Cut-away view of the ATLAS muon spectrometer^[28].

The details of four-type chambers are given as below:

- **Monitored Drift Tubes (MDT).** MDTs provide the precise momentum measurement with the $|\eta|$ range up to 2.7, except in the innermost end-cap layer where the coverage is limited to $|\eta| < 2.0$. The chambers are comprised of three or eight layers of drift tubes, with a diameter of 29.970 mm, operated with Ar/CO₂ gas (93/7) at 3 bar. The average resolution can reach 80 μm per tube and 30 μm per chamber.
- **Cathode strip chambers (CSC).** CSCs are used in the forward region of $2 < |\eta| < 2.7$ in the innermost tracking layers, due to their good time resolution and high rate capability. The CSCs are multi-wire proportional chambers (MWPC) with the cathode planes segmented into strips in orthogonal directions, which allows both coordinates to be measured from the induced-charge distribution. The resolution of a chamber is about 40 μm for bending plane and 5 mm for the transverse plane.
- **Resistive plate chambers (RPC).** The RPCs serve as fast triggers in the barrel region of $|\eta| < 1.05$ due to the high rate capability and good spatial and time resolution. It is a gaseous parallel electrode-plate detector without any wires. There are three concentric cylindrical layers around the beam axis, referred to as the three trigger stations. Each station consists of two independent layers to measure the transverse coordinates of η and ϕ .
- **Thin gap chambers (TGC).** TGCs are used as trigger system for the end-cap region of $1.5 < |\eta| < 2.4$, and operated based on the same principle as multi-wire proportional chambers. In addition, they can also provide the second azimuthal

coordinate to complement the measurement of MDT in bending direction.

3.2.7 Trigger system

Trigger system in ATLAS is a very essential component, which is responsible for deciding whether to keep a given collision event for later study or not. In the LHC run-2, higher energy, luminosity and pile-up lead to an large increase of event rate by up to a factor of five, which cause to a even larger challenge and more strict requirement of trigger system.

The trigger system in run-2 is comprised of a hardware-based first level trigger (Level-1) and a software-based high level trigger (HLT)^[29]. As depicted in figure 3.15, in Level-1, the inputs from coarse granularity calorimeter and muon detector information together with some other subsystems are sent to the Central Trigger Processor to determine Regions-of-Interest (RoIs) in the detector. The events rate can be reduced by Level-1

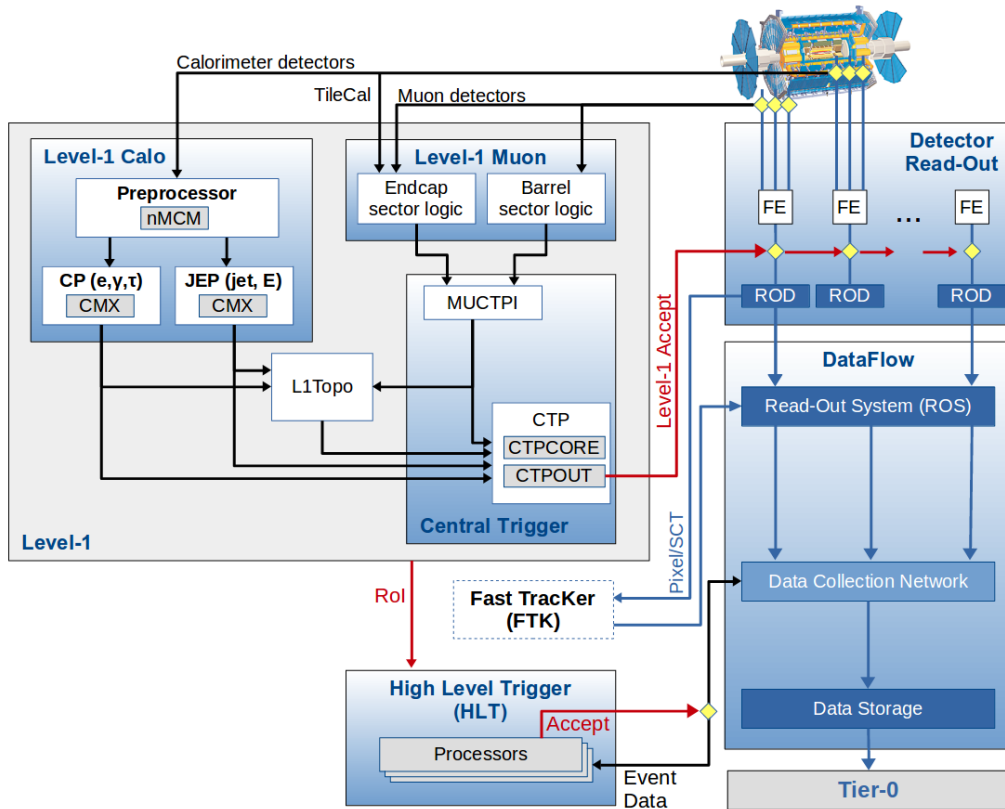


Fig. 3.15 Schematic diagram of the ATLAS trigger and data acquisition system in Run-2.

triggers from 30 MHz to 100 kHz. After that, the ROI information from Level-1 is sent to HLT, in which more sophisticated selection algorithms are run for regional reconstruction. The HLT reduces the rate from Level-1 of 100 kHz to about 1 kHz on average. At the end, the events that accepted by HLT are transferred to local storage at experimental site for offline reconstruction. Details about Level-1 and HLT trigger systems will be described

as below.

Level-1 trigger

Substantial upgrades have been delivered in ATLAS Level-1 trigger system for Run-2 data taking. The upgrades took place in both hardware and detector readout, allows the trigger rate increasing from 70 kHz (run-1) to 100 kHz (run-2). As mentioned above, there are two major parts of Level-1 triggers, which include Level-1 calorimeter (L1calo) trigger and Level-1 muon (L1mu) trigger.

Level-1 Calorimeter trigger uses the reduced granularity information from the electromagnetic and hadronic calorimeters to search for electrons, photons, taus and jets and missing transverse energy (E_T^{miss}). It can identify an Region-of-Interest (RoI) as a 2×2 trigger tower cluster in the EM calorimeter as shown in figure 3.16, and 4×4 or 8×8 trigger tower for Jet RoIs. One important upgrade is that, the new FPGA-based (field-

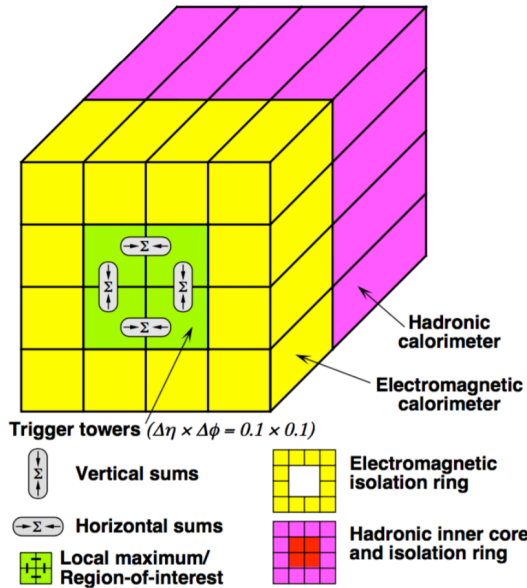


Fig. 3.16 An examples of L1 calorimeter trigger tower for electron and photon triggers^[30].

programmable gate array) Multi-Chip Modules are used to replace the ASICs (application-specific integrated circuits) included in the modules used in run-1, which allows the use of auto-correlation filters to suppress pile-up.

The Level-1 Muon trigger system includes one barrel section (RPC) and two end-cap section (TGC), which provides fast trigger signals from the muon detectors for the Level-1 trigger decision. By requiring a coincidence with hits from the innermost muon chambers, it can reduce the $L1_MU15$ rate by about 50% in the region of $1.3 < |\eta| < 1.9$ while only loss around 2% signal efficiency. In addition, the coverage is extended by around 4% due to installing new chambers in the feet region of the muon detector.

High Level Trigger

The ATLAS trigger system separated the Level-2 and Event Filter computer clusters in run-1, but for run-2, they have been merged into a single HLT event processing. The new arrangement helps to reduce the complexity and duplication of algorithm, which leads to a more flexible high level trigger system. During the long-shutdown between LHC run-1 and run-2, lots of re-optimizations have been done for trigger reconstruction algorithms as well as the offline analysis selections, which can improve the efficiency by more than a factor of two in some cases like in hadronic tau triggers. For some triggers, the HLT processing performed within RoIs can also allows to aggregate from RoIs to single objects. This improvement reduces the CPU processing for events with overlapping RoIs, and the average output rate has been increased from 400 Hz to 1 kHz. The HLT reconstruction algorithm can be divided into fast and precision online reconstruction steps. As depicted by figure 3.17, the initial fast reconstruction helps to reduce the event rate early, and be seeded into precision reconstruction. Then the final online precision reconstruction is improved and uses offline-like algorithms as much as possible. In particular, multivariate analysis techniques (based on machine learning) have been introduced online in many aspects.

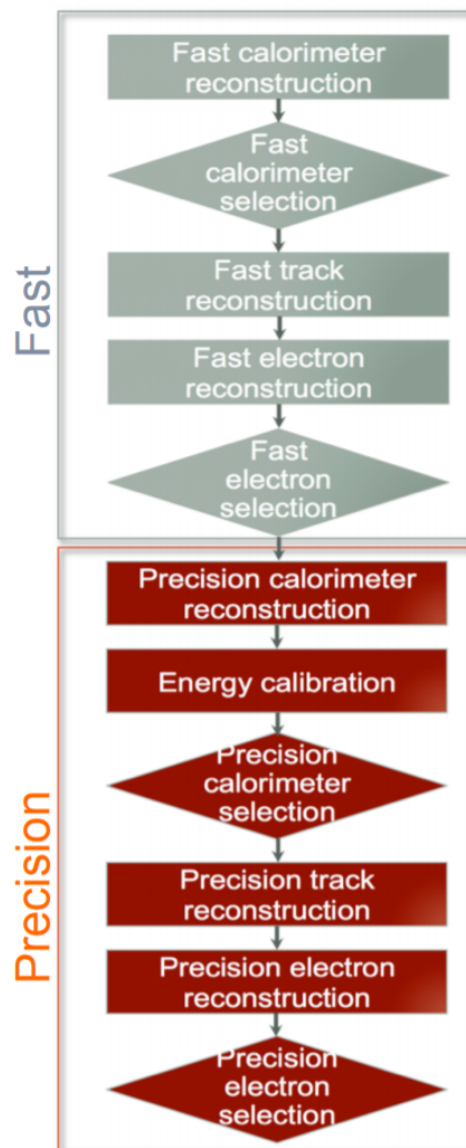


Fig. 3.17 The HLT trigger algorithm sequence^[30].

Chapter 4 Simulation and Event Reconstruction for the ATLAS Experiment

In current LHC pp collision, bunches of protons collide every 25 nanoseconds (ns), which gives a large challenge to event reconstruction and selections. To predict and model each process, the Monte Carlo simulations of physics events are essential for high-energy physics experiments. This section will briefly discuss the event simulation and reconstruction programs based on the ATLAS software framework.

4.1 Event simulation

The ATLAS simulation program is integrated into the ATLAS software framework called *Athena*^[31], which uses Python as an object-oriented scripting and interpreter language to configure and load C++ algorithms and objects. Figure 4.1 shows the overview of ATLAS simulation data flow^[32]. In the diagrams, the square-cornered boxes represents algorithms and applications to be run and round-cornered boxes denote data objects.

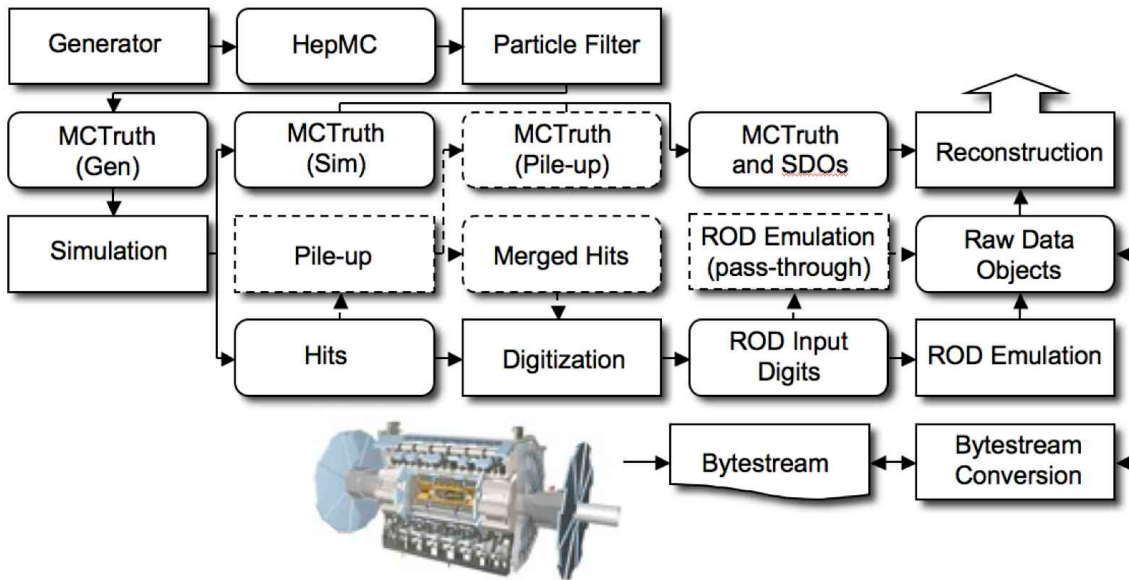


Fig. 4.1 The flow of the ATLAS simulation software.

First of all, events are produced by MC generators in standard HepMC format and then read into the simulation. During the simulation, particles are propagated through the full ATLAS detector whose configurations can be set by users via GEANT4 toolkit. The energies deposited in the sensitive regions of the detector are recorded as *hits*, which contains the total energy deposition, position, and time, and are written to a simulation

hit file. In the meantime, the events in "truth" format are also recorded to contain the history of the interactions from the generator, including incoming and outgoing particles. Simulated Data Objects (SDOs) are created from truth, which are maps between hits in sensitive portions of the detector and truth information of particles in simulation. The files are then sent to digitization, with constructs "digits" inputs and be written into Raw Data Object (RDO) file used for reconstruction.

In conclusion, there are three main parts of framework: *Generation*, *Simulation* and *Digitization*. More details are given below.

Event generation

As shown in figure 4.2^[33], at hardon colliders, multiple scattering and rescattering effects arise, which must be simulated by Monte Carlo (MC) event generators to reflect the full complexity of those event structures. Several MC event generators can be used to generate events originally in HepMC format. The events can be filtered at generation time with some certain requirements (eg. decay channel or missing energy above a certain threshold). The generator is responsible for any prompt decays (e.g. W or Z bosons) but stores any "stable" particle expected to propagate through a part of the detector. During the generation steps, any interactions with detector are ignored and only immediate decays are considered.

There are several MC generators that have been widely-used with general purpose, which include Sherpa^[34], Herwig++^[35], PowhegBox^[36], MC@NLO^[37] and Pythia8^[38].

Simulation

GEANT4 is used as standard simulation toolkit for the ATLAS experiment, which transports physics particles through the detector's geometry. During the generation level, the entire connected chain of the HepMC event is stored as the Monte Carlo truth. Only the stable particles are read into GEANT4 for further simulation and cuts and transformations can be applied to these events to select certain processes. During the simulation, many secondary tracks can be produced, therefore only information from the interactions of interest are stored, including the incoming particles, step sequence, vertex and also outgoing particles. The output of GEANT4 is called *hit file*, which contains metadata describing the configuration of the simulation during the run, all truth information requested and a collection of hits for each subdetector.

Since the standard ATLAS detector simulation cost very large computing resources to accurately model the complex detector geometry and physics descriptions, some fast simulation programss are developed according to different user purpose. Some widely-used fast-sim toolkits include *Fast G4 Simulation*^[39], *ATLFAST-I*^[40] and *ATLFAST-II*^[41].

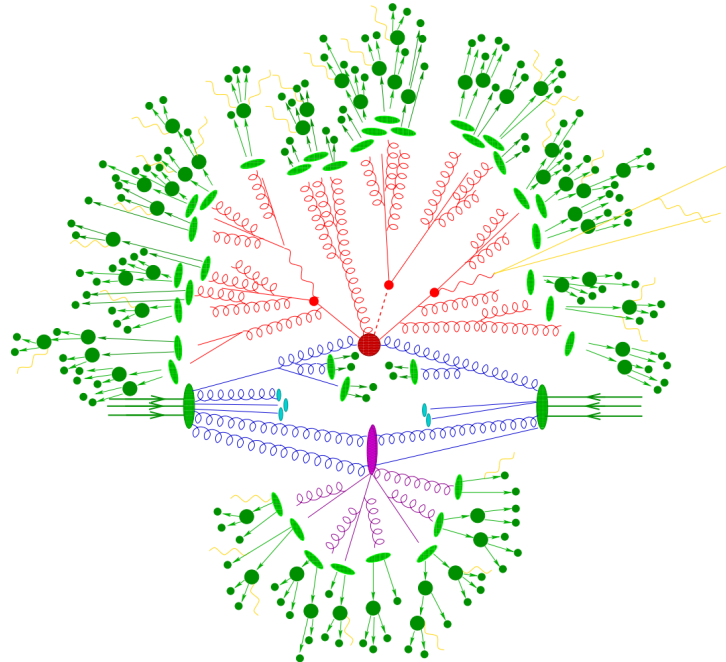


Fig. 4.2 Sketch of a hardon-hardon collision simulated by MC event generator. The red blob in center denotes the hard collision, surrounded by tree-like structures representing Bremsstrahlung which is simulated by Parton Showers. The purple blob stands for a secondary hard scattering event. The light green blobs indicate the parton-to-hardon transitions and the dark green blobs represents hadron decays. The yellow lines are soft photon radiations.

Digitization

The hit outputs from simulated events, including hard scattering signal, minimum bias, beam halo, beam gas and cavern background events, are then send into digitization to convert into detector response called "digits". Before converting into detector signal with 'digits' formart, each type of events can be overlaid at a user-specified rate. Those overlay, called "pile-up", can be done during digitization to save the CPU time in simulation level. At this stage, the detector noise and the first level trigger that implemented with hardware on the real detector are added into events. The digitization firstly constructs "digits" inputs to the read out drivers (RODs) in the detector electronics. The ROD functionality is then emulated, and the output digits are written out as Raw Data Object (RDO) file. In addition, the digitization algorithms can also produce Simulated Data Objects (SDOs), which contain information about all the particles, noise and the amount of energy that contributed to the signal. Then all information are sent into reconstruction that will be described in next subsection.

4.2 Event reconstruction

The data flow of ATLAS data processing is sketched in figure 4.3^[42]. Data from detector is firstly filtered by online trigger system and then sent to the *Tier-0* (*T0*) for initial processing by offline reconstruction software also based on Athena. A small amount of data named "express stream" is processed in almost real time in *T0* for online data quality monitoring. In addition, some other dedicated data streams are sent out at trigger level for detector alignment and calibration. These calibration and alignment information are then used for bulk reconstruction in *T0*. At the end of the reconstruction chain, the data are delivered into *Tier-1* (*T1*) and *Tier-2* (*T2*) centers for further analysis and production of simulated data. Besides, *T1* centers are also responsible for data reprocessing by re-running data reconstruction with improved calibration and alignment constants and with improved reconstruction algorithms. This section describes the reconstruction of some important physics objects in ATLAS experiment, i.e. tracks, vertices, electrons, muons, jets, and missing energies.

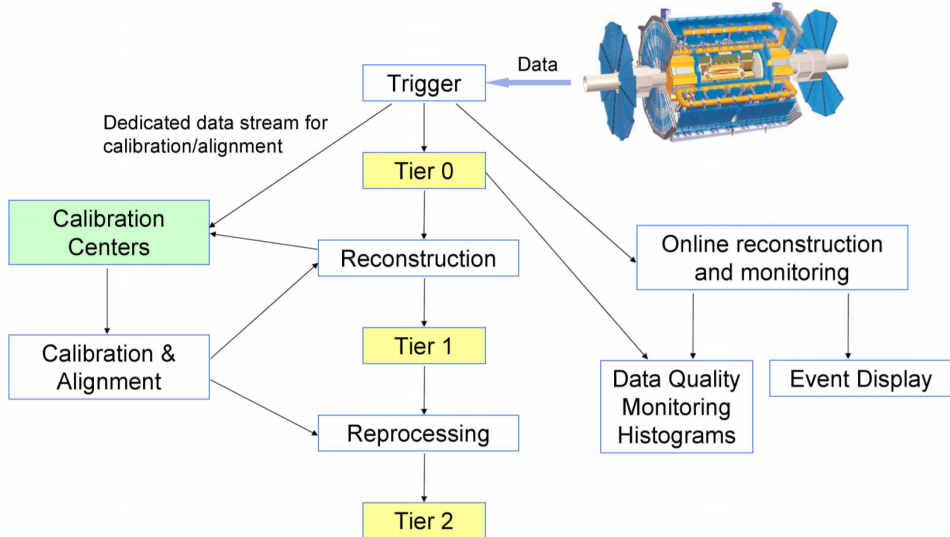


Fig. 4.3 The flowchart of the ATLAS data processing.

4.2.1 Track

The ATLAS detector is composed of two independent tracking systems: the Inner Detector (ID) close to the interaction point, and the Muon Spectrometer (MS). The reconstructed charged-particle trajectories in the ID and MS are referred to as ID tracks and MS tracks respectively. The ID reconstruction needs to handle high track density that imposes a large number of combinatorial track candidates, the MS reconstruction is however largely limited by the huge amount of inert material, the large background and the highly

inhomogeneous magnetic field^[43]. More details of two types of track reconstructions are given below.

Inner detector track

Figure 4.4 shows the ID system used for detect charge-particle tracks. The ID track reconstructions contains two sequences: *inside-out* track reconstruction and *outside-in* one.

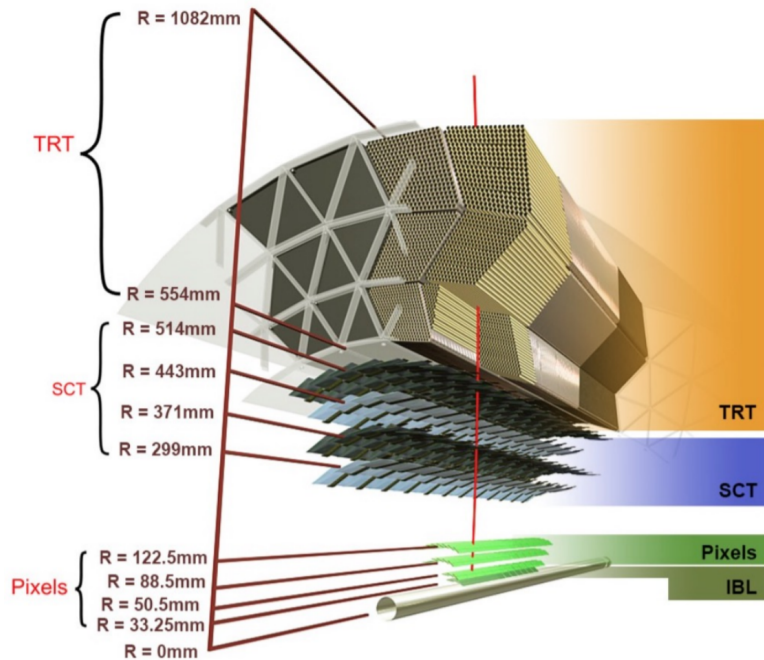


Fig. 4.4 Schematic view of the ATLAS inner detector showing all the corresponding components.

For inside-out tracking, it exploits the high granularity of the pixel and SCT detectors to discover prompt tracks originating from the interaction point. In first step, the track seeds are formed by combining the information of space-points in the three pixel layers and the first SCT layer. Then, these seeds are extended throughout the SCT to build track candidates. After that, these candidates are fitted, some quality cuts are applied to remove the outlier clusters, reject the fake tracks and resolve ambiguities in the cluster-to-track association. The selected tracks are then further extended to TRT, and refitted with the full information from pixel, SCT and TRT detectors.

Another complementary approach, outside-in, searches for unused track segments start from TRT instead. These segments are then extended into the SCT and pixel detectors to improve the tracking efficiency for secondary tracks from conversions or decays of long-lived particles.

Muon spectrometer track

The MS track reconstruction^[44] starts from searching hit patterns inside each muon chamber to form segments. In each MDT chamber and nearby trigger chamber, a Hough transform^[45] is used to search the hits lies on a certain trajectory in the bending plane of the detector. The MDT segments are reconstructed by performing a linear fit to the hits found in each layer. The RPC or TGC hits can be built by measuring the coordinate orthogonal to the bending plane. And the segments of CSC can be built using a separate combinatorial search in the η and ϕ detector planes.

Then muon track candidates are built by fitting together hits from segments in different layers. This task makes use of the algorithm by performing a segment-seeded combinatorial search, which starts by using the segments generated in the middle layers of the detector where more trigger hits are available as seeds. The search is then extended to use the segments as seeds from the inner and outer layers. The segments are selected based on criteria of hit multiplicity and fit quality, and are matched using their relative positions and angles. To build a track, at least two matching segments are required, except in the barrel-endcap transition region where a single high-quality segment with η and ϕ information can be used to build a track. At beginning, the same segment can be used to build more than one track candidates. Later on, an overlap removal algorithm is performed to select the best assignment to a single track, or decide whether allows the certain segment to be shared between two tracks.

The hits associated with each track candidate are then fitted using a global χ^2 fit. Then the algorithm accepts the track candidate if its fitting χ^2 passes the selection criteria. Hits contribute largely to χ^2 are removed and the track fit is repeated. In addition, the algorithm performs a hit recovery procedure that looks for additional hits consistent with the candidate trajectory, and the track candidate is refit if additional hits are found.

4.2.2 Primary vertex

The primary vertex (PV) is reconstructed by using the reconstructed tracks introduced in previous section as inputs. The tracks to be considered for vertex reconstruction must satisfy the following criteria^[46]:

- $p_T > 400 \text{ MeV}$
- $|\eta| < 2.5$
- Number of silicon hits $\geq \begin{cases} 9 & \text{if } |\eta| \leq 1.65 \\ 11 & \text{if } |\eta| > 1.65 \end{cases}$
- IBL hits + B-layer hits $\square 1$
- A maximum of 1 shared module (1 shared pixel hit or 2 shared SCT hits)

- Pixel holes = 0
- SCT holes \square 1

A candidate vertex is formed by requiring two tracks passing these selection criteria.

The reconstruction of PV can be divided into two steps^[47]: vertex finding and vertex fitting. The first step represents the pattern recognition process, namely the association of reconstructed tracks to vertex candidates. The latter one works on the reconstruction of the actual vertex position and its covariance matrix. More details are described as below:

First of all, a set of tracks passing the selection criteria mentioned above is selected. Then a seed position for the first vertex is chosen. This seed position is determined by beam spot in the transverse plane. The starting point for x- and y- coordinates are directly from the centre of the beam spot, while the one for z-coordinate is calculated as the mode of z-coordinates of tracks at their respective points with closest approach to the reconstructed centre of the beam spot.

After determining the seed position, the iterative primary vertex finding procedure starts. An vertex fitting algorithm is adopted to find the optimal vertex position by performing an iterative χ^2 minimization, in which the seed position is used as the start point and the reconstructed tracks are used as input measurements. For this fitting procedure, the input tracks are assigned weights to reflect their compatibility with the vertex estimation, and the vertex position is re-calculated based on these weighted tracks. Then the iterative procedure is repeated by re-calculating the track weight according to the new vertex position. After the last iteration, the final weight of each track used in vertex fit is estimated. And those incompatible tracks ($> 7\sigma$) are then rejected from this vertex candidate and moved back to the unused pool for next vertex finding. Then iteration procedure describes above are repeated again by using the remaining tracks, until no un-associated tracks are left or no additional vertex can be found in remaining tracks.

At the end, the vertices with at least two associated tracks passing through are treated as possible PV candidates. And the output of this vertex reconstruction algorithm is the information of three dimensional vertex positions and their covariance matrices. In physics analysis, it's most often to choose the one with highest sum of transverse momentum ($\sum p_T^2$) as PV.

4.2.3 Electron

Many of the interesting physical processes with the involvement of one or more electrons (or positrons) at the LHC. But these electrons can be subjected to large amount of backgrounds such as hadrons, non-prompt electrons from photon conversions and non-

isolated electrons from heavy flavor hadon decays. It is therefore essential to efficiently reconstruct and identify electrons and in the meantime to keep high background rejection.

In ATLAS, in central region, the electrons leave tracks in inner detector (ID) and the energy deposits in the electromagnetic (EM) calorimeter. Firstly the signals from calorimeter are used for L1 trigger system, and them combined with the information from ID tracks to reconstruct electron candidates that will be used for the high level trigger (HLT) decision algorithms^[48]. The backgrounds mentioned above can then be further suppressed by using several identification criteria. In addition, electrons are required to be isolated from other activities to be further distinguished from background.

More details of electron *reconstruction*, *identification* and *isolation* will be described as below.

Electron reconstruction

Several steps are proceeded for electron reconstruction in the central region of ATLAS detector ($|\eta| < 2.47$):

1. **Seed-cluster reconstruction:** A sliding window with size of 3×5 in unit of $\Delta\eta^{tower} \times \Delta\phi^{tower} = 0.025 \times 0.025$ in $\eta \times \phi$ space is utilized to search for electron cluster seeds with total cluster transverse energy greater than 2.5 GeV. Then a clustering algorithm^[49] is applied to form the clusters around the seeds, which can take advantage of removing the duplications. The kinematics of clusters are then reconstructed by using an extended window depending on the cluster position. The efficiency of cluster search is from about 95% at $E_T = 7GeV$ to 99% for $E_T \geq 15GeV$.
2. **Track reconstruction:** The track reconstruction can be divided into two steps: pattern recognition and track fit. The standard pattern recognition in ATLAS uses pion hypothesis for energy loss caused by interactions with detector material. If a track seed with $p_T > 1GeV$ cannot be successfully extended to a full track required at least seven hits using this pion hypothesis, but still falls inside one of the EM cluster region of interest, as a second attempt, the pattern recognition using electron hypothesis is then used to allow larger energy loss. Depending on the pattern that has been used in previous stage, the track candidates are then fitted with either the pion hypothesis or the electron hypothesis by using ATLAS Global χ^2 Track Fitter^[50]. If a track candidate fails the fit by using pion hypothesis, it can be refit with the electron hypothesis again. In this method, a specific electron-oriented algorithm is integrated into the ATLAS standard track reconstruction, which improves the performance for electron and as well as maintain minimal interference with the

main track reconstruction.

3. **Electron specific track fit:** Once the tracks are obtained, they are loosely matched to EM cluster using the distance in η and ϕ between the position of track (after extrapolation) in calorimeter's middle layer and the cluster barycentre. The matching conditions take into account the energy loss of bremsstrahlung and the number of precise hits in silicon detector.
4. **Electron candidate reconstruction:** The electron candidate is reconstructed by matching the track candidate to EM cluster seed to eventually completes the electron reconstruction procedure. If more than one track satisfy the matching condition, one track is chosen as primary track based on the information of the cluster-track distance R , the number of pixel hits and the presence of a hit in the first silicon layer^[51]. In addition, we remove the electron candidates mentioned above but without any associated precise hit tracks from electron pool and move them into photon candidates. Then we re-formed the electron clusters by using 3×7 (5×5) longitudinal towers of cells in barrel (endcaps) in EM calorimeter. The measured energy is calibrated to original electron energy based on MC simulated samples by using multivariate techniques (MVA).

In addition, in physics analysis, to reduce the background from photon conversions and secondary particles, the track associated with electron is required to be compatible with the primary vertex of the hard collision. Practically, the impact parameters cuts such as $d_0/\sigma_{d_0} < 5$ and $z_0 \sin\theta < 0.5\text{mm}$ are usually applied, where d_0 is the closest distance of the track to the measured beam-line, z_0 is the distance along the beam-line between the point where d_0 is measured and the beam-spot position, and the θ is polar angle of the track, σ_{d_0} denotes the estimated uncertainty of d_0 parameter. To be clearer, figure 4.5 depicts the definition of each track impact parameter.

Electron identification

The electron identifications (ID) are applied to determine the reconstructed electron candidates are more signal-like or background-like objects. The ID algorithms make use of quantities of related variables from electron cluster and track measurements including calorimeter shower shapes, track properties, as well as variables measuring bremsstrahlung effects for distinguishing signal from background. Taking the advantage of new IBL in run-2, the number of hits in this innermost pixel layer is utilized for discriminating between electrons and converted photons. In addition, a likelihood method based on the TRT high-threshold hits is adopted to compensate the lower transition radiation absorption probability of the argon.

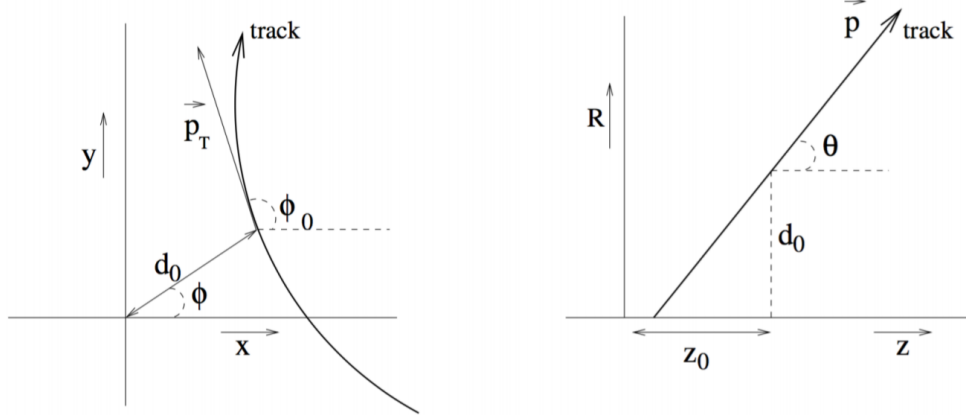


Fig. 4.5 Schematic of the impact parameters of a track in the transverse plane (left) and RZ-plane (right), as defined in the global ATLAS tracking frame^[52].

The baseline ID algorithm introduced for ATLAS run-2 data analysis is the likelihood-based (LH) method, which uses a MVA technique to simultaneously evaluate several properties of electron candidates when making a decision. The LH method utilizes the probability density functions (PDFs) of signal and background as the input discriminating variables. Based on these PDFs, it can calculate an overall probability for the object to be signal or background. Then the probabilities of signal and background are combined together into a discriminant $d_{\mathcal{L}}$:

$$d_{\mathcal{L}} = \frac{\mathcal{L}_S}{\mathcal{L}_S + \mathcal{L}_B}, \quad \mathcal{L}_{S(B)}(\mathbf{x}) = \prod_{i=1}^n P_{s(b),i}(x_i) \quad (4.1)$$

where \mathbf{x} denotes the vector of discriminating variables and $P_{s(b),i}(x_i)$ represents the value of signal (background) PDF of the i^{th} variable as x_i .

Three levels of working points (WPs) for electron ID are provided: *Loose*, *Medium* and *Tight*, in order of increasing background rejection. Samples selected by a looser WP are subsets of a tighter one, for example, the electrons passing Medium can all be selected by Loose. The ID efficiency varies as function of electron energy (E_T) as shown in figure 4.6. For evaluations, the electron candidates from MC simulation of $Z \rightarrow ee$ decays (di-jet) are used as signal (background). Depending on the working point, the signal (background) efficiencies for reconstructed electron candidates at $E_T = 25 GeV$ are in the range of 78 to 90% (0.3 to 0.8%), and increase (decrease) with E_T .

Electron isolation

In addition to the ID criteria, most analyses have electron isolation requirement to further distinguish signal from background. To quantify the energy of particles around the electron candidate, the isolation variables can help to separate the prompt electron

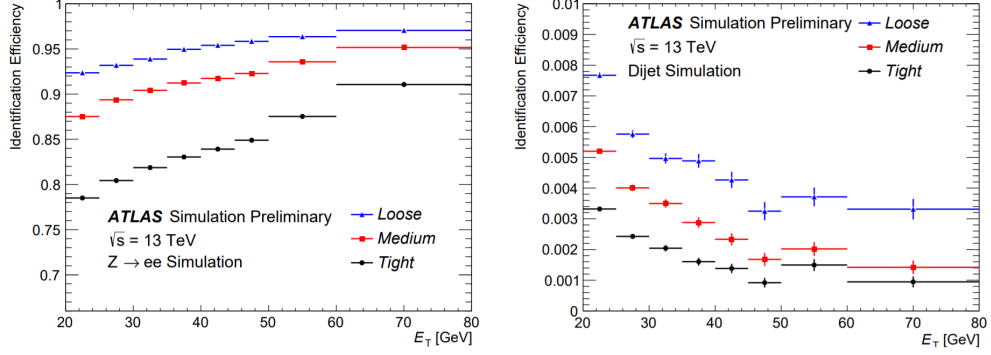


Fig. 4.6 The efficiencies of three electron ID WPs from $Z \rightarrow ee$ (left) events and hadrons misidentified as electrons estimated using di-jet MC samples (right).

from other, non-isolated electron candidates, like the electrons from converted photons or from heavy flavour hadron decays. There are two kinds of discriminating variables that have been designed:

- **Calorimeter-based variable:** $E_T^{topocone20}$. It's defined as the sum of transverse energies of topological clusters^[53], calibrated at EM scale within a cone of $\Delta R = 0.2$ around the candidate electron cluster. It only consider the clusters with positive reconstructed energy. Besides, a correction as a function of (E_T, η) values is then applied to account for the electron energy leakage outside the cluster.
- **Track-based variable:** $p_T^{varcone20}$. It's calculated as the sum of all transverse momentum of all satisfied tracks within a cone of $\Delta R = \min(0.2, 10\text{GeV}/E_T)$ around the candidate electron track. For the sum calculation, it requires the tracks are originating from the reconstruction PV of hard collision, and exclude the associated tracks of electron itself.

Based on the values of $E_T^{cone0.2}/p_T$ and $p_T^{varcone0.2}/p_T$, a series of working points with different selection requirements are defined. The resulting WPs are divided into two kinds:

- Efficiency targeted working points: varying requirements to obtain a certain isolation efficiency, which can either be a constant or as a function of E_T .
- Fixed requirement working points: set the constant upper thresholds on isolation variables.

The distribution of two discriminating variables are shown in figure 4.7 for $ZZ \rightarrow ee$ events with $E_T > 27\text{GeV}$ and satisfying *Tight* requirement.

4.2.4 Muon

Muons are distinctive signatures in final states of many physics analyses at the LHC which include the Higgs analyses, SM measurements and BSM searches and so on. High

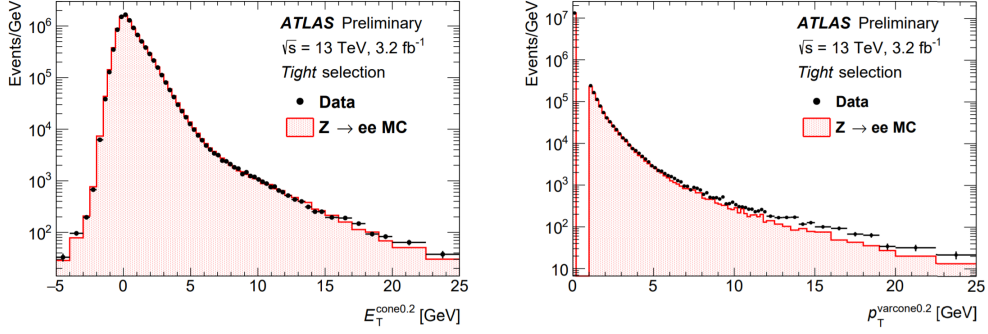


Fig. 4.7 Distributions of $E_T^{cone0.2}$ (left) and $p_T^{varcone0.2}$ (right) for electrons from $ZZ \rightarrow ee$ events in data and MC simulation. The simulated events (full histograms) are normalized to data.

performance of muon reconstruction and identifications are crucial. This section briefly describes some more details of the reconstruction, identification and isolation of muon.

Muon reconstruction

Muon reconstruction is firstly performed in inner detector (ID) and muon spectrometer (MS) independently as given in section 4.2.1. The information from each individual detectors are then combined together to form the muon tracks for physics analyses. The combined ID-MS reconstruction is developed according to several algorithm based on the information from ID, MS and calorimeters. Four different muon types are defined^[44]:

- **Combined (CB) muons:** a combined track is formed by using the reconstructed tracks performed independently in ID and MS with a global refit. To improve the fit quality, the hits from MS may be added to or removed from the track. The outside-in pattern recognition is utilized for the reconstruction of most muons, in which the muons are first reconstructed in MS and then extrapolated inward to match the ID track. In the meantime, the inside-out pattern is also used as a complementary method.
- **Segment-tagged (ST) muons:** a reconstructed track in ID is defined as muon, if it can associated with at least one track segment in MDT or CSC chambers. These ST muons are used when they can only pass across one layer of MS chambers due to their low p_T or falling into regions with less MS acceptance.
- **Calorimeter-tagged (CT) muons:** a reconstructed track in ID is categorized as muon if it's matched to the energy deposit in calorimeter which is recognized with a minimum-ionizing particle. This CT muons have lowest purity amount all types of muons, but it covers the region where ATLAS muon spectrometer is only partially constructed. For the region of $|\eta| < 0.1$ and $15\text{GeV} < p_T < 100\text{GeV}$, the identification of CT muons are optimal.

- **Extrapolated (ME) muons:** the muon is reconstructed based only on the MS track and a loose requirement of originating from the interaction point. In general, this type of muon needs to pass at least two (three) layers of MS chambers to provide a track measurement in barrel (forward) region. ME muons are designed to extend the acceptance for muon reconstruction into the region $2.5 < |\eta| < 2.7$ where ID doesn't cover.

Before collecting those muons for physics analyses, overlap removals are performed between different muon types with the priority of CB > ST > CT, if two types of muons share the same ID track. Besides, the overlaps with ME muons are resolved by analyzing the track hit content, and selecting the track with better fit quality and larger number of hits.

Muon identification

After reconstruction, the muon identification is then performed to further discriminate between signal and background, especially to suppress backgrounds from pion and kaon decays by requiring prompt muons with high efficiency and guaranteeing a robust momentum measurement. The muon identification is defined by using the fit quality of combined track. The variables utilized in judgement for CB tracks include:

- *q/p significance*, the absolute difference between q/g (charge over momentum) of muons measured in ID and MS divided quadratic sum of their corresponding uncertainties;
- ρ' , the absolute value of difference between the p_T (transverse momentum) measured in ID and MS, divided by the p_T of combined track;
- *Normalized χ^2* of the combined track fit;
- *Number of hits in ID and MS*

In addition, some new variables used for *LowPt* muon working point what will be described below include^[54]:

- *Momentum balance significance (MBS)* is computed as momentum difference between the ID and MS standalone measurements with respect to the uncertainty σ on energy lost in the calorimeter system.
- *Scattering neighbor significance (SNS)* is defined to estimated the significance of a change in trajectory along the track, expected in the presence of a hadron decaying to a muon.
- *Scattering curvature significance (SCS)* is defined as the normalized integral of the scattering angle significances, corrected for large kinks along the trajectory.

Five selection levels are developed to satisfy the different needs for different physics

goals: *LowPt*, *Loose*, *Medium*, *Tight* and *HighPt*. The *Tight*, *Medium*, *Loose* are subsets from the tighter one to looser one. More detailed definition of each working point is given as follow:

- *Loose*: this working point is designed to maximize the reconstruction efficiency while keeping good-quality of muon tracks. And they are specifically developed for reconstructing the Higgs boson candidates from four-lepton final states. All four muon types are used for this selection level. The CB and ME muons passing Medium WP that will mentioned below are all included into Loose category. In addition, the CT and ST muons are restricted to $|\eta| < 0.1$ region. In the range of $|\eta| < 2.5$, around 97.5% Loose muons are CB muons, and about 1.5% are CT while remaining 1% are ST muons.
- *Medium*: this working point is the default criteria of muon identification in ATLAS. This selection minimizes the systematic uncertainties of muon reconstruction and calibration. In this category, we only use CB and ME muons. For CB muons, at least 3 hits in at least two layers of MDT is required, except $|\eta| < 0.1$ region, in which tracks with ≥ 1 MDT layer but ≤ 1 MDT hole layer are allowed. For ME muons, at least 3 MDT/CSC layers is required. Furthermore, a loose cut on the compatibility between measured momentum in ID and MS is applied to reduce the fake muons from hadrons misidentification. Besides, the q/p-significance is required to be less than 7.
- *Tight*: this working point is used to maximize the purity of muons but with sacrifice of some selection efficiency. Only CB muons with hits in ≥ 2 stations of MS and passing Medium criteria are selected. In addition, the normalized χ^2 of combined track fit should be smaller than 8. Then, a two-dimensional cut of q/p-significance and ρ' is adopted as a function of muon p_T to ensure tighter background rejection for momentum below 20 GeV, in which the fake rate is usually higher.
- *High- p_T* : this set of selections aims to maximize the momentum resolution for tracks with $p_T > 100\text{GeV}$ region. The selection is especially optimized for searching high-mass Z' and W' resonances. CB muons satisfying Medium selection and with ≥ 3 hits in 3 MS stations are chosen. The specific region in MS where alignment is suboptimal are removed as a precaution.
- *Low- p_T* : this type of muon is newly designed for physics analyses with ATLAS software release version 21. It's designed to obtain a optimal muon identification with very low transverse momentum of $3\text{GeV} < p_T < 5\text{GeV}$, which is crucial for B-physics measurement in ATLAS. In this muon requirement, only CB muons are

used. In the range of $|\eta| < 1.3$, it requests muons hit at least one MS station; in $1.3 < |\eta| < 1.55$, a least two MS stations are required; while in region of $|\eta| > 1.55$, *Medium WP* is required. In addition, cuts are applied to suppress fakes: $|\text{MBS}| < 3.0$, $|\text{SNS}| < 3.0$ and $|\text{SCS}| < 3.0$.

Figure 4.8 and 4.9 show the selection efficiency of different muon identification working points. For *Medium*, *Tight* and *High- p_T* : $Z \rightarrow \mu\mu$ events with $p_T > 10\text{GeV}$ are used for measurement. In addition, the top plot also shows the efficiency of the *Loose* selection (squares), in which the Loose and Medium selections differ significantly in region of $|\eta| < 0.1$. For *LowPt*, $J/\Psi \rightarrow \mu\mu$ events with $3\text{GeV} < p_T < 10\text{GeV}$ are used for measurement.

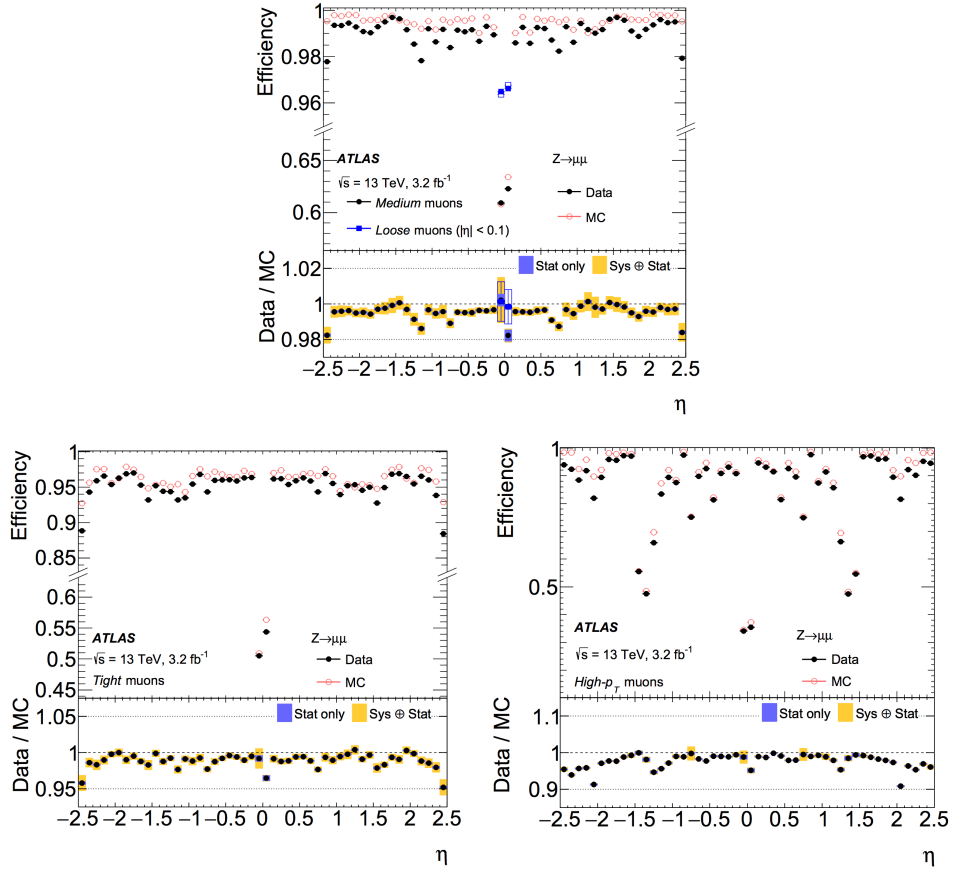


Fig. 4.8 Muon reconstruction efficiency as a function of η for: Medium (and Loose), Tight and High- p_T working points.

Muon isolation

Similar as electron, the muon isolation is used to further distinguish the prompt muon from non-prompt backgrounds. There are also two types of isolation variables for muon:

- **Calorimeter-based variable:** $E_T^{\text{topocone}20}$. It's defined as the sum of the transverse energy of topological clusters within a cone of size $\Delta R = 0.2$ around the candi-

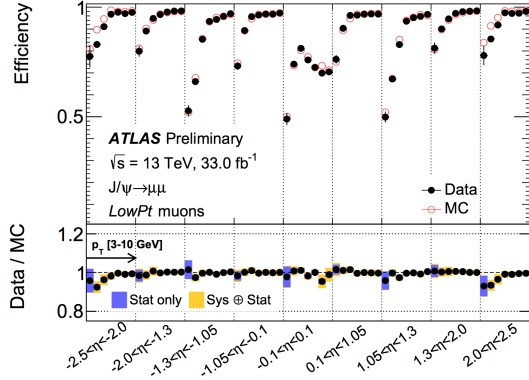


Fig. 4.9 Muon reconstruction efficiency for Low- p_T working point as a function of η .

date muon, after subtracting the contribution from the energy deposit of the muon itself and correcting for pile-up effects. The contributions from pile-up and underlying events are computed using the ambient energy-density technique^[55] and are corrected on an event-by-event basis.

- **Tracked-based variable:** $p_T^{varcone30}$. It's computed as the scalar sum of the transverse momenta of the tracks with $p_T > 1\text{GeV}$ in a cone size of $\Delta R = \min(10\text{GeV}/p_T^\mu, 0.3)$ around the candidate muon whose transverse momenta is p_T^μ after excluding the muon track itself. This p_T -dependent cone size can help to improve the performance for muons produced in the decay of particles with a large transverse momentum.

Then the isolation selections are applied based on *relative isolation variables*, which are computed as the ratio of the track- or calorimeter-based isolation variables to the transverse momentum of the muon. Figure 4.10 shows the distribution of those relative isolation variables by using $Z \rightarrow \mu\mu$ events and passing *Medium* identification criteria.

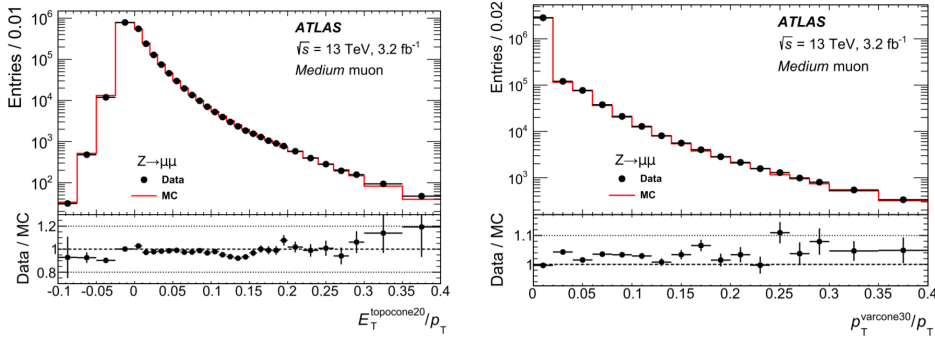


Fig. 4.10 Distributions of the calorimeter-based (right) and the track-based (left) relative isolation variables measured in $Z \rightarrow \mu\mu$ events.

4.2.5 Jets

Jets are another important features for many physics analyses at the LHC, and especially the key signatures for vector boson fusion/scattering (VBF/VBS) processes. In ATLAS detector, jets are reconstructed as groups of topologically associated energy deposits in the calorimeters, tracks associated with charged particles measured in the inner tracking detector, or simulated particles. This section will introduce the jet reconstruction, jet energy scale (JES) calibration and the b-jet tagging technical.

Jet reconstruction

Jets are reconstructed using anti- k_t algorithm^[56] and with radius parameter of $R = 0.4$ in most cases. The FastJet software package^[57] is utilized for jet finding and reconstruction. A collection of four-vectors are used as inputs at each combination step in jet clustering, the total four-momentum is therefore computed as the sum of four-vector of all its constituents. There are three types of jets in ATLAS:

- *Truth jets*: the inputs to jet algorithm are simulated particles.
- *Track jets*: the inputs are charged tracks measured from inner detector.
- *Calorimeter jets*: the inputs are energy deposits in calorimeters.

Figure 4.11 shows the schematic of ATLAS jet reconstruction.

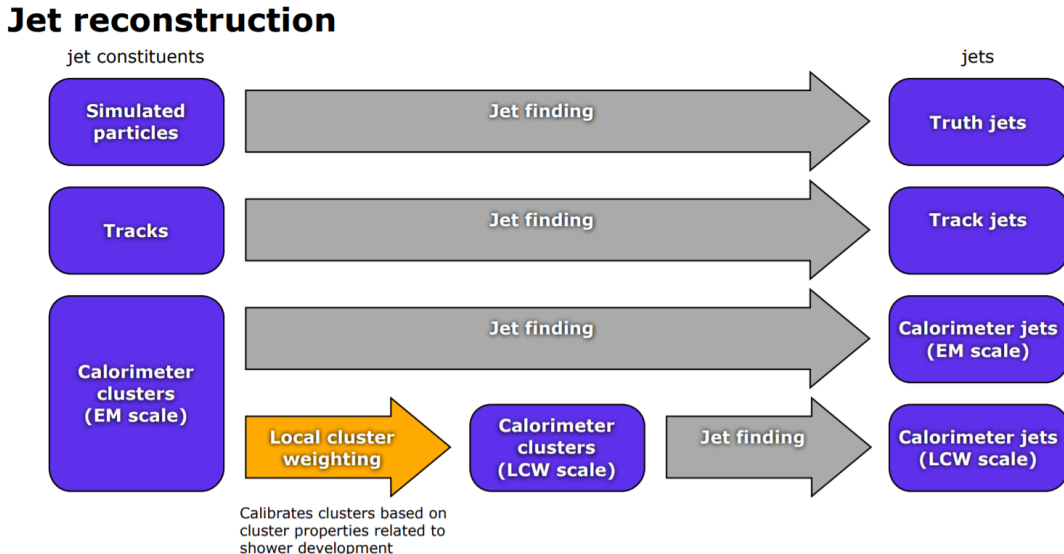


Fig. 4.11 A overview schematic of ATLAS jet reconstruction^[58].

The *calorimeter jets* are reconstructed using a set of three-dimensional, positive-energy topological clusters (topo-clusters) made of calorimeter cell energies as input to the anti- k_t algorithm^[59]. Topo-clusters are built from near-by calorimeter cells that contains a significant energy above a noise threshold, which is estimated from measurements of calorimeter electronic noise and simulated pile-up noise. Those calorimeter cell ener-

gies are measured at electromagnetic energy scale (EM scale) corresponding to the energy deposited by electromagnetically interacting particles. And jets passing a p_T threshold of 7 GeV are reconstructed with the anti- k_t algorithm.

The *truth jets* are reconstructed also using anti- k_t algorithm with $R = 0.4$ by using final-state, stable particles from MC simulation as inputs. It requires the candidate particles with lifetime $c_\tau > 10\text{mm}$ and muons, neutrinos, and excludes particles from pile-up. Truth jets with $p_T > 7\text{GeV}$ and $|\eta| < 4.5$ are then used for jets calibration that will be mentioned later.

The *track jets* are reconstructed from charged particles within the full acceptance of inner detector ($|\eta| < 2.5$). The track reconstruction has been introduced in section 4.2.1. Reconstructed jets with $p_T > 500\text{MeV}$ and associated with primary vertex are then selected. Tracks are assigned to jets using ghost association^[55], a procedure that treats selected tracks as four-vectors of infinitesimal magnitude during the jet reconstruction and assigns them to the jet with which they are clustered. In addition, muon track segments are used as a compensation for those uncaptured jet energy from energetic particles passing through the calorimeters without fully being absorbed. The segments are tracks reconstructed from hits in MS and assigned to jets using the method of ghost association mentioned above as well.

Jet energy scale calibration

Figure 4.12 depicts an overview of ATLAS jet calibration scheme for EM-scale calorimeter jets. This procedure restores the jet energy scale to that of truth jets, which is reconstructed at the particle-level. Each step of the calibration corrects the full four-momentum unless otherwise stated, scaling the jet p_T , energy, and mass.

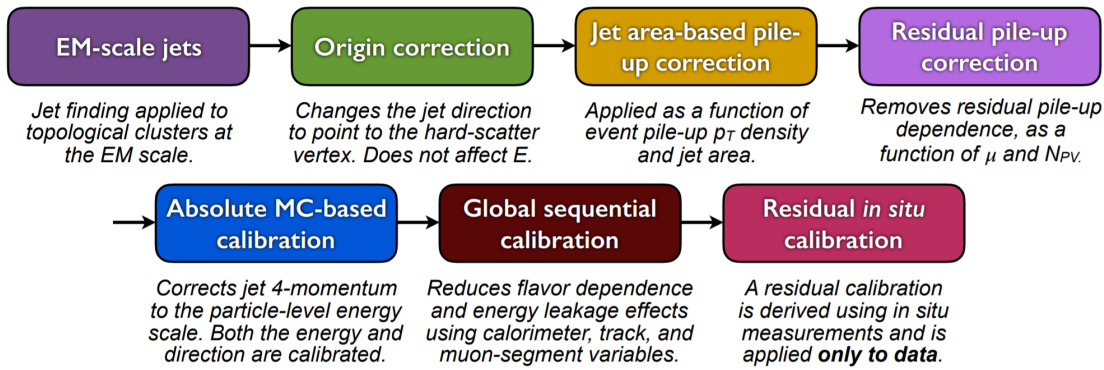


Fig. 4.12 A overview schematic of ATLAS jet calibration^[59].

First of all, the origin correction recompute the four-momentum of jets to point them to the hard-scatter primary vertex instead of the centre of detector, and in the meantime keep the jet energy unchanged. This correction improves the η resolution of jets for roughly

25% at a jet p_T of 20 GeV and > 5 times improvement for jet with p_T above 200 GeV, as measured from the difference between reconstructed jets and truth jets in MC simulation. Secondly, the pile-up correction is adopted to remove the excess energy due to in-time and out-of-time pile-up, which consists of two processes: an area-based p_T density subtraction applied on the top of each event; and a residual correction derived from the simulation. Thirdly, the absolute JES calibration corrects the jet four-momentum to the particle-level energy scale, using truth jets in di-jet MC events. Furthermore, the step of global sequential calibration use calorimeter, track and MS-based variables to reduce the flavor dependence and energy leakage effects. Finally, the residual in situ calibration is adopted to correct jets in data by using well-measured objects eg. photons, Z bosons and calibrated jets.

B-jet tagging

Tagging of b-jets plays a important role in many physics analyses involving b- or t-quark. On the other hand, lots of analyses need to apply b-jet veto to suppress top-antitop process. There are three major types of algorithms that have been developed to distinguish b-jet from light-quark (u,d,s) jets^[60]:

- **Impact parameter based algorithms (IP2D and IP3D):** b-hadrons usually have long lifetime (~ 1.5 ps, $c_\tau \sim 450 \mu\text{m}$), which leads to large impact parameter for tracks produced from b-hadron decay. The impact parameter taggers are developed based on these variables. The IP2D tagger makes use of the transverse impact parameter significance $d_0/\sigma(d_0)$ as discriminant, while IP3D tagger uses two-dimensional discriminant of both transverse and longitudinal impact parameter significances: $d_0/\sigma(d_0)$ and $z_0 \sin\theta/\sigma(z_0)$.
- **Secondary vertex finding algorithm (SV1)** makes use of the secondary vertex formed by decay products of b-hadron within the jet. All track pairs within a jet are tested for a two-track vertex hypothesis, and removed if they are likely to originate from a long-live particle decay (eg. K_s or Λ), hadronic interactions or photon conversions. After that, a new vertex is fitted with all tracks from remaining two-track vertices, and the outliers are removed from this set of tracks.
- **Decay chain multi-vertex algorithm (JetFitter)**^[61] exploits the topological structure of weak b- and c- hadron decays inside the jet and tries to reconstruct the full b-hadron decay chain. A Kalman filter is adopted to find a common line between primary vertex and b-/c- vertices, as well as their position in this line, which gives an approximated flight path for the b-hadron. In this approach, the b- and c-hadron vertices, whenever resolution allows, can be resolved, even when there is only a

single track associated to them.

The final discrimination commonly used in many physics analyses is called **Multivariate Algorithm (MV2)**, which is based on Boosted Decision Tree (BDT) implemented in the TMVA package^[62] by combining the outputs from underlying taggers mentioned above. The MV2 was trained using jets in $t\bar{t}$ sample, where b-jets are treated as signal and c- and light-flavor jets are treated as backgrounds. There are three kinds of MV2 depending on the fraction of c-jets in background for training: $MV2c00$, $MV2c10$ and $MV2c20$. Figure 4.13 presents the output score of MV2c10 for different flavor jets.

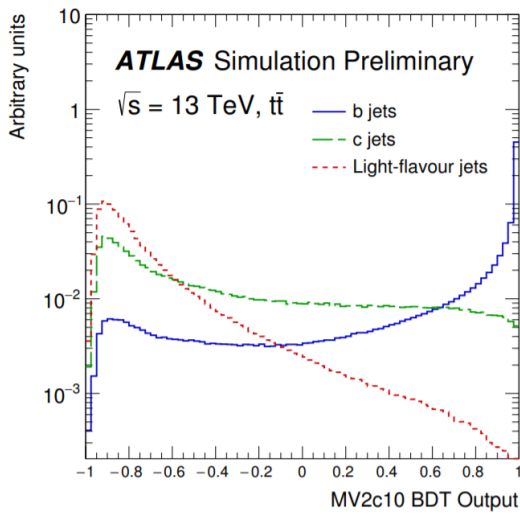


Fig. 4.13 MV2c10 BDT output for b- (solid blue), c- (dashed green) and light-flavour (dotted red) jets in $t\bar{t}$ events^[60].

4.2.6 Missing transverse energy

Many interesting physics processes are with the involvement of neutrinos. Since they do not interact with any materials in the detector, neutrinos cannot be detected directly; but instead, they can result in imbalance in the plane transverse to the beam axis, in which momentum conservation is assumed. It is known as the missing transverse momentum denoted as E_T^{miss} , which is obtained from the negative vector sum of the momenta of all particles detected in a proton-proton collision event.

The E_T^{miss} is measured using selected, reconstructed and calibrated hard objects in an event. Its x- and y- components can be calculated as follow^[63]:

$$E_{x(y)}^{miss} = E_{x(y)}^{miss,e} + E_{x(y)}^{miss,\gamma} + E_{x(y)}^{miss,\tau} + E_{x(y)}^{miss,jets} + E_{x(y)}^{miss,\mu} + E_{x(y)}^{miss,soft} \quad (4.2)$$

where each object term is given by the negative vectorial sum of the momenta of the respective calibrated objects. The calorimeter signals are associated with the recon-

structed objects in the following order: electrons, photons, hadronically decaying taus, jets, muons. The soft term is reconstructed from detected objects not match any hard object passing the selections, but associated with the primary vertex. Details of applied selections for each term are summarized in table 4.1.

Table 4.1 Overview of the contributions to E_T^{miss} .

Objects contributing to E_T^{miss}				
Priority	Type	Selections	Variables	Comments
(1)	e	$ \eta < 1.37 \text{ or } 1.52 < \eta < 1.47$ $p_T > 10GeV$	$E_T^{miss,e}$	all e^\pm passing kinematic selections and medium reconstruction quality
(2)	γ	$ \eta < 1.37 \text{ or } 1.52 < \eta < 1.47$ $p_T > 25GeV$	$E_T^{miss,\gamma}$	all γ passing kinematic selections and tight reconstruction quality, and without signal overlap with (1)
(3)	τ_{had}	$ \eta < 1.37 \text{ or } 1.52 < \eta < 1.47$ $p_T > 20GeV$	$E_T^{miss,\tau}$	all τ_{had} passing kinematic selections and medium reconstruction quality, and without overlap with (1) and (2)
(4)	μ	$ \eta < 2.7$ $p_T > 10GeV$	$E_T^{miss,\mu}$	all μ passing kinematic selections and medium reconstruction quality
(5)	jet	$ \eta < 4.5$ $p_T > 60GeV$ — — — or — — — $2.4 < \eta < 4.5$ $20GeV < p_T < 60GeV$ — — — or — — — $ \eta < 2.4$ $20GeV < p_T < 60GeV$ $JVT > 0.59$	$E_T^{miss,jet}$	all jets passing kinematic selections and reconstruction quality (jet cleaning), and without overlap with (1)–(4)
(6)	ID track	$p_T > 400MeV$ $ d_0 < 1.5mm$ $ z_0 \sin\theta < 1.5mm$ $\Delta R(track, e/\gamma cluster) > 0.05$ $\Delta R(track, \tau_{had}) > 0.2$	$E_T^{miss,soft}$	all ID tracks from the hard-scattering vertex passing kinematic selections and reconstruction quality, and not associated with any particle from (1), (3) or (4), or associated with a jet from (5)

Based on $E_{x(y)}^{miss}$, the magnitude of E_T^{miss} and the azimuthal angle ϕ^{miss} are computed:

$$E_T^{miss} = \sqrt{(E_x^{miss})^2 + (E_y^{miss})^2} \quad (4.3)$$

$$\phi^{miss} = \arctan(E_y^{miss}/E_x^{miss})$$

In equation 4.2, each objects are required to pass certain reconstruction and calibrated criteria and selections mentioned above before taken as inputs.

In figure 4.14, left plot shows the E_T^{miss} distribution for data and MC of $Z \rightarrow \mu\mu$ events, in which there is no genuine missing transverse momentum; and right plot shows the E_T^{miss} distribution for $W \rightarrow e\nu$ events that has genuine (true) missing transverse momentum due to real neutrino.

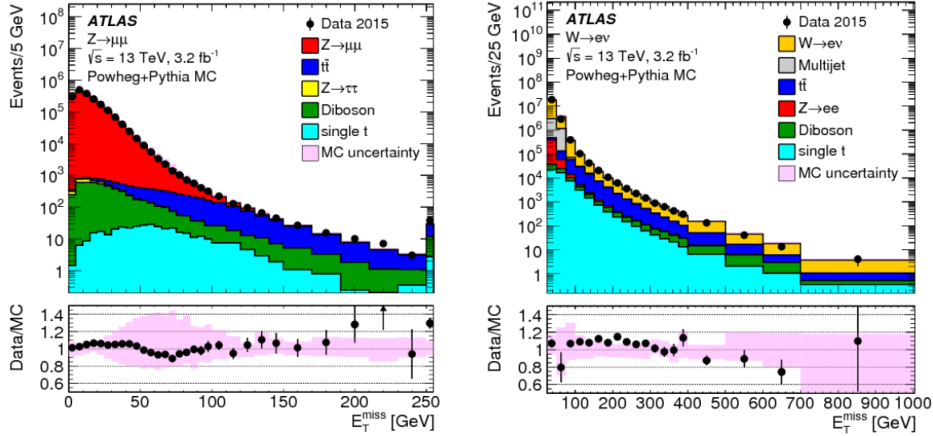


Fig. 4.14 Measured E_T^{miss} distribution for $Z \rightarrow \mu\mu$ events (left) and $W \rightarrow e\nu$ events (right).

Chapter 5 Observation of electroweak ZZ production and measurement of the SM ZZ cross section in the $\ell\ell\ell\ell$ final state using pp collisions data collected by ATLAS detector from 2015~2018

5.1 Introduction

After discovering Higgs boson^[64-65], the examine of electroweak symmetry breaking (EWSB) becomes a main focus at the LHC. In addition to measuring the properties of Higgs boson directly, the vector boson scattering (VBS) process is another key avenue to probe EWSB^[66-68]. As introduced in section 2.1.3, in Standard Model (SM), the Higgs boson acts as "moderator" to unitarize high-energy longitudinal VBS amplitudes at the TeV scale. Therefore, studying high-energy behaviours of VBS is crucial to understand the mechanism of EWSB.

Since no VBS process was observed prior to the LHC era, LHC provides an unexceptionable opportunity to study them due to its unprecedented high energy and luminosity. At LHC, the VBS process is typically studied through the measurements of electroweak (EW) production of two vector bosons radiated from initial-state quarks plus a pair hadronic jets with high energy in the back and forward regions (denoted as EW-VVjj). The quantum chromodynamics (QCD) production of VVjj contains two QCD vertices at the lowest order (denoted as QCD-VVjj) is an irreducible background to the search of EW-VVjj production. The features of EW-VVjj production include a large invariant mass of jet pair (m_{jj}) and a significant separation of rapidity between two jets (Δy_{jj}). Figure 5.1 presents some typical Feynman diagrams of EW- and QCD-ZZjj processes.

The first evidence of the EW-VVjj process was seen in same-sign WW channel (EW- $W^\pm W^\pm jj$) by ATLAS collaboration with 20.3 fb^{-1} 8 TeV data^[69], in which a 3.6σ excess was observed in data over the background-only prediction. In LHC run-2, the observation of EW- $W^\pm W^\pm jj$ process has been reported in both ATLAS and CMS collaboration with 36 fb^{-1} 13 TeV data^[70-71]. In WZ channel (EW-WZjj), an observation with 5.3σ excess was also reported by the ATLAS collaboration recently^[72]. The EW production in ZZ final state (EW-ZZjj) is typically rare, whose fiducial cross section has an order of $O(0.1) \text{ fb}^{-1}$ in the final state where both Z bosons decay leptonically. The EW-ZZjj production was searched by CMS using 35.9 fb^{-1} 13 TeV data, no evidence was found^[73]. But in the meantime, $ZZ \rightarrow 4l$ process offers a extremely clean channel than all the others, with

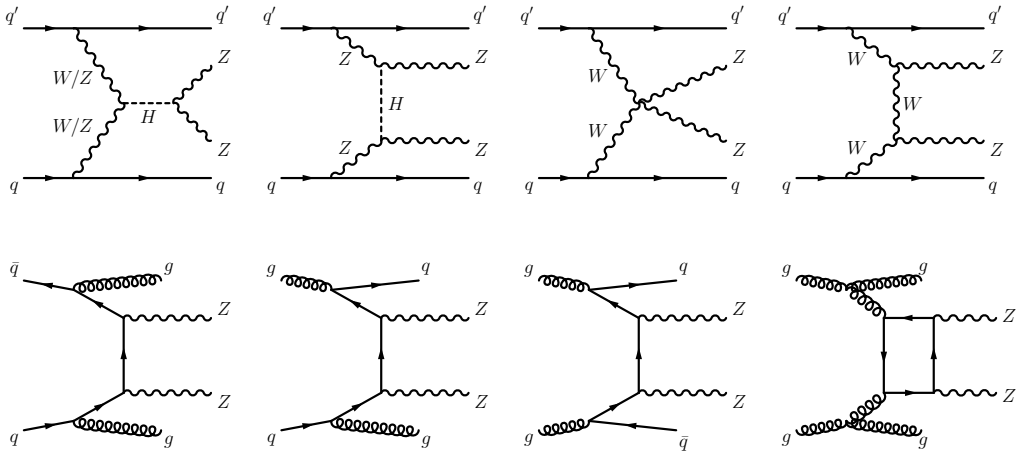


Fig. 5.1 Typical diagrams for the production of $ZZjj$, including the relevant EW VBS diagrams (first row) and QCD diagrams (second row).

more data collected in LHC, the observation of EW-ZZjj becomes possible.

This section will present the first observation of EW-ZZjj production by ATLAS collaboration using the complete set of LHC run-2 data with 139 fb^{-1} luminosity. It is a new milestone in the study of EWSB at LHC, and completes the last missing part of observation of weak boson scattering for *massive bosons*. The thesis will focus on the final state of Z bosons pair decay to four charged leptons with two jets ($\ell\ell\ell\ell jj$), includes both search of EW production and the fiducial cross-sections measurement for the inclusive production of the EW and QCD processes. The ZZjj production involving intermediate τ -leptons from Z decays is considered as signal but has a negligible contribution to the selected event sample. Reducible backgrounds give minor contributions in the $\ell\ell\ell\ell jj$ channel. To further separate the EW signal and the QCD background, multivariate discriminant (MD) is trained using event kinematic information from simulated samples. The MD distribution is then used as discriminant in statistical fit to evaluate the signal strength of EW process.

5.2 Data and MC samples

5.2.1 Data samples

The data sets for this analysis include the full run-2 pp collision data collected by the ATLAS experiment during the years from 2015 to 2018. Data event is only used if it passed the latest Good Run List (GRL) released by the Data Quality group from ATLAS experiment as listed below:

data15_13TeV.periodAllYear_DetStatus-v89-pro21-02_Unknown_PHYS_StandardGRL_All_Good_25ns.xml

data16_13TeV.periodAllYear_DetStatus-v89-pro21-01_DQDefects-00-02-04_PHYS_StandardGRL_All_Good_25ns.xml

```
data17_13TeV.periodAllYear_DetStatus-v99-pro22-01_UncKnown_PHYS_StandardGRL_All_Good_25ns_Triggerno17e33prim.xml
data18_13TeV.periodAllYear_DetStatus-v102-pro22-04_UncKnown_PHYS_StandardGRL_All_Good_25ns_Triggerno17e33prim.xml
```

5.2.2 MC simulations

The EW- $ZZjj$ production (signal) is modelled using MadGraph5_aMC@NLO 2.6.1^[74] matrix elements (ME) calculated in the leading-order (LO) approximation in perturbative QCD (pQCD) and with the NNPDF2.3LO^[75] parton distribution functions (PDF). The VBF Higgs process is also included.

The QCD- $ZZjj$ production is modelled using Sherpa 2.2.2^[76] with the NNPDF3.0NNLO^[77] PDF, in which events with up to one (three) outgoing partons are generated at NLO (LO) in pQCD. The production of $ZZjj$ from the gluon-gluon initial state with a four-fermion loop or with an exchange of the Higgs boson has an order of α_S^4 in QCD, and is not included in the Sherpa simulation. A separate gg induced $ZZ + 2\text{jets}$ sample is modelled using Sherpa 2.2.2 with the NNPDF3.0NNLO PDF, and with an additional 1.7 k-factor^[78] being applied.

Then the interference between EW- and QCD- $ZZjj$ is modelled with MadGraph5_aMC@NLO 2.6.1 calculated at LO.

The diboson productions from QCD $WW \rightarrow llqq$ as well as QCD and EW $WZ \rightarrow llqq$ are modelled using Sherpa 2.2.2 with the NNPDF3.0NNLO PDF. The productions of semileptonic decays ($WW \rightarrow llqq$ and $WZ \rightarrow qqll$) are modelled using Powheg-Box v2^[79] with the CT10 PDF^[80]. The triboson production is modelled using Sherpa 2.2.2 with the NNPDF3.0NNLO PDF.

For top-quark pair ($t\bar{t}$) production, the Powheg-Box v2 is used with the CT10 PDF. The single top-quark production in t -channel, s -channel and Wt -channel were simulated using the Powheg-Box v1 event generator^[81–83]. The productions of $t\bar{t}$ in association with vector boson(s) ($t\bar{t}V$) is modelled with MadGraph5_aMC@NLO 2.3.3 for $t\bar{t}W$ and $t\bar{t}Z$ with $Z \rightarrow \nu\nu/qq$ decays, with Sherpa 2.2.1 for $t\bar{t}Z$ with the Z to dilepton decays, and with MadGraph5_aMC@NLO 2.2.2 for $t\bar{t}WW$ respectively.

The $Z+jets$ processes are modelled using Sherpa 2.2.1 with the NNPDF3.0NNLO PDF, in which the ME is calculated for up to two partons with next-to-leading-order (NLO) accuracy in pQCD and up to four partons with LO accuracy.

For all the samples except those from Sherpa, the parton showering is modelled with Pythia8^[38] using the NNPDF2.3^[75] PDF set, and the A14 set of tuned parameters^[84]. For Sherpa samples, the parton showering is simulated within the programme.

All simulated events were processed with detector response simulated based on

Geant4 described in section 4.1. In addition, simulated inelastic pp collisions were overlaid to model additional pp collisions in the same and neighbouring bunch crossings (pile-up), and reweighted to match the pile-up conditions in data. Moreover, all simulated events were processed using the same reconstruction algorithms as data. And the leptons’ and jets’ reconstruction, energy scale and resolution, and the leptons’ identification, isolation, trigger efficiencies for simulated events, as described in section 4.2, were all corrected to match the data measurements.

5.3 Objects and Event selection

5.3.1 Objects selection

The selection of analysis relies on the definition of multiple objects: *electrons*, *Muons*, and *jets*. Details of definitions for each objects are described as below:

Muon: To increase the acceptance range in reco-level for $\ell\ell\ell\ell jj$ channel, all four types of muons (CB, ST, CT, ME muons, described in section 4.2.4) are used. The identified muons are then required to pass $p_T > 7\text{GeV}$ and $|\eta| < 2.7$, and satisfy the *Loose* identification criterion (see definition in sec 4.2.4). The impact parameter cuts are further applied to suppress the contribution from cosmic muons and non-prompt muons, with the value of: $|d_0/\sigma(d_0)| < 3.0$ and $|z_0 \sin\theta| < 0.5\text{mm}$, where d_0 is the transverse impact parameter relative to the beam line, $\sigma(d_0)$ is its uncertainty, and z_0 is the longitudinal impact parameter relative to the primary vertex. In order to avoid muons associated with jets, all muons are required to be isolated and pass *FixedCutLoose* isolation criteria, which required $E_T^{\text{topocone}20}/p_T < 0.3$ and $p_T^{\text{varcone}30}/p_T < 0.15$.

Electron: As described in section 4.2.3, electrons are reconstructed from energy deposits in the EM calorimeter matched to a track in the inner detector. The electron candidates must satisfy the *Loose* criterion valuing by the likelihood-based (LH) method. And electrons are required to have $p_T > 7\text{GeV}$ and $|\eta| < 2.47$. Moreover, the impact parameter requirements of $|d_0/\sigma(d_0)| < 5.0$ and $|z_0 \sin\theta| < 0.5\text{mm}$ are applied. Same as muon, all electrons are required to satisfy *FixedCutLoose* isolation criteria of $E_T^{\text{topocone}20}/p_T < 0.2$ and $p_T^{\text{varcone}20}/p_T < 0.15$.

Jets: Jet are key signatures for VBS processes. This analysis use the jets clustered using the anti- k_t algorithm with radius parameter $R = 0.4$, more details of jets’ reconstruction can be found in section 4.2.5. The jets are required to satisfy $p_T > 30$ (40) GeV in the $|\eta| < 2.4$ ($2.4 < |\eta| < 4.5$) region. To further reduce the effects of pile-up jets, a jet vertex tagger (JVT) is applied to jets with $p_T < 60$ GeV and $|\eta| < 2.4$ to select jets from

hard-scattering vertex^[85].

Overlap removal: An overlap-removal procedure is applied to selected leptons and jets in this analysis. To enhance the selection efficiency, leptons are given higher priority to be kept when overlapping with jets. With this lepton preferred method, the events of EWK signal after selection increases about 19% while background only increases 14%. More details of the strategy is summarized in table 5.1.

	Reference objects	Criteria
Remove electrons	electrons	Share a track or have overlapping calorimeter cluster. Keep higher p_T electron
Remove muons	electrons	Share track and muon is calo-tagged
Remove electrons	muons	Share track
Remove jets	electrons	$\Delta R_{e-jet} < 0.2$
	muons	$\Delta R_{\mu-jet} < 0.2$ OR muon track is ghost-associated to jet AND ($N_{Trk}(jet) < 3$ OR ($p_T^{jet}/p_T^{\mu} < 2$ and $p_T^{\mu}/\sum_{Trk} p_t > 0.7$))

Table 5.1 Overlap removal criteria between pre-selection objects for the $\ell\ell\ell\ell$ channel. The overlap removal follows the order shown in this table. Once an object has been marked as removed, it does not participate in the subsequent stages of the overlap removal procedure.

5.3.2 Event selection in reconstruction level

The events are required to additionally be recorded by single or multi-lepton triggers, with transverse momentum (p_T) thresholds varying from 8 to 26 GeV. The overall trigger efficiency for selected inclusive $\ell\ell\ell\ell jj$ signal events in the analysis region are from 95 to 99%.

The $\ell\ell\ell\ell$ quadruplets are formed by two opposite-sign, same-flavour (OSSF) lepton pairs (l^+l^-), in which leptons are required to be separated by $\Delta R > 0.2$ in table 5.1. At most one muon is allowed to be ME or CT muon. The p_T threshold of first three leading muons are 20, 20 and 10 GeV. If more than one quadruplets are found, the one with minimum sum of difference between two muon pair masses and Z boson mass ($|m_{l_1^+l_1^-} - m_Z| + |m_{l_2^+l_2^-} - m_Z|$) is selected. Both two dilepton pair masses are required to be between 66 to 116 GeV. In addition, the invariant masses of all possible OSSF pairs are required to be greater than 10 GeV to reject events from J/ϕ or Y decay.

For VBS topology, the two most energetic jets in different detector side ($y_{j1} \times y_{j2} < 0$)

are selected. Furthermore, the invariant mass of two jets (m_{jj}) is required to be greater than 300 GeV, while Δy_{jj} is required to be larger than 2. Table 5.2 summarizes the above selection requirements, which is defined as signal region (SR).

Electrons	$p_T > 7 \text{ GeV}, \eta < 2.47$ $ d_0/\sigma_{d_0} < 5 \text{ and } z_0 \times \sin \theta < 0.5 \text{ mm}$
Muons	$p_T > 7 \text{ GeV}, \eta < 2.7$ $ d_0/\sigma_{d_0} < 3 \text{ and } z_0 \times \sin \theta < 0.5 \text{ mm}$
Jets	$p_T > 30 (40) \text{ GeV for } \eta < 2.4 (2.4 < \eta < 4.5)$
ZZ selection	$p_T > 20, 20, 10 \text{ GeV for the leading, sub-leading and third leptons}$ Two OSSF lepton pairs with smallest $ m_{\ell^+\ell^-} - m_Z + m_{\ell'^+\ell'^-} - m_Z $ $m_{\ell^+\ell^-} > 10 \text{ GeV for lepton pairs}$ $\Delta R(\ell, \ell') > 0.2$ $66 < m_{\ell^+\ell^-} < 116 \text{ GeV}$
Dijet selection	Two most energetic jets with $y_{j_1} \times y_{j_2} < 0$ $m_{jj} > 300 \text{ GeV and } \Delta y_{jj} > 2$

Table 5.2 Summary of selection of physics objects and candidate events at detector level in the $\ell\ell\ell\ell jj$ signal region.

5.4 Background estimation

Table 5.3 summarizes the background yields for $ZZjj \rightarrow \ell\ell\ell\ell jj$ channel in 139 fb^{-1} . Uncertainties on the predictions include both statistical and systematic components. "Others" includes minor contributions from non- ZZ processes including $Z+jets$, top-quark, triboson and $t\bar{t}V$ processes. Detail of estimation for each source will be described below.

Process	$\ell\ell\ell\ell jj$
EW- $ZZjj$	20.6 ± 2.5
QCD- $q\bar{q} \rightarrow ZZ$	77 ± 25
QCD- $gg \rightarrow ZZ$	13.1 ± 4.4
Others	3.2 ± 2.1
Total	114 ± 26
Data	127

Table 5.3 Observed data and expected signal and background yields in 139 fb^{-1} of luminosity. Minor backgrounds are summed together as 'Others'. Uncertainties on the predictions include both statistical and systematic components.

5.4.1 QCD backgrounds

The QCD- $ZZjj$ production, which include both qq and gg induced processes, is an irreducible background in the search of EW- $ZZjj$ production. A QCD-enriched control region (CR) is defined to constrain the contribution by reverting either the m_{jj} or Δy_{jj} requirements:

$$m_{jj} < 300 \text{ GeV} \text{ or } \Delta y_{jj} < 2$$

Then the normalization factor of QCD- $ZZjj$ process is included into statistical fit as a float parameter to properly treat the uncertainty correlations between SR and CR, while the shapes are taken from MC simulation. Table 5.4 shows the event yields of each background components in this CR. Uncertainties are statistical one only. The distributions of

Process	$\ell\ell\ell\ell jj$
EW- $ZZjj$	3.9 ± 0
QCD- $ZZjj$	136.9 ± 0.6
QCD- $ggZZjj$	16.8 ± 0.1
Diboson	0.3 ± 0.1
Triboson	1.6 ± 0.1
$Z+jets$	0
$t\bar{t}$	0
Total	159.5 ± 0.62
Data	152

Table 5.4 Observed data and expected signal and background yields in 139 fb^{-1} of luminosity.
Diboson background in table includes all the other diboson processes discussed in section 5.2.2, except those with four-lepton final state. Uncertainties include only MC statistic. No events from $Z+jets$ and $t\bar{t}$ MC samples pass the selection, and are indicated as 0 in the table.

4l and di-jet invariant mass in QCD CR are shown in figure 5.2.

5.4.2 Reducible backgrounds

Backgrounds from $Z+jets$, top-quark and WZ processes are estimated by data-driven method. These events usually contain two or three leptons from Z/W decays, together with heavy-flavor jets or misidentified components of jets reconstructed as leptons called "fake leptons". A *fake factor* method is used to estimate this backgrounds, in which the lepton misidentification is measured in data regions with enhanced contributions from $Z+jets$ and top-quark processes:

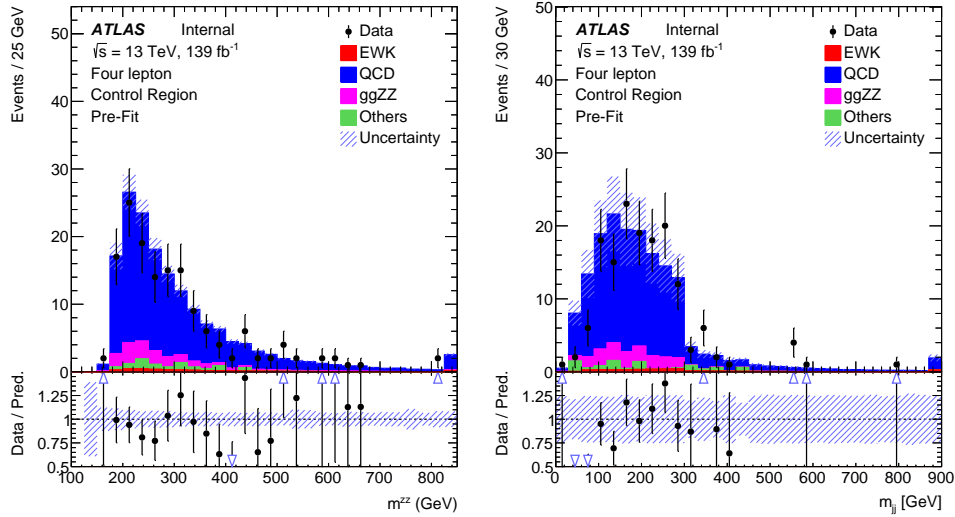


Fig. 5.2 Pre-fit m_{ZZ} and m_{jj} distribution in QCD-enriched CR.

1. Define a dedicated background dominant region to derive the fake factor for this background. The *fake factor* is defined as:

$$\mathcal{F} = \mathcal{N}_{good}/\mathcal{N}_{pool} \quad (5.1)$$

where \mathcal{N}_{good} refers to the number of good leptons passing all SR selection, while \mathcal{N}_{pool} denotes the number of poor leptons passing most SR selection but fail one certain requirement.

2. Define a $\ell\ell\ell\ell jj$ fake control region, where one or two leptons pass *poor* requirement while all the other leptons are required to have SR selection.
3. The number of fake events are calculated as:

$$\mathcal{N}_{fake} = (N_{gggp} - N_{ggpp}^{ZZ}) \times \mathcal{F} - (N_{ggpp} - N_{ggpp}^{ZZ}) \times \mathcal{F}^2 \quad (5.2)$$

with the subtraction of ZZ contribution, and the double counting between (N_{gggp} and N_{ggpp}).

For the definition of *poor* leptons: The poor electrons are defined as failing "Fixed-CutLoose" isolation requirement or "LooseLH" electron ID requirement but satisfying "VeryLooseLH" WP. The poor muons are required to fail the "FixedCutLoose" isolation requirement or invert the impact parameter cut to be $3 < d_0/\sigma(d_0) < 10$. The dedicated $Z+jets$ and $t\bar{t}$ dominant regions are defined to calculate the fake factor respectively in the following subsections.

1. Fake factor for $Z+jets$

Fake factor for $Z+jets$ background is calculated in $Z+jets$ -enriched region, where events with one SFOS lepton pair around Z mass associated with two jets are selected.

The value of fake factor is driven from data, and as a function of p_T and η as shown in figure 5.3 for electrons and figure 5.4 for muons. During calculation, the contributions from non- $Z+jets$ backgrounds ($t\bar{t}$, ZZ , WZ) have been subtracted from data. The values calculated from $Z+jets$ MC directly are also shown in plots for comparison.

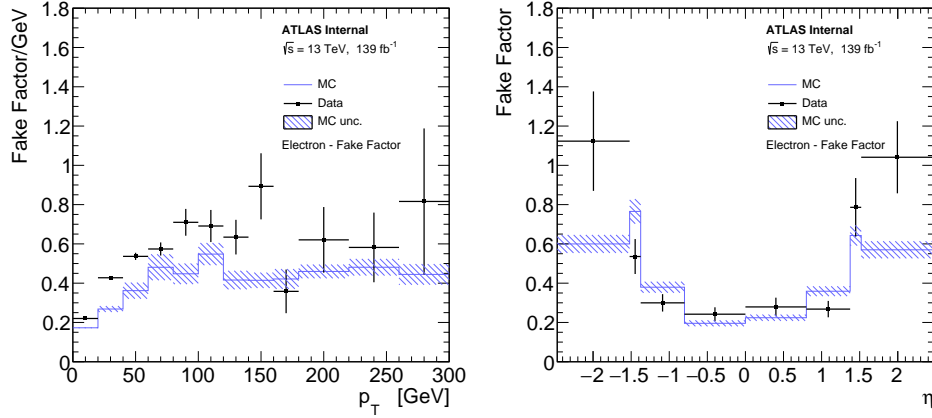


Fig. 5.3 Fake factor for $Z+jets$ background, constructed with additional electron, as a function of p_T (left) and η (right).

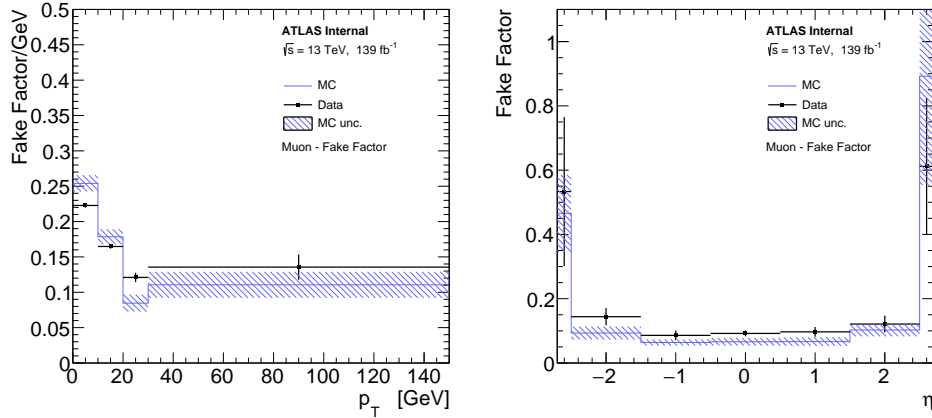


Fig. 5.4 Fake factor for $Z+jets$ background, constructed with additional muon, as a function of p_T (left) and η (right).

2. Fake factor for $t\bar{t}$

The fake factor for $t\bar{t}$ are calculated in $t\bar{t}$ dominated region by selecting one $e\mu$ -pair with additional two jets. For events with three leptons, $m_T^W < 60 \text{ GeV}$ cut is applied to reject the contribution from $t\bar{t} + W$ events. The m_T^W is defined as below:

$$m_T^W = \sqrt{2p_T^{l_3}E_T^{miss} \left[1 - \cos \left(\Delta\phi \left(p_T^{l_3}, E_T^{miss} \right) \right) \right]} \quad (5.3)$$

In addition, at least one b-jet is required to enhance the top component. The fake factors of $t\bar{t}$ calculated from data as the function of p_T and η are shown in figure 5.5 for electrons

and 5.6 for muons. The non- $t\bar{t}$ contributions, which include $Z+jets$, ZZ and WZ , are subtracted from data.

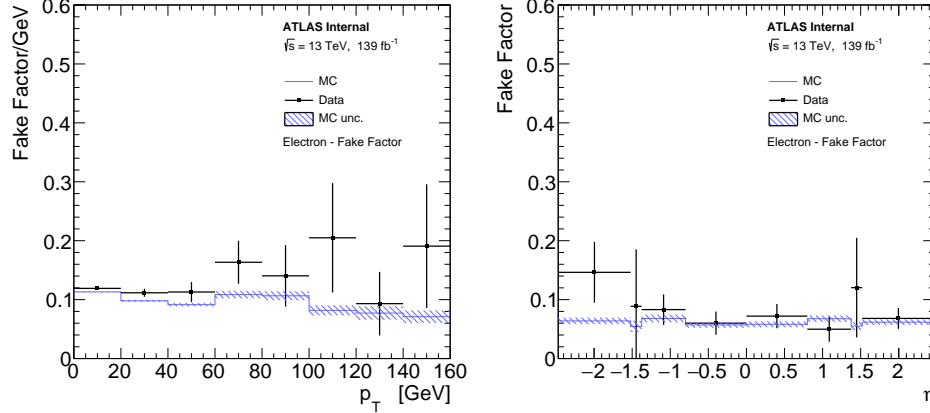


Fig. 5.5 Fake factor for $t\bar{t}$ background, constructed with additional electron, as a function of p_T (left) and η (right).

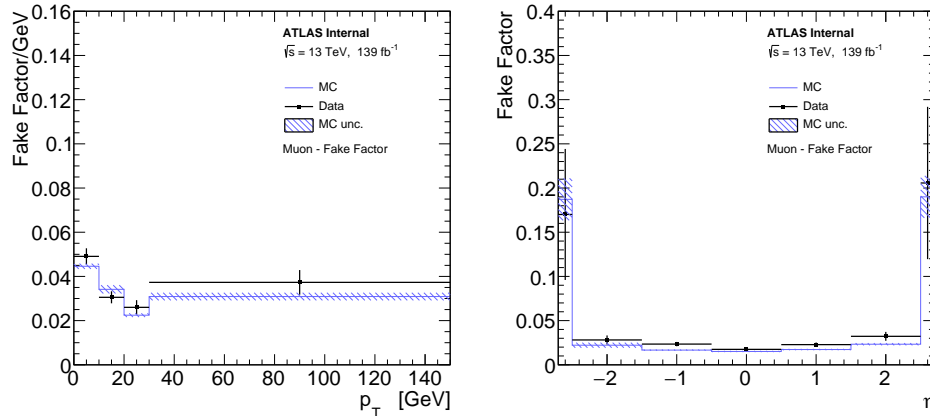


Fig. 5.6 Fake factor for $t\bar{t}$ background, constructed with additional muon, as a function of p_T (left) and η (right).

3. Combination

The fake factors calculated from each dedicated region are then combined together according to their contributions in fake control region described previously. Figure 5.7 shows the m_{jj} distribution with data and major fake backgrounds in three different 4l channels.

4. Systematics of fake estimation and results

The systematics of fake factor method can be measured by varying the parameters and selection requirements in fake factor calculation. In addition, due to the very limited data statistic in $\ell\ell\ell\ell$ channel, to be more conservative, the difference between data measurement and MC simulation are also considered as another systematics component. In detail,

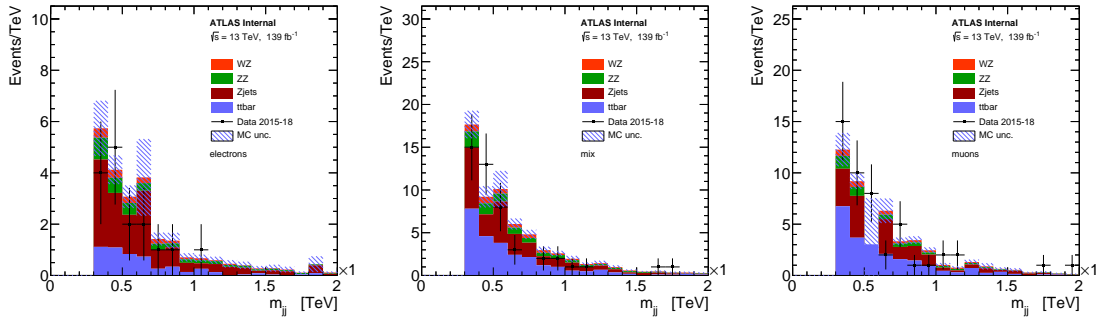


Fig. 5.7 m_{jj} distributions in fake control region in 4e (left), 2e2 μ (middle) and 4 μ (right) channel. The ratios between $Z+jets$ and $t\bar{t}$ ($Z+jets/t\bar{t}$) in each individual channel are: 2.59, 0.95, 0.74.

the sources of systematics that have been included are listed as below:

- Variations of isolation cut for the poor lepton definition up and down scaled by a factor of two.
- Variations of the yields of those subtracted MC in fake control region scaled by 30% up and down.
- The difference of fake factors between driven from data and from MC simulation.
- The difference of fake factors when changing to one bin measurement (instead of p_T or η dependent).
- The statistical uncertainties on fake factor in fake control region.

Table 5.5 summarizes the contribution of fake backgrounds in signal region under different systematic conditions mentioned above as well as the nominal one. Uncertainties of each value in table are statistical one.

channel	4e	2e2 μ	4 μ	inclusive
Nominal estimate	0.678 ± 0.652	1.023 ± 0.740	0.566 ± 0.240	2.268 ± 1.015
F stat. uncertainty varied down	0.698 ± 0.622	0.872 ± 0.652	0.509 ± 0.214	2.079 ± 0.926
F stat. uncertainty varied up	0.657 ± 0.685	1.173 ± 0.840	0.622 ± 0.267	2.452 ± 1.116
One bin F	0.653 ± 0.590	0.594 ± 0.558	0.646 ± 0.313	1.892 ± 0.870
MC F	0.534 ± 0.471	1.415 ± 0.993	0.439 ± 0.184	2.389 ± 1.114
Isolation varied down	0.938 ± 0.686	0.552 ± 0.466	0.215 ± 0.107	1.704 ± 0.837
Isolation varied up	0.723 ± 0.646	1.104 ± 0.739	0.559 ± 0.237	2.386 ± 1.010
MC corr. varied down	0.697 ± 0.695	1.048 ± 0.811	0.832 ± 0.385	2.577 ± 1.136
MC corr. varied up	0.660 ± 0.614	0.984 ± 0.687	0.316 ± 0.159	1.961 ± 0.935

Table 5.5 Fake background estimations in the SR. For the nominal value the 2D fake factor together with the $Z+jets$ and $t\bar{t}$ combination applied. The other lines show the estimations with different uncertainty variations.

5.5 Systematics

The analysis performs both the statistical fit to MD distribution to extract the EW- $Z Z jj$ contributions and the cross section measurements in fiducial volume. Therefore, theoretical and experimental uncertainties may affect the predictions background yields and shapes, correction factors from detector-level to particle-level measurement, as well as the $Z Z jj$ MD shapes and so on. Moreover, the statistical uncertainties of simulated samples are also taken into account. And due to the extremely low cross section of $\ell\ell\ell\ell$ channel, the analysis is still data statistic dominant. This section describes the measurement of both theoretical and experimental systematics for $Z Z jj$ productions. The systematics for fake backgrounds have been elaborated in section 4.

5.5.1 Theoretical systematics

The theoretical systematics on EW- and QCD- $Z Z jj$ processes include the uncertainties from PDF, QCD scale, α_S and parton showering variations. The PDF uncertainty is estimated from envelop of NNPDF internal variations and the difference between nominal and alternative PDF sets, following the PDF4LHC as introduced in section 2.2.1. The QCD scale uncertainty is estimated by varying the nominal renormalization scale (μ_R) and factorisation scale (μ_F) by a factor of 0.5 or 2.0. There are seven different configurations being considered, where the maximum of variations is chosen as final uncertainty. The parton showering uncertainty is estimated by comparing events with different parton showering setting between the nominal Pythia8 and the alternative Herwig7^[86-87] algorithm. The α_S uncertainty is estimated by varying the value of α_S within ± 0.001 . Details of those variation components are summarized in table 5.6. Due to the lack of simula-

Process	EW- $Z Z jj$	QCD- $Z Z jj$
PDFs	NNPDF30lo (nominal), CT14lo	NNPDF30nnlo (nominal), MMHT2014nnlo68cl, CT14nnlo
α_S	0.118	0.117, 0.118 (nominal), 0.119
QCD scale ($[\mu_R, \mu_F]$)	[0.5,0.5], [0.5,1], [1,0.5], [1,1], [1,2], [2,1], [2,2]	[0.5,0.5], [0.5,1], [1,0.5], [1,1], [1,2], [2,1], [2,2]
Parton showering algorithm	Pythia8, Herwig7	-

Table 5.6 Summary of different variations for EW- and QCD- $Z Z jj$ theoretical uncertainties measurement.

tion sample for alternative parton showering on QCD- $Z Z jj$ process, the value of parton showering component is taken from the measurement of EW process.

Table 5.7 summarizes the uncertainties of each theoretical components in fiducial volume, while table 5.8 shows the numbers in QCD-enriched CR region. For QCD process, the uncertainty is QCD scale dominant. Both of them are taken as inputs for statistical fit.

Process	PDF (%)	α_S (%)	QCD scale (%)	Parton shower (%)
EW	+5.9 -5.9		+6.1 -5.6	+3.3 -3.3
qqQCD	+2.0 -1.0	+2.6 -2.6	+34.2 -22.8	

Table 5.7 Summary of theoretical uncertainties for the fiducial volume (SR) for both EW and QCD $q\bar{q}$ -initial processes.

Process	PDF (%)	α_S (%)	QCD scale (%)	Parton shower (%)
EW $\ell\ell\ell\ell$	+6.1 -6.1		+0.8 -1.1	+10.1 -10.1
qqQCD $\ell\ell\ell\ell$	+2.0 -1.0	+2.6 -2.6	+31.5 -22.0	

Table 5.8 Summary of theoretical uncertainties for the control region for EW and qqQCD processes.

The uncertainties of QCD gg -induced process ($gg \rightarrow ZZ$) as the function of MD discriminant is shown in figure 5.8 for both fiducial volume (SR) and QCD CR.

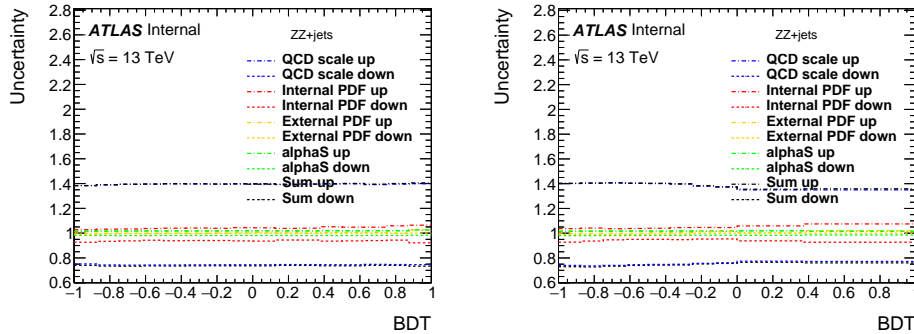


Fig. 5.8 The theoretical uncertainties for $gg \rightarrow ZZ$ background in particle-level SR (left) and CR (right).

5.5.2 Experimental systematics

The major experimental uncertainties are from the luminosity uncertainty, the momentum scale and resolution of leptons and jets, as well as the lepton reconstruction and selection efficiency. Some smaller uncertainties, such as trigger efficiency and pile-up correction, are also considered. Overall, most large systematics are from leptons and jets. Table 5.9 lists the major systematic components from leptons and jets for major processes in $\ell\ell\ell\ell$ channel. The total uncertainties for sources from electron, muon and jet respec-

tively, as well as the sum (quadratic sum) of them are also summarized in this table.

name	EW- $ZZjj$	QCD qq -initial	QCD gg
nominal yield	20.61	76.69	13.10
EG_RESOLUTION_ALL	$\pm^{0.00\%}_{0.03\%}$	$\pm^{0.02\%}_{0.04\%}$	$\pm^{0.01\%}_{1.41\%}$
EG_SCALE_ALL	$\pm^{0.03\%}_{0.05\%}$	-0.04%	$\pm^{0.01\%}_{0.06\%}$
EL_EFF_ID_TOTAL_1NPCOR_PLUS_UNCOR	$\pm^{2.66\%}_{2.58\%}$	$\pm^{2.60\%}_{2.53\%}$	$\pm^{2.65\%}_{2.57\%}$
EL_EFF_Iso_TOTAL_1NPCOR_PLUS_UNCOR	$\pm 0.70\%$	$\pm 0.47\%$	$\pm 0.42\%$
EL_EFF_Reco_TOTAL_1NPCOR_PLUS_UNCOR	$\pm 0.55\%$	$\pm 0.55\%$	$\pm 0.63\%$
JET_EtaIntercalibration_NonClosure	-0.01%	-0.03%	0%
JET_GroupedNP_1	$\pm 1.97\%$	$\pm^{11.82\%}_{10.14\%}$	$\pm^{16.21\%}_{12.92\%}$
JET_GroupedNP_2	$\pm 0.23\%$	$\pm 1.26\%$	+5.3%
JET_GroupedNP_3	$\pm 0.55\%$	$\pm 2.94\%$	$\pm^{3.14\%}_{0.12\%}$
JET_JER_SINGLE_NP	0.11%	+5.47%	+6.31%
JET_JvtEfficiency	$\pm 0.04\%$	$\pm 0.12\%$	$\pm 0.15\%$
MUON_EFF_ISO_STAT	$\pm 0.09\%$	$\pm 0.08\%$	$\pm 0.07\%$
MUON_EFF_ISO_SYS	$\pm 0.54\%$	$\pm 0.55\%$	$\pm 0.56\%$
MUON_EFF_RECO_STAT	$\pm 0.15\%$	$\pm 0.19\%$	$\pm 0.15\%$
MUON_EFF_RECO_STAT_LOWPT	$\pm 0.06\%$	$\pm 0.02\%$	$\pm 0.03\%$
MUON_EFF_TTVA_STAT	$\pm 0.06\%$	$\pm 0.07\%$	$\pm 0.06\%$
MUON_EFF_TTVA_SYS	$\pm 0.03\%$	$\pm 0.4\%$	$\pm 0.03\%$
MUON_ID	$\pm 0.03\%$	$\pm 0.02\%$	<0.001%
MUON_MS	-0.05%	$\pm^{0.04\%}_{0.01\%}$	<0.001%
MUON_SAGITTA_RESBIAS	$\pm 0.01\%$	$\pm 0.02\%$	<0.001%
MUON_SAGITTA_RHO	+1.13%	-0.73%	$\pm 1.00\%$
MUON_SCALE	$\pm 0.02\%$	$\pm^{0.03\%}_{0.02\%}$	<0.001%
PRW_DATASF	$\pm 0.5\%$	$\pm^{0.42\%}_{1.02\%}$	$\pm^{2.17\%}_{1.46\%}$
Electron Exp	$\pm^{2.8\%}_{2.7\%}$	$\pm^{2.70\%}_{2.62\%}$	$\pm^{2.75\%}_{2.64\%}$
Muon Exp	$\pm 1.3\%$	$\pm 1.3\%$	$\pm 1.04\%$
Jet Exp	$\pm 2.0\%$	$\pm^{13.39\%}_{10.64\%}$	$\pm^{18.54\%}_{13.57\%}$
Total experimental uncertainties	$\pm^{3.7\%}_{4.0\%}$	$\pm^{13.72\%}_{11.11\%}$	$\pm^{18.90\%}_{13.57\%}$

Table 5.9 Experimental uncertainties in 4l channel (normalized to 139 fb^{-1}). The "Electron Exp", "Muon Exp" and "Jet Exp" represent the quadrature of the respective sources from electron, muon, and jets.

In addition, the uncertainty of the combined 2015–2018 integrated luminosity is 1.7%^[88], obtained using the LUCID-2 detector^[89] for the primary luminosity measurements.

An systematic uncertainty for MD distribution with different pile-up ($\langle \mu \rangle$) is also

been considered, by comparing the distribution between events with low and high pile-up conditions. A boundary of $< \mu > = 33$ is used to define low/high pile-up according to the average $< \mu >$ for signal (about 34.5) and QCD background (about 33). Figure 5.9 shows the MD distribution in SR (left) and QCD CR (right), the difference as function of MD is then taken into account as additional shape uncertainty for statistical fit.

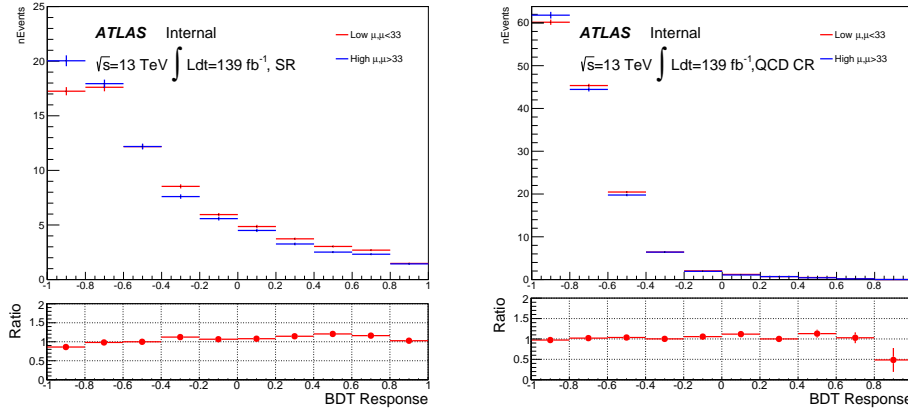


Fig. 5.9 MD distribution between low and high pile-up events for SR (left) and CR (right).

Moreover, a conservative uncertainty is assigned to QCD- $ZZjj$ process by comparing the sample modelled by Sherpa generator (nominal) to MadGraph5_aMC@NLO. The MD shape differences for both SR (left) and QCD CR (right) are shown in figure 5.10. The modelling uncertainty is calculated from the envelope of MD shape difference between nominal and alternative samples as function of MD.

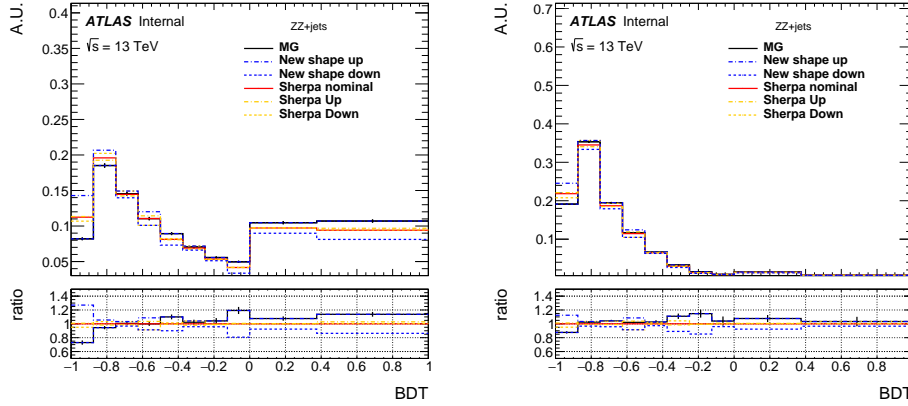


Fig. 5.10 MD shape difference for QCD $q\bar{q} \rightarrow ZZ$ background between different Sherpa theoretical uncertainties and sample from MadGraph5_aMC@NLO on SR (left) and CR (right).

5.6 Measurement of fiducial cross section

The fiducial cross section for the production of inclusive $Z Z j j$, which includes both EW and QCD components, is then measured.

The definition of fiducial volume, which is used for cross section measurement, follows closely to the detector-level selection but use physics objects in "particle-level", which are reconstructed in simulation from stable final-state particles, prior to their interactions with the detector. For electrons and muons, QED final-state radiation is for the most part recovered by adding the four-momenta of surrounding photons that are not originating from hadrons and within an angular distance $\Delta R < 0.1$ to the lepton four-momentum, called lepton "dressing". Particle-level jets are built with anti- k_T algorithm with radius parameter $R = 0.4$ using all final-state particles except leptons and neutrinos as inputs. Comparing to the events selection in detector-level in section 5.3, in particle-level, the selected dilepton pair mass required is relaxed to be within 60 to 120 GeV to reduce the migration effect as well as be more compatibility with previous CMS publication^[73]. All the other kinematics selection requirements are the same as the definition in detector-level.

5.6.1 Calculation of C-factor

C-factor is defined as the ratio between the number of selected events in detector-level and the number of particle-level events in fiducial volume (FV):

$$C = \frac{N_{\text{detector-level}}}{N_{\text{FV}}} \quad (5.4)$$

The C-factor value of each $Z Z j j$ processes calculated from each individual simulation samples are listed in table 5.10 as well as their systematics.

Process	C	ΔC (stats.)	ΔC (sys.)	ΔC (theo.)
EWK $Z Z j j$	0.663	± 0.002	$\pm^{0.032}_{0.031}$	NA
QCD $q \bar{q} \rightarrow Z Z$	0.702	± 0.003	$\pm^{0.061}_{0.051}$	$\pm^{0.015}_{0.018}$
QCD $gg \rightarrow Z Z$	0.741	± 0.021	$\pm^{0.143}_{0.072}$	± 0.002

Table 5.10 C Factor of different $Z Z j j$ processes.

Then the C from different processes are combined together to be used as inputs for cross section calculation:

$$C = \sum_i \frac{N_{\text{FV}}^i}{\sum_j N_{\text{FV}}^j} \times C_i = 0.699 \pm 0.003(\text{stats.}) \pm^{0.011}_{0.013} (\text{theo.}) \pm 0.028(\text{exp.}) \quad (5.5)$$

The stats. refers to the statistical uncertainty from MC simulation statistics. The theo. and exp. denote the theoretical and experimental uncertainties described in section 5.5.

5.6.2 Result of fiducial cross section

The cross section in fiducial volume is computed as:

$$\sigma^{FV.} = \frac{N_{data} - N_{bkg}}{C \times Lumi} \quad (5.6)$$

where N_{data} and N_{bkg} denote the number of events selected from detector-level selection from data and sum of backgrounds, and C is the C-factor calculated above, Lumi represents the integrated luminosity of data 2015–2018 of 139 fb^{-1} .

As shown in table 5.3, in inclusive measurement, only "Others" represents background, processes of EW- $ZZjj$, QCD- $q\bar{q} \rightarrow ZZ$ and QCD- $gg \rightarrow ZZ$ are signals. Table 5.11 shows the fiducial cross section for $\ell\ell\ell\ell$ channel measured from equation 5.6, as well as the predicted cross section measured from signals MC directly. The measured

Measured fiducial σ [fb]	Predicted fiducial σ [fb]
$1.27 \pm 0.12(\text{stat}) \pm 0.02(\text{theo}) \pm 0.07(\text{exp}) \pm 0.01(\text{bkg}) \pm 0.03(\text{lumi})$	$1.14 \pm 0.04(\text{stat}) \pm 0.20(\text{theo})$

Table 5.11 Measured and predicted fiducial cross-sections in $\ell\ell\ell\ell jj$ final-state. Uncertainties due to different sources are presented.

cross section has a total uncertainty of 11%, and is found to be compatible with SM prediction. The data statistic is still dominant for the measurement.

5.7 Search for EW- $ZZjj$

Figure 5.11 represents the m_{jj} distribution in SR (left) and QCD CR (right), where the normalization of EW and QCD processes are scaled according to their observed value explained later in this section. High m_{jj} region is more sensitive for EW- $ZZjj$ events detection from this figure. Figure 5.12 shows the spectrum of invariant mass of $\ell\ell\ell\ell$ system (m_{ZZ}) in SR.

5.7.1 MD discriminant

To further separate the EW- $ZZjj$ component from QCD- $ZZjj$, a MD based on *Gradient Boosted Decision Tree (BDTG)* algorithm^[90] is trained with simulated events via TMVA framework^[62]. For $\ell\ell\ell\ell$ channel, training is performed between EW (signal) and QCD (background) processes. Twelve event kinematic variables sensitive to the charac-

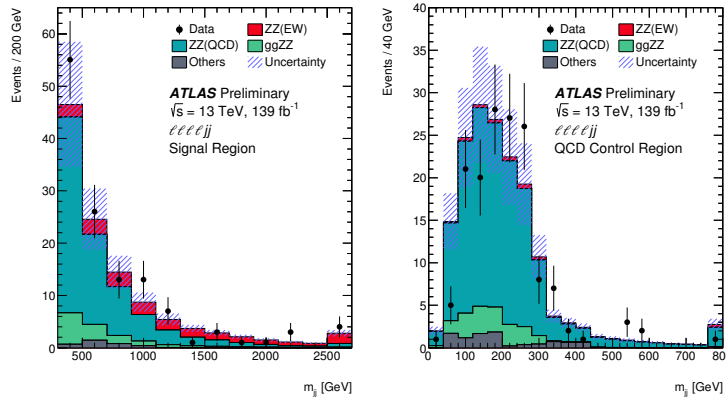


Fig. 5.11 Observed and expected m_{jj} distributions in SR (left) and QCD CR (right). The error bands include the expected experimental and theoretical uncertainties. The error bars on the data points show the statistical uncertainty on data. The contributions from the QCD and EW production of ZZ_{jj} events are scaled by 0.96 and 1.35, respectively, which correspond to the observed normalization factors in the statistical fit to the combined channel. The last bin includes the overflow events.

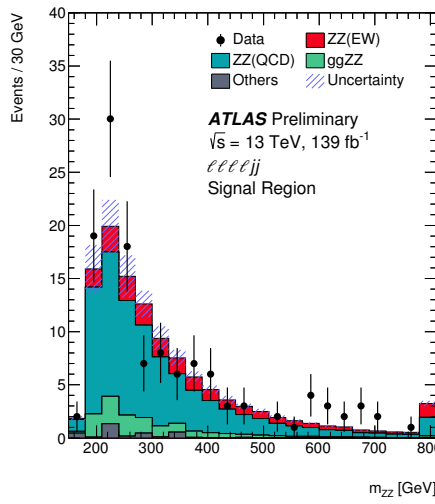


Fig. 5.12 Observed and expected m_{ZZ} spectrum in SR. The error bands include the expected experimental and theoretical uncertainties. The error bars on the data points show the statistical uncertainty on data. The contributions from the QCD and EW production of ZZ_{jj} events are scaled by 0.96 and 1.35, respectively, which correspond to the observed normalization factors in the statistical fit to the combined channel. The last bin includes the overflow events.

teristics of the EW signal is used as input features in training. Table 5.12 listed those input variables with the order of their ranking provide by TMVA tool. The jet-related information provides larger sensitive in $\ell\ell\ell\ell$ final-state. Then the MD distributions in both SR

Rank	Variables	Description
1	m_{jj}	Dijet invariant mass
2	p_T^{j1}	p_T of the leading jet
3	p_T^{j2}	p_T of the sub-leading jet
4	$\frac{p_T(ZZjj)}{H_T(ZZjj)}$	p_T of the $ZZjj$ system divided by the scalar p_T sum of Z bosons and two jets
5	$y_{j1} \times y_{j2}$	Product of jet rapidities
6	Δy_{jj}	Rapidity difference between two jets
7	Y_{Z2}^*	Rapidity of the second Z boson
8	Y_{Z1}^*	Rapidity of the Z boson reconstructed from the lepton pair with the mass closer to the Z boson mass
9	p_T^{ZZ}	p_T of 4l system
10	m_{ZZ}	Invariant mass of 4l system
11	p_T^{Z1}	p_T of the Z boson reconstructed from the lepton pair with the mass closer to the Z boson mass
12	$p_T^{\ell3}$	p_T of the third lepton

Table 5.12 Input features for the training of MD.

and QCD CR region are used for statistical fit.

5.7.2 Profile likelihood ratio method

To examine the compatibility between data and the signal-plus-background hypothesis, a test statistic is driven by using the profile likelihood ratio method. The binned

likelihood function is given as”

$$\mathcal{L}(\mu, \sigma) = \prod_i^{\text{bins}} \mathcal{L}_{\text{poiss}}(N_{\text{data}} | \mu s(\theta) + b(\theta))_i \times \mathcal{L}_{\text{gauss}}(\theta)_i \quad (5.7)$$

where the Poisson term presents the statistical fluctuations of the data and a Gaussian term models the pdf of auxiliary measurement to constrain the systematics. μ denotes the signal strength of EW- $Z Z jj$ process, computed as the ratio between measured (expected) cross section to the SM prediction. θ presents the nuisance parameter, which is the set of parameters that parameterize the effect of systematic uncertainties described in section 5.5. N_{data} is the number of selected data events, while the $s(\theta)$ is the expected signal yield and $b(\theta)$ is the expected background yield as the function of nuisance parameters.

The test statistic q_μ is defined as:

$$q_\mu = -2 \ln \left(\frac{\mathcal{L}(\mu, \hat{\theta}_\mu)}{\mathcal{L}(\hat{\mu}, \hat{\theta})} \right) \quad (5.8)$$

in which $\mathcal{L}(\hat{\mu}, \hat{\theta})$ is the unconditional likelihood with respect to both μ and θ , and $\mathcal{L}(\mu, \hat{\theta}_\mu)$ is the conditional likelihood for a constant μ . Signal-like data distributions are more likely to have a low test-statistic (q_μ close to 0) while the contributions of background-like data have a larger q_μ . Under the background-only hypothesis, the compatibility of the observed (Asimov) data with the prediction is calculated to obtain the observed (expected) significance respectively.

5.7.3 Fitting procedure

A profile likelihood fit is performed on MD discriminant to extract the EW- $Z Z jj$ signal from backgrounds. The binning of MD distributions in SR is optimized to maximize the sensitive for detecting EW signal. The normalization of QCD- $Z Z jj$ production (μ_{QCD}^{III}) in $\ell\ell\ell\ell$ channel is varied simultaneously in the fit in SR and QCD CR as described in section 5.4. The signal strength of EW- $Z Z jj$ production (μ_{EW}) is taken as parameter of interest and floated in the fit. The effects of the uncertainties related to normalizations and shapes described previously in section 5.5 of background processes in the MD distribution are all taken into account.

In most case, a common nuisance parameter is used for each source of systematic in all bins and all channels. The statistical uncertainties for simulated samples are uncorrelated among all bins, and the background uncertainties only applied to their corresponding backgrounds. For combination between two channels, the theoretical uncertainties be-

tween $\ell\ell\ell\ell$ and $\ell\ell\nu\nu$ are uncorrelated due to different fiducial volumes definition. Furthermore, to be more conservative, the generator modelling uncertainty for QCD- $ZZjj$ production mentioned in section 5.5 is separated to be two nuisance parameters in low and high MD region.

5.7.4 Result of statistical fit

The statistical fit is performed both in individual $\ell\ell\ell\ell$ channel, as well as the combination between $\ell\ell\ell\ell$ and $\ell\ell\nu\nu$ channel to gain more statistic. The results of statistical fit for $\ell\ell\ell\ell$ channel and the combined channel are presented in table 5.13. The $\ell\ell\nu\nu$ analysis will not be talked about in this thesis, but more details can refer to^[91]. To drive expected results, the observed data is used for QCD CR to extract normalization factor of QCD component (μ_{QCD}^{III}), while in SR, asimov data built from background prediction and signal model with SM assumed cross section is used. For $\ell\ell\ell\ell$ channel, the background-

	μ_{EW}	$\mu_{QCD}^{\ell\ell\ell\ell jj}$	Significance Obs. (Exp.)
$\ell\ell\ell\ell jj$	1.54 ± 0.42	0.95 ± 0.22	$5.48 (3.90) \sigma$
Combined	1.35 ± 0.34	0.96 ± 0.22	$5.52 (4.30) \sigma$

Table 5.13 Observed μ_{EW} and $\mu_{QCD}^{\ell\ell\ell\ell jj}$, as well as the observed and expected significance from the individual $\ell\ell\ell\ell jj$ channel, and the combined fits. The full set of systematic uncertainties is included.

only hypothesis is rejected at 5.5σ (3.9σ) for data (expectation), which leads to the observation of EW- $ZZjj$ production. Figure 5.13 shows the post-fit MD distributions for $\ell\ell\ell\ell$ channel in SR (left) and QCD CR (right). The EW- $ZZjj$ cross section measured in $\ell\ell\ell\ell$ channel is extracted to be 0.94 ± 0.26 fb.

Figure 5.14 depicts the display of an event candidate of EW- $ZZjj$ production in $2e2\mu$ final state with two jets in forward and backward region, and with a MD value from 0.875 to 1.0.

5.8 Prospect study of EW- $ZZjj$ production in HL-LHC

5.8.1 Introduction

The High-Luminosity Large Hadron Collider (HL-LHC) project aims to increase luminosity by a factor of 10 beyond the LHC’s design value to increase the potential for discoveries after 2025. The designed luminosity will reach 3000 fb^{-1} with the centre-of-mass energy of 14 TeV.

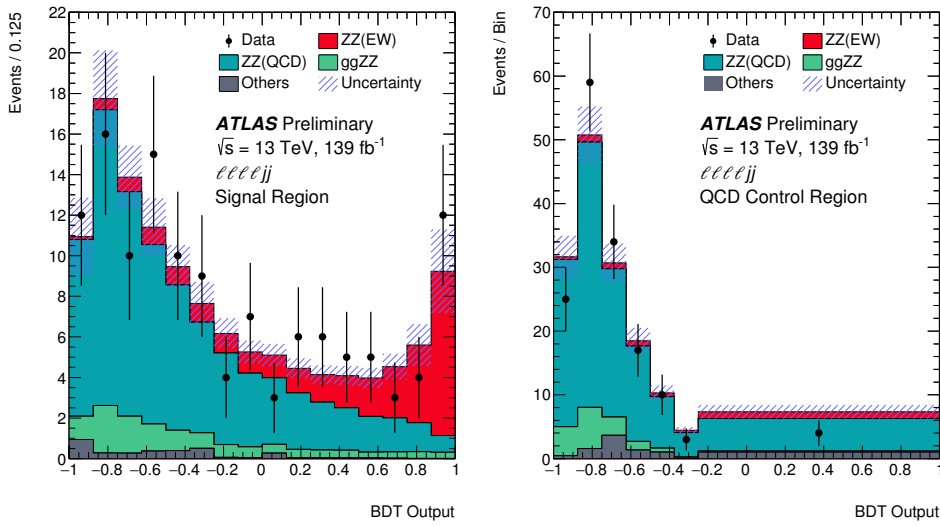


Fig. 5.13 Observed and expected multivariate discriminant distributions after the statistical fit in the $\ell\ell\ell\ell$ SR (left) and QCD CR (right). The error bands include the experimental and theoretical uncertainties, as well as the uncertainties in μ_{EW} and $\mu_{\text{QCD}}^{\ell\ell\ell\ell jj}$. The error bars on the data points show the statistical uncertainty on data.

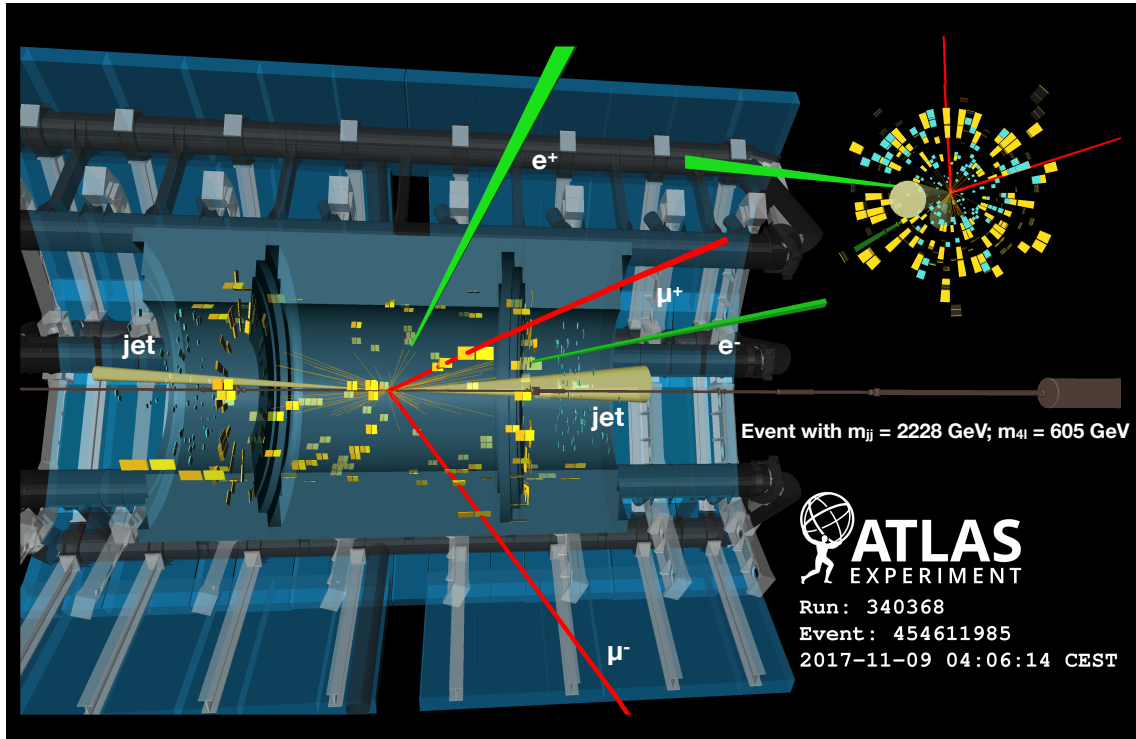


Fig. 5.14 Display of an event candidate of EW- $ZZjj$ production in $2e2\mu$ channel in last MD bin ($0.875 < \text{MD} < 1.0$). The invariant mass of the di-jet (four-lepton) system is 2228 (605) GeV.

As introduced in previous sections, with full run-2 data of 139 fb^{-1} collected by ATLAS detector at the LHC, the EW- $ZZjj$ production is the last channel of observation for VBS processes with massive boson due to its very low cross section in ZZ decay. So we expect that this channel will benefit significantly from the increased luminosity at the high-luminosity LHC (HL-LHC), and can be studied in great details for this known mechanism.

In this section, a prospect study has been performed for EW- $ZZjj$ production at the HL-LHC in the $\ell\ell\ell\ell$ channel with the ATLAS detector. The study uses 3000 fb^{-1} of simulated pp collisions at a centre-of-mass energy of 14 TeV that is expected to be recorded by the ATLAS detector at HL-LHC. All simulated events are produced at particle-level, and the detector effects of lepton and jet reconstruction and identification are estimated by corrections, assuming the mean number of interactions per bunch crossing ($< \mu >$) of 200.

5.8.2 The ATLAS detector at HL-LHC

As the expectation of HL-LHC, the new Inner Tracker (ITk)^[92] will extend the tracking acceptance capability of ATLAS detector to pseudorapidity ($|\eta|$) up to 4.0. By including a forward muon trigger, the upgraded Muon Spectrometer^[93] is also expected to provide muon identification capabilities to $|\eta|$ up to 4.0. In addition, the new high granularity timing detector (HGTD)^[94] that designed to mitigate the pile-up (PU) effects is also expected to be installed in the forward region of $2.4 < |\eta| < 4.0$. More details of expected performance of the upgraded ATLAS detector at the HL-LHC has been reported in Ref.^[95].

5.8.3 Simulation

The analysis is performed using particle-level events. The samples are generated at $\sqrt{s} = 14 \text{ TeV}$ and with a fast simulation based on setting for ATLAS detector at the HL-LHC. The signal in this analysis is EW- $ZZjj$ process, while only the dominant irreducible background of QCD- $ZZjj$ is considered. Both signal and background are generated using Sherpa with the NNPDF3.0NNLO PDF set. The signal sample is modelled with two jets at Matrix Element (ME) level. The background only considers the qq-initial process, in which events with up to one (three) outgoing partons are generated at NLO (LO) in perturbative QCD. As a quick study, other minor backgrounds such as fake backgrounds from $Z+jets$ and top-quark processes, as well as Diboson without 4l final-state and Triboson processes are not considered into this analysis. Furthermore, for hard scat-

tering events, the pile-up collisions are set with a mean value of 200 interactions per bunch crossing. In studies, signal and background yields are then scaled to an integrated luminosity of 3000 fb^{-1} for HL-LHC.

5.8.4 Event selection

The analysis selection follows closely to the one in ATLAS run-2 analysis as described in section 5.3. Here are some changes according to the expectation of HL-LHC scenario for ATLAS detector:

- Extend the lepton identification in forward with $|\eta| < 4.0$
- Pile-up (PU) jet suppression is applied with a PU rejection factor of 50 for all PU jets in the region of $|\eta| < 3.8$, based on the expected ATLAS detector performance at the HL-LHC.
- The jets are required to have $p_T > 30$ (70) GeV in the $|\eta| < 3.8$ ($3.8 < |\eta| < 4.5$) region.
- For two selected jets, tight the m_{jj} requirement to > 600 GeV, and require $\Delta\eta_{jj} > 2$.

In addition, a fiducial volume, which is used to study the expected precision of the cross-section measurements, is defined at particle-level with the same kinematic requirements listed above.

Table 5.14 summarized the number of selected signal and background events normalized to 3000 fb^{-1} . In addition to the *baseline* selection listed above, to compare the different detector scenarios at the HL-LHC, two alternative selections are also studied:

- Reduce the lepton η region to 2.7, to understand the effect due to forward lepton reconstruction and identification with the upgraded ATLAS detector.
- Only apply the PU jet suppression with region $|\eta| < 2.4$, to measure the improvement of *baseline* by extending the rejection range of PU jets at the HL-LHC.

Selection	$N_{\text{EW-ZZjj}}$	$N_{\text{QCD-ZZjj}}$	$N_{\text{EW-ZZjj}} / \sqrt{N_{\text{QCD-ZZjj}}}$
Baseline	432 ± 21	1402 ± 37	11.54 ± 0.58
Leptons with $ \eta < 2.7$	373 ± 19	1058 ± 33	11.46 ± 0.62
PU jet suppression only in $ \eta < 2.4$	536 ± 23	15470 ± 120	4.31 ± 0.19

Table 5.14 Comparison of event yields for signal ($N_{\text{EW-ZZjj}}$) and background ($N_{\text{QCD-ZZjj}}$) processes, and expected significance of EW- $ZZjj$ processes, normalized to 3000 fb^{-1} data at 14 TeV, with baseline and alternative selections. Uncertainties in the table refer to expected data statistical uncertainty at 14 TeV with 3000 fb^{-1} .

From this table, one can see the extended track coverage increases the $\ell\ell\ell\ell jj$ events by 15–30%, via improving the lepton efficiency. But the significance of searching for

EW- $ZZjj$ process does not improve so much due to the large increment of background events.

Figure 5.15 shows the kinematic distributions of di-jet invariant mass (m_{jj}), the ZZ invariant mass (m_{ZZ}) and the ϕ separation of two Z bosons ($|\Delta\phi(ZZ)|$) as well as the centrality of the ZZ system. The ZZ centrality is defined as:

$$ZZ \text{ centrality} = \frac{|y_{ZZ} - (y_{j1} + y_{j2})/2|}{|y_{j1} - y_{j2}|} \quad (5.9)$$

To measure the event yield, the top panel shows the stack distribution for EW- and QCD- $ZZjj$ processes, while bottom panel is the ratio between EW and QCD.

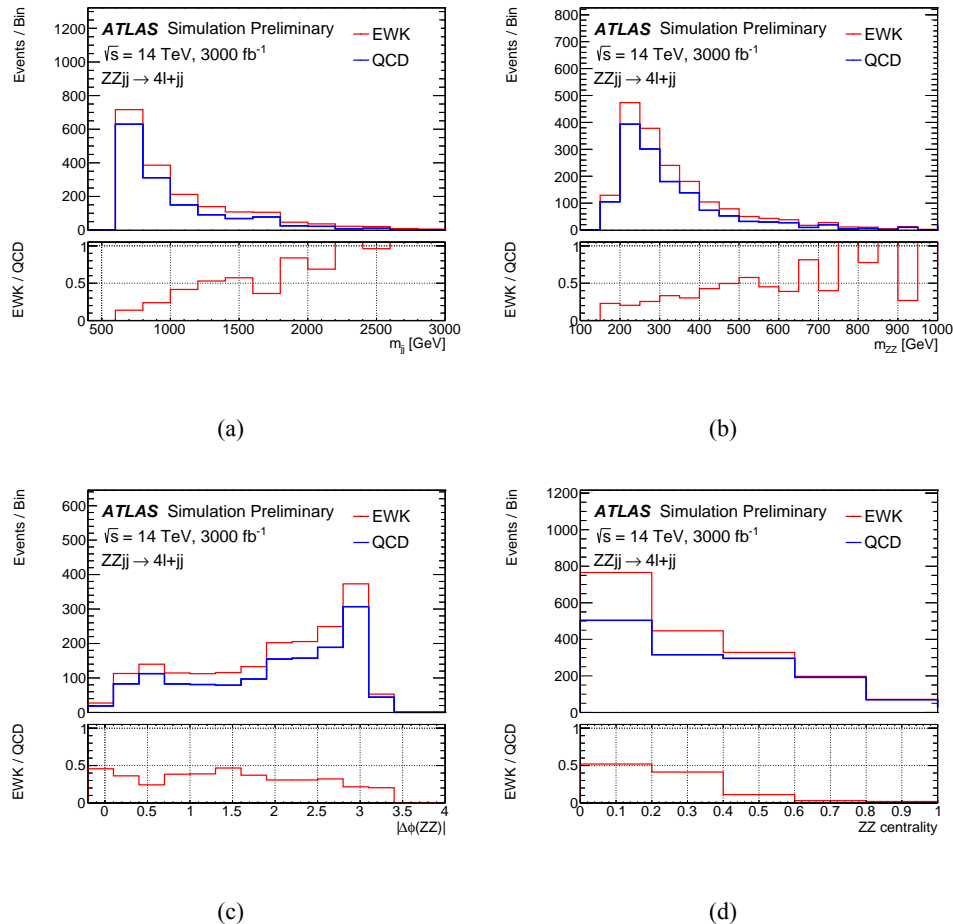


Fig. 5.15 Detector-level distributions of EW- and QCD- $ZZjj$ processes with selected events in defined phase space at 14 TeV of (a) m_{jj} , (b) m_{ZZ} , (c) $|\Delta\phi(ZZ)|$, (d) ZZ centrality, normalized to 3000 fb^{-1} .

5.8.5 Systematics

According to studies in section 5.5, the dominant systematic in $\ell\ell\ell\ell$ channel is from theoretical systematic for QCD- $ZZjj$ background process. Different sizes of systemat-

ics have been studied, at a factor of 5, 10 and 30% on background modelling. The 5% uncertainty is an optimal estimation when there is enough data events from QCD-enrich control region at the HL-LHC can be used to constrain the theoretical normalization on QCD- $Z Z jj$ process. The 30% one is a conservative estimation, in which the uncertainties are directly calculated from different PDF sets and QCD renormalization and factorization scales, following recommendation from the PDF4LHC mentioned in section 5.5.

For experimental sources, the jet systematic has been checked following the setting provided by the HL-LHC in Ref. [95], and the uncertainties are within 5% level, which is smaller than run-2 measurement at 10%. Figure 5.16 depicts the up and down variations for jet uncertainty provided by the HL-LHC performance tool as function of di-jet invariant mass. Therefore, a conservative 5% uncertainty is used as experimental uncertainty.

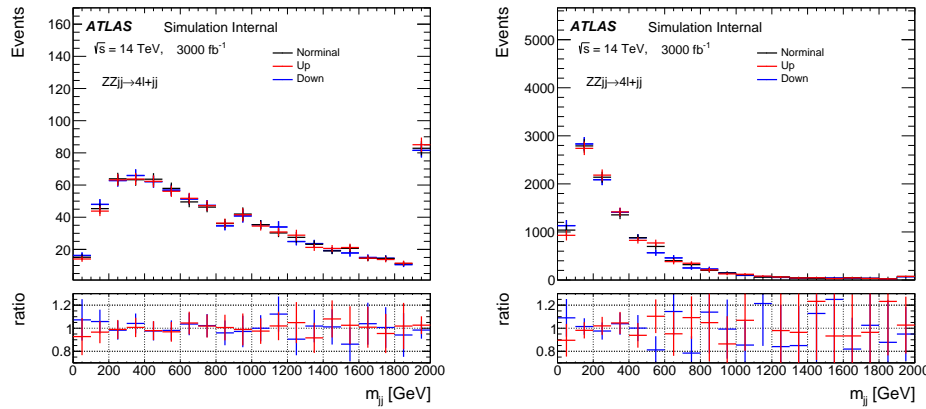


Fig. 5.16 Jet variations on m_{jj} distribution for EW- $Z Z jj$ (left) and QCD- $Z Z jj$ (right) processes with luminosity of 3000 fb^{-1} at 14 TeV. *Upgrade Performance Function* is used to extract the uncertainties with *baseline* setting.

Since the final results rely greatly on the uncertainties, especially the theoretical uncertainties on QCD- $Z Z jj$ production. So results with different uncertainty conditions will be shown as below:

- The case with statistical uncertainty of simulated samples only.
- The case with statistical and experimental uncertainties (5%)
- The case with statistical, experimental and additional theoretical uncertainties at 5%, 10% and 30% respectively.

Three different sources of uncertainties are treated as uncorrelated and summed up quadratically.

5.8.6 Results

In this analysis, instead of a statistical fit, the expected significance of EW- $ZZjj$ production is calculated as:

$$\text{Significance} = \frac{S}{\sqrt{\sigma(B)_{\text{stat.}}^2 + \sigma(B)_{\text{syst.}}^2}}, \quad (5.10)$$

where S presents the number of selected signal events, and $\sigma(B)_{\text{stat.}}$ and $\sigma(B)_{\text{syst.}}$ denote the statistical and systematic (exp. + theo.) uncertainties from background processes. The statistical uncertainty is computed from expected data yield with an integrated luminosity of 3000 fb^{-1} .

Base on baseline selection of $m_{jj} > 600 \text{ GeV}$, a additional scan over different m_{jj} cuts are performed with a step of 50 GeV for luminosity of 3000 fb^{-1} under different systematic conditions, as shown in figure 5.17.

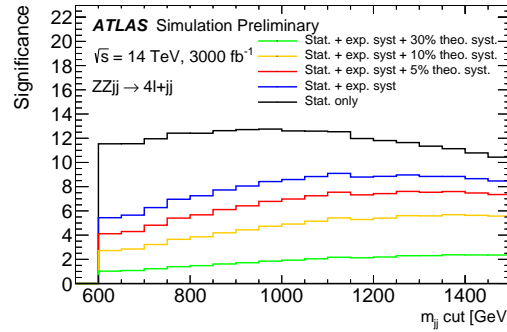


Fig. 5.17 The expected significance of EW- $ZZjj$ processes as a function of different m_{jj} cut with 3000 fb^{-1} , under conditions of different sizes of theoretical uncertainties on the QCD- $ZZjj$ background modelling. The statistical uncertainty is estimated from expected data yield at 14 TeV with 3000 fb^{-1} . Different uncertainties are summed up quadratically.

In addition, the expected differential cross section of EW- $ZZjj$ process is measured in the defined phase space at 14 TeV , as a function of m_{ZZ} and m_{jj} , shown in figure 5.18. The expected differential cross sections are calculated as:

$$\sigma = \frac{N_{\text{pseudo-data}} - N_{QCD-ZZjj}}{L * C_{EW-ZZjj}} \quad (5.11)$$

$$C_{EW-ZZjj} = \frac{N_{EW-ZZjj}^{\text{det.}}}{N_{EW-ZZjj}^{\text{part.}}}$$

where $N_{\text{pseudo-data}}$ denotes the expected number of data events with 3000 fb^{-1} luminosity at 14 TeV , and $N_{QCD-ZZjj}$ and $N_{EW-ZZjj}$ are the number of predicted events of QCD-

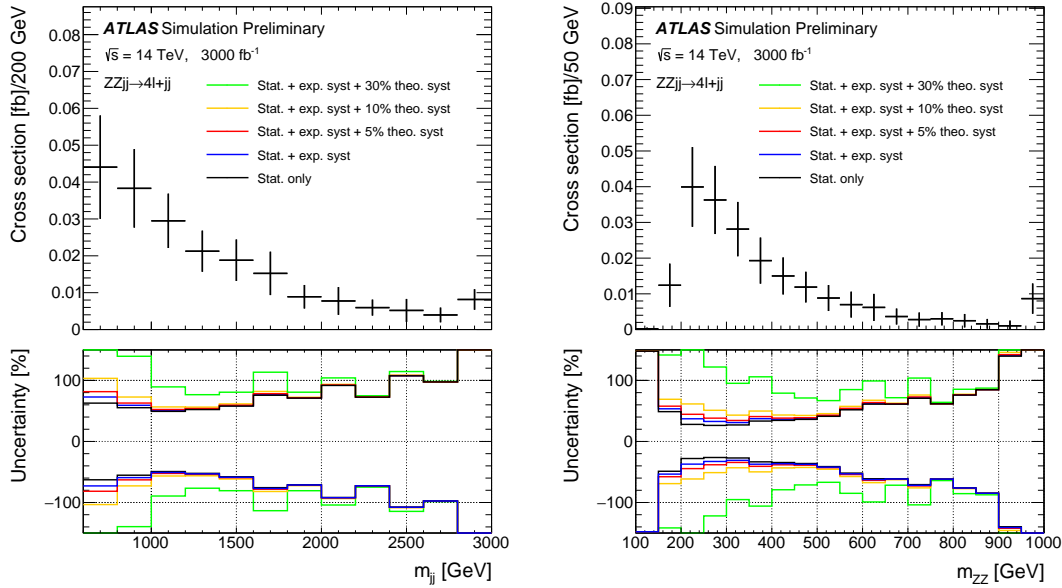


Fig. 5.18 The projected differential cross-sections at 14 TeV for the EW- $ZZjj$ processes as a function of m_{jj} (left) and m_{ZZ} (right). The top panel shows measurement with statistical only case, where statistical uncertainty is estimated from expected data yield at 14 TeV with 3000 fb^{-1} . The bottom panel shows impact of different sizes of systematic uncertainties.

$ZZjj$ and EW- $ZZjj$ processes in particle-level. The $C_{EW-ZZjj}$ factor represents the detector efficiency for EW- $ZZjj$ processes introduced in section 5.6.1. The interference between EW- and QCD- $ZZjj$ processes is ignored due to its minor contribution.

The number of expected integrated cross section as well as its uncertainty under different uncertainty conditions are shown in table 5.15 in 3000 fb^{-1} luminosity at 14 TeV. The statistical uncertainty is at 10% level when with such large luminosity. The result is dominated by systematics and can reach 100% level when theoretical modelling uncertainty is 30% for QCD- $ZZjj$ processes.

	Cross section [fb]	Stat. only	Plus exp.	Plus 5% theo.	Plus 10% theo.	Plus 30% theo.
EW- $ZZjj$	0.21	± 0.02	± 0.04	± 0.05	± 0.08	± 0.21

Table 5.15 Summary of expected cross-section measured with different theoretical uncertainties. The statistical uncertainty is computed from expected data yield with 3000 fb^{-1} at 14 TeV. Different uncertainties are treated as uncorrelated and quadratic sum is used.

5.9 Conclusion

The fiducial cross section for inclusive $ZZjj$ production is measured in this section, with a total relative uncertainty of 11% for the $\ell\ell\ell\ell jj$ final state, and found to be compatible with the SM prediction. The observation of electroweak production of two jets in association with a Z -boson pair decay to $\ell\ell\ell\ell$ final state using 139 fb^{-1} of 13 TeV pp collision data collected by ATLAS experiment at the LHC is presented in this section. The search for electroweak production of two jets in association with a Z -boson pair is based on multivariate discriminants (MD) to enhance the separation between the signal and backgrounds. In $\ell\ell\ell\ell$ final state, the background-only hypothesis is rejected with an observed (expected) significance of 5.5 (3.9) σ , which gives the first observation of electroweak production in $ZZjj$ channel.

In addition, the prospect study for the EW- $ZZjj$ production at the HL-LHC in the $\ell\ell\ell\ell$ channel, using 3000 fb^{-1} simulated pp collision at a centre-of-mass energy of 14 TeV has been presented. The precision of the expected measurements of the integrated and differential cross sections as a function of di-jet or $\ell\ell\ell\ell$ invariant mass are shown. Under the assumption of theoretical uncertainty for the QCD- $ZZjj$ processes and experimental uncertainty for jets being constraint at 5% level respectively, with statistical uncertainty in 3000 fb^{-1} being considered, the observation of the EW- $ZZjj$ process can reach a significance of 7σ .

Chapter 6 Search for heavy ZZ resonances in the $\ell\ell\ell\ell$ final state using pp collisions data collected by ATLAS detector from 2015–2018

6.1 Introduction

A new particle was discovered by the ATLAS and CMS Collaborations at the LHC^[64–65] in 2012. Both two experiments have confirmed that the properties including spin, couplings and parity of this new particle are consistent with Higgs boson predicted in the Standard Model (SM), which is an important milestone in understanding of the mechanism of EWSB. Nevertheless, the possibility that this newly discovered particle is just a part of the extended Higgs sector as predicted by various extensions in the SM cannot be ruled out. There are many models predicting the existence of new heavy resonances decaying into dibosons, such as a heavy spin-0 neutral Higgs boson^[96] and the two-Higgs-doublet models (2HDM)^[97], as well as the spin-2 Kaluza–Klein (KK) excitations of the graviton (G_{KK})^[98].

Though with smaller branching ratio comparing to semileptonic or fully hadronic decay channels, the $\ell\ell\ell\ell$ final states have its unique sensitivity in mass range smaller than 1 TeV region due to its good mass resolution and relative small experimental and theoretical systematics. This section presents the search for heavy resonance decaying into a pair of Z bosons to the $\ell\ell\ell\ell$ final states, in which ℓ denotes to either an electron or a muon. Several signal hypotheses are considered. The first hypothesis is a heavy Higgs boson (spin-0 resonance) under the narrow-width approximation (NWA). Then since several theoretical models prefer non-negligible natural widths, the models under large-width approximation (LWA), assuming widths of 1%, 5% and 10% of the resonance mass, are also studied. It is assumed that the heavy resonance is produced predominantly via the gluon-gluon fusion (ggF) and the vector-boson fusion (VBF), but with the unknown ratio of two production rates. So the results are separated for ggF and VBF production modes. To gain more sensitivity, the $\ell\ell\ell\ell$ events are classified into ggF- and VBF-enriched categories. Moreover, for the NWA model, the categorizations are studied under both cut-based and DNN-based methods, whose details of categorization are shown in following sections.

The search uses the four-lepton invariant mass in the range of 200 GeV to 2000 GeV for signal hypothesis of spin-0 resonance under the NWA model, and from 400 GeV to 1500 GeV for the one under the LWA models. The data collected by ATLAS detector

at the LHC from 2015 to 2018 at the centre-of-mass energy of 13 TeV is used. In case of no excess, upper limits on the production rate of different signal hypotheses are computed from statistical fits to m_{4l} distribution in the ggF production of a heavy scalar under both NWA and LWA models, and in the VBF production only under NWA model.

6.2 Data and MC samples

6.2.1 Data samples

The data used in these searches are collected by ATLAS detector at the centre-of-mass energy of 13 TeV during the years of 2015 to 2018. Only events pass the latest Good Run List (GRL) released by the Data Quality group from ATLAS experiment as listed in section 5.2.1 corresponding to an integrated luminosity of $139.0 \pm 2.4 \text{ fb}^{-1}$ are used. Table 6.1 listed the recorded integrated luminosity, average and peak pile up of each year’s data.

Table 6.1 Summary of the recorded integrated luminosity (lumi), average and peak pile up (PU) of data from 2015 to 2018.

Year	recorded integrated lumi	lumi after GRL	average PU	peak PU
2015	3.86 fb^{-1}		13.4	28.1
2016	35.6 fb^{-1}	36.2 fb^{-1}	25.1	52.2
2017	46.9 fb^{-1}	44.3 fb^{-1}	37.8	79.8
2018	60.6 fb^{-1}	58.5 fb^{-1}	36.1	88.6

6.2.2 Background MC simulations

Background processes considered in this analysis include ZZ ($q\bar{q} \rightarrow ZZ$, $gg \rightarrow ZZ$), triboson (WWZ , WZZ , ZZZ), $Z+jets$ and top-quark ($t\bar{t}$, $t\bar{t}V$) processes. The QCD $q\bar{q} \rightarrow ZZ$ process is modelled using Sherpa 2.2.2^[76] with the NNPDF3.0NNLO^[77] PDF, in which events with up to one (three) outgoing partons are generated at NLO (LO) in pQCD. The production of ZZ from the gluon-gluon initial state with a four-fermion loop or with an exchange of the Higgs boson, which has an order of α_S^4 in QCD, is not included in the Sherpa simulation. So a separate gg induced ZZ sample including the continuum background, the SM Higgs boson, and the interference contribution is modelled using Sherpa 2.2.2 with the NNPDF3.0NNLO PDF set, and with an additional 1.7 k-factor^[78] being applied. The EW- $ZZjj$ production is simulated using Sherpa 2.2.2 with the NNPDF3.0NNLO PDF, and the $ZZZ \rightarrow \ell\ell\ell\ell qq$ process is also taken into account in this sample.

The $Z+jets$ events are generated using Sherpa 2.2.2 with the NNPDF3.0NNLO PDF, in which the ME is calculated for up to two partons with next-to-leading-order (NLO) accuracy in pQCD and up to four partons with LO accuracy. The $Z+jets$ events are normalized using the next-to-next-to-leading-order (NNLO) cross section. The triboson processes with full leptonic decays and at least four prompt charged leptons are generated using Sherpa 2.1.1. For top-quark pair ($t\bar{t}$) production and the single top-quark productions in t -channel, s -channel and Wt -channel, the Powheg-Box v2 is used with the CT10 PDF. The productions of $t\bar{t}$ in association with Z boson(s) ($t\bar{t}Z$) is modelled with MadGraph5_aMC@NLO.

6.2.3 Signal MC simulations

One model considered in this analysis is heavy spin-0 resonance under Narrow Width Approximation (NWA) simulated using Powheg-Box v2 MC event generator with the CT10 PDF. The gluon-gluon fusion (ggF) production mode and vector-boson fusion (VBF) production mode are calculated separately with matrix elements up to NLO in QCD. The Powheg-Box is interfaced to Pythia8 for parton showering, and for decaying the Higgs boson into the $H \rightarrow ZZ \rightarrow \ell\ell\ell\ell$ final states. Events under NWA are generated at mass points between 200 GeV to 2000 GeV using the step of 100 (200) GeV up to (above) 1 TeV in both ggF and VBF productions.

In addition, heavy Higgs boson events under Large Width Approximation (LWA) with widths of 1%, 5%, 10% and 15% of the boson mass are generated using MadGraph5_aMC@NLO 2.3.2 interfaced to Pythia8. Only ggF production is considered. Mass points between 400 GeV to 2000 GeV are simulated with 100 (200) GeV step up to (above) 1 TeV. To describe jet multiplicity, MadGraph5_aMC@NLO is used to simulated process of $pp \rightarrow H + \geq 2$ jets at NLO in QCD with the FxFx merging scheme^[99].

Spin-2 Kaluza–Klein (KK) gravitons (G_{KK}) from the Bulk Randall–Sundrum model^[100] are also studies in this analysis. Events are generated by MadGraph5_aMC@NLO at LO in QCD, which is then interfaced to Pythia8. The G_{KK} -gluon coupling $k/\overline{M}_{\text{Planck}}$, where k is the curvature scale of the extra dimension and $\overline{M}_{\text{Planck}}$ is the reduced Planck mass, is set to 1. And the mass of the G_{KK} is the only free parameter in this simplified model.

6.3 Analysis selections

6.3.1 Objects selection

Similar as described in section 5.3, the selection of this analysis relies on the definition of multiple objects: *electrons*, *Muons*, and *jets*. Details of definitions for each objects are described as below:

Electron: The reconstruction of electrons is described in section 4.2.3. In this analysis, the electron candidates satisfying *Loose* working point (WP) are selected, with a selection efficiency ranging from 90% for transverse momentum $p_T = 20$ GeV to 96% for $p_T > 60$ GeV. Also, electrons are required to have $p_T > 7$ GeV and $|\eta| < 2.47$.

Muon: To increase the acceptance range in reco-level for $\ell\ell\ell\ell jj$ channel, all four types of muons (CB, ST, CT, ME muons, described in section 4.2.4) are used. But at most one CT, ST or ME muon is allowed in one $\ell\ell\ell\ell$ quadruplet. The Muon candidates are required to pass $p_T > 5$ GeV and $|\eta| < 2.7$, and satisfy the *Loose* identification criterion with an efficiency of 98.5%.

Jets: Jets are clustered using the anti- k_t algorithm with radius parameter $R = 0.4$ implemented in the FastJet package described in section 4.2.5. The particle flow (PFlow) objects^[101], which are the ensemble of positive energy topo-clusters surviving the energy subtraction step at the PFlow algorithm within $|\eta| < 2.5$, and the selected tracks that are matched to a primary vertex, are used as inputs to the FastJet package. Before jet-finding, the topo-cluster η and ϕ are recomputed pointing to the primary vertex position, instead of the centre of detector. For the region of $|\eta| > 2.5$ that outside the geometrical acceptance of the tracker, only the calorimeter information is available. Therefore, the topo-clusters, formed from calorimeter cells with significant energy depositions, are used as inputs to jet reconstruction. The jets used in this analysis are required to pass $p_T > 30$ GeV and $|\eta| < 4.5$. To further reduce the effects of pile-up jets, a jet vertex tagger (JVT) is applied to jets with $p_T < 60$ GeV and $|\eta| < 2.4$.

Overlap removal: As the selected jet and lepton candidates can be reconstructed from same detector information, an overlap-removal procedure is applied. For electron and muon sharing the same ID track, the electron is selected in the case that the muon is calorimeter-tagged and does not have a MS track, or is a segment-tagged muon, otherwise the muon is selected. The jet overlapping with electron (muon) within a cone of size of $\Delta R \equiv \sqrt{(\Delta\eta)^2 + (\Delta\phi)^2} = 0.2(0.1)$ are removed.

6.3.2 Event selection

First of all, the four-lepton events are required to pass single or multi-lepton triggers, with the multi-lepton ones including electron(s)-muon(s) triggers. Due to the increasing of peak luminosity and pile-up, the p_T and E_T thresholds of triggers increase slightly during the data-taking periods from 2015 to 2018. Table 6.2 summarizes the triggers used for $\ell\ell\ell\ell jj$ channel. The overall trigger efficiency for selected signal events passing final selection is around 98%.

Table 6.2 Summary of the p_T (E_T) trigger thresholds (in GeV) employed for the muon (electron) trigger selection in the year of 2015, 2016, 2017, and 2018.

Trigger item	Trigger threshold			
	2015	2016	2017	2018
single muon	$\mu 20; \mu 50; \mu 60$	$\mu 24; \mu 26; \mu 40; \mu 50$	$\mu 26; \mu 50; \mu 60$	$\mu 26; \mu 50; \mu 60$
single electron	$e 24; e 60; e 120$	$e 26; e 60; e 140; e 300$	$e 26; e 60; e 140; e 300$	$e 26; e 60; e 140; e 300$
dimuon	$2\mu 10; \mu 18_{-\mu} 8$	$2\mu 10; 2\mu 14; \mu 22_{-\mu} 8$	$2\mu 14; \mu 22_{-\mu} 8$	$2\mu 14; \mu 22_{-\mu} 8$
dielectron	$2e 12$	$2e 15; 2e 17$	$2e 17; 2e 24$	$2e 17; 2e 24$
electron-muon	$e 24_{-\mu} 8$	$e 24_{-\mu} 8; e 26_{-\mu} 8$ $e 17_{-\mu} 14; e 7_{-\mu} 24; 2e 12_{-\mu} 10; e 12_{-\mu} 10$	$e 26_{-\mu} 8$	$e 26_{-\mu} 8$
trimuon	$\mu 18_{-\mu} 2\mu 4$	$\mu 11_{-\mu} 2\mu 4; \mu 6_{-\mu} 2\mu 4; \mu 20_{-\mu} 2\mu 4; 3\mu 4$ $3\mu 6$	$4\mu 4; \mu 20_{-\mu} 2\mu 4; 3\mu 4$	$\mu 20_{-\mu} 2\mu 4$
trilepton	$e 17_{-\mu} 2e 9$	$e 17_{-\mu} 2e 9; e 17_{-\mu} 2e 10$	$e 24_{-\mu} 2e 12$	$e 24_{-\mu} 2e 12$

The $\ell\ell\ell\ell$ quadruplets are formed by two opposite-sign, same-flavour (OSSF) lepton pairs (l^+l^-), selected as described in section 6.3.1. The p_T threshold of first three leading muons are required to be 20, 15 and 10 GeV. If there are more than one combination of lepton pairing in quadruplet, the pairing is selected by keeping it with the lepton pairs closest (leading pair, refers as m_{12}) and second closest (sub-leading pair, refers as m_{34}) to Z boson mass. The mass of leading pair is required to satisfy $50 < m_{12} < 106$ GeV, while the sub-leading pair is required to be less than 115 GeV and larger than a threshold that is 12 GeV for $m_{4\ell} \leq 140$ GeV, rises linearly from 12 GeV to 50 GeV with $m_{4\ell}$ in the interval of [140 GeV, 190 GeV] and is fixed to 50 GeV for $m_{4\ell} > 190$ GeV.

The two lepton pairs in quadruplet are required to have angular separation with $\Delta R > 0.1$. To suppress the contribution from $J/\psi \rightarrow ll$ decays, for 4μ and $4e$ quadruplets, the event is rejected if any opposite-sign same-flavour lepton pair is found with mass below 5 GeV. If there are more than one quadruplets from different channels in event at the point, the quadruplet with highest expected signal rate is selected in the order of 4μ , $2e2\mu$, $4e$. The transverse impact-parameter significance ($|d_0|/\sigma_{d_0}$) for muons (electrons) is then required to be smaller than 3 (5) to suppress the backgrounds from heavy-flavour hadrons.

In addition, the track- (p_T) and calorimeter-based isolation criteria is required for all electrons and muons to further suppress the reducible backgrounds of $Z+jets$ and $t\bar{t}$. For lepton isolation selection, the two track- and calorimeter-based variables, $E_T^{topocone}$ and $p_T^{varcone}$ as described in section 4.2.4 (section 4.2.3) for muons (electrons), are vulnerable to pileup. For track-based variable, this is because of additional tracks in the event. The definition of $p_T^{varcone}$ attempts to limit the tracks used in the calculation to those from the vertex via a loose cut of $|z_0 \sin(\theta)| < 3$, which proved to be too loose in new pile-up regime 2017 and 2018 datasets. So new track-based variable is used, by adding a requirement that the track be used in determining the vertex, or that, if not, it both pass the cut on $|z_0 \sin(\theta)|$ and not be used in determining any other vertex, which makes the track-based variable to be more isolation-robust in the high pile-up regime. The new variable is named as $ptvarcone[cone]_TightTTVA_{pt}[p_T \text{ cut}]$, where [cone] is the cone size and [p_T cut] is the cutoff for including tracks in the calculation.

For calorimeter-based variable, the calculation of $E_T^{topocone}$ corrects the pile-up effects by subtracting an average pileup contribution computed over the whole detector. But with the increasing of energy density of pile-up events, the root mean square (RMS) of $E_T^{topocone}$ variable increases, which leads to the increment of possibility that the pile-up fluctuations are not be accounted for correctly. One possible solution is using particle-flow (PFlow) method to calculate the calorimeter isolation. As part of PFlow reconstruction process, it assigns the clusters to tracks which improves the track-cluster association for better determination of the raw value of the E_T in the cone. And using PFlow jets to calculate the pileup correction provides a further improvement. So a resulting variable named $neflow-isol[cone]$ is used. Finally, a requirement of isolation, called *FixedCutPFlowLoose*, which gives better performance in high pileup condition is applied to electrons and muons:

$$(\max(ptcone20_TightTTVA_{pt}500, ptvarcone30_TightTTVA_{pt}500) + 0.4 \times neflow-isol20) / p_T < 0.16$$

On the top of impact parameter cut and lepton isolation cut, the four-lepton candidates are also required to originate from a common vertex to reduce $Z+jets$ and $t\bar{t}$ backgrounds. This is ensured by applying a vertex fit χ^2 cut of 4 ID tracks of lepton candidates satisfying $\chi^2/N_{dof} < 6$ (9) for events in 4μ ($4e$ and $2e2\mu$) channel(s).

To improve the mass resolution, the QED process of final state radiation (FSR) photons in Z boson decays are taken into account in the reconstruction of Z bosons. The Four-momentum of any reconstructed photon that is consistent with having been radiated from lepton(s) in leading pair are added into final state. Moreover, the four-momenta of leptons in both (leading and sub-leading) pairs are recomputed by performing a Z -mass-

constrained kinematic fit, which uses a Breit–Wigner Z boson line-shape and Gaussian function with width set to the expected lepton resolution per lepton to model the momentum response function. The Z-mass-constrained mass improves the $m_{4\ell}$ resolution by up to 15% depending on m_H .

In summary, table 6.3 lists a comprehensive object and event level selection as described above. Table 6.4 shows the cutflow of NWA ggF signal samples at several different mass points as examples.

6.3.3 Event categorizations

To improve the sensitivity of search in both VBF and ggF production mode in NWA model, events are classified into the VBF- and ggF- enriched categories. With the increment of statistic with full run-2 data, a deep neural network (DNN-) based classifier has been studied, while in the meantime the traditional cut-based classifier is also used as cross check.

1. Cut-based categorization

There are four categories in total: one VBF-enriched category and three ggF-enriched ones with different lepton-flavor channels. The categorization is defined based on kinematic cuts:

- VBF-enriched category: Events have at least two selected jets as defined in section 6.3.1, with the two leading jets being separated by $|\Delta\eta_{jj}| > 3.3$ and invariant mass satisfying $m_{jj} > 400$ GeV;
- ggF-enriched categories: The remaining events that are not classified into VBF-enriched category. Then events are categorized into three channels based on lepton-flavor, namely ggF_2e2μ, ggF_4e and ggF_4μ.

2. DNN-based categorization

In order to target different production modes, two types of classifiers, one dedicated to VBF production while the other one for ggF, have been trained. Details of two classifiers are described as below.

DNN models

Figure 6.1 shows the architecture of VBF (left) and ggF (right) network. The VBF network includes three parts: two recurrent networks (RNNs) and one multilayer perceptron (MLP). One RNN (and another one) takes the p_T and \square of p_T -ordered four leptons (two leading jets) as input features, which intends to study the time relationship from particle decay between leptons (jets). The ggF network consists of one RNN and one MLP.

For training, the VBF and ggF signal samples at the masses of 200, 300, 400, 500,

Table 6.3 Summary of the object and event selection requirements.

Physics Objects	
Electrons	
Loose Likelihood quality electrons with hit in innermost layer, $E_T > 7$ GeV and $ \eta < 2.47$	
Interaction point constraint: $ z_0 \cdot \sin \theta < 0.5$ mm (if ID track is available)	
Muons	
Loose identification with $p_T > 5$ GeV and $ \eta < 2.7$	
Calo-tagged muons with $p_T > 15$ GeV and $ \eta < 0.1$, segment-tagged muons with $ \eta < 0.1$	
Stand-alone and silicon-associated forward restricted to the $2.5 < \eta < 2.7$ region	
Combined, stand-alone (with ID hits if available) and segment-tagged muons with $p_T > 5$ GeV	
Interaction point constraint: $ d_0 < 1$ mm and $ z_0 \cdot \sin \theta < 0.5$ mm (if ID track is available)	
Jets	
anti- k_T jets with <i>bad-lose</i> identification, $p_T > 30$ GeV and $ \eta < 4.5$	
Overlap removal	
Jets within $\Delta R < 0.2$ of an electron or $\Delta R < 0.1$ of a muon are removed	
Vertex	
At least one collision vertex with at least two associated track	
Primary vertex	
Vertex with the largest p_T^2 sum	
Event Selection	
Quadruplet Selection	<ul style="list-style-type: none"> - Require at least one quadruplet of leptons consisting of two pairs of same-flavour opposite-charge leptons fulfilling the following requirements: - p_T thresholds for three leading leptons in the quadruplet: 20, 15 and 10 GeV - Maximum one calo-tagged or stand-alone muon or silicon-associated forward per quadruplet - Leading di-lepton mass requirement: $50 < m_{12} < 106$ GeV - Sub-leading di-lepton mass requirement: $m_{\text{threshold}} < m_{34} < 115$ GeV - $\Delta R(\ell, \ell') > 0.10$ for all leptons in the quadruplet - Remove quadruplet if alternative same-flavour opposite-charge di-lepton gives $m_{\ell\ell} < 5$ GeV - Keep all quadruplets passing the above selection
Isolation	<ul style="list-style-type: none"> - Contribution from the other leptons of the quadruplet is subtracted - FixedCutPFlowLoose WP for all leptons
Impact Parameter	<ul style="list-style-type: none"> - Apply impact parameter significance cut to all leptons of the quadruplet
Significance	<ul style="list-style-type: none"> - For electrons: $d_0/\sigma_{d_0} < 5$ - For muons: $d_0/\sigma_{d_0} < 3$
Best Quadruplet Selection	<ul style="list-style-type: none"> - If more than one quadruplet has been selected, choose the quadruplet with highest Higgs decay ME according to channel: 4μ, $2e2\mu$, $2\mu2e$ and $4e$
Vertex Selection	<ul style="list-style-type: none"> - Require a common vertex for the leptons: - $\chi^2/\text{ndof} < 5$ for 4μ and < 9 for others decay channels

Table 6.4 Cutflow table for NWA ggF signal samples at different mass points. N_{event} represents the number of MC events selected after each cut is applied. The proportion of events selected relative to the initial number of events is also included.

Cut	$m_H = 400 \text{ GeV}$		$m_H = 600 \text{ GeV}$		$m_H = 1000 \text{ GeV}$		$m_H = 2000 \text{ GeV}$	
	N_{event}	Rel. [%]	N_{event}	Rel. [%]	N_{event}	Rel. [%]	N_{event}	Rel. [%]
Initial	150 000	100.00	150 000	100.00	149 000	100.00	120 000	100.00
Lepton selection	47 422	31.61	52 345	34.90	56 932	38.21	48 644	40.54
SFOS	44 086	29.39	48 247	32.16	51 701	34.70	43 228	36.02
Kinematic cuts	44 024	29.35	48 215	32.14	51 677	34.68	43 197	36.00
Z_1 Mass	43 857	29.24	47 975	31.98	51 368	34.48	42 749	35.62
Z_2 Mass	39 359	26.24	42 834	28.56	45 602	30.61	37 479	31.23
J/ψ Veto	39 354	26.24	42 828	28.55	45 597	30.60	37 477	31.23
ΔR	39 346	26.23	42 823	28.55	45 588	30.60	37 473	31.23
Isolation	37 088	24.73	40 753	27.17	43 615	29.27	35 971	29.98
Impact parameters	36 461	24.31	40 186	26.79	43 066	28.90	35 610	29.68
Vertex requirement	36 372	24.25	40 100	26.73	42 967	28.84	35 529	29.61
Trigger	36 333	24.22	40 076	26.72	42 952	28.83	35 503	29.59
“Badjet” veto	36 202	24.13	39 908	26.61	42 779	28.71	35 350	29.46

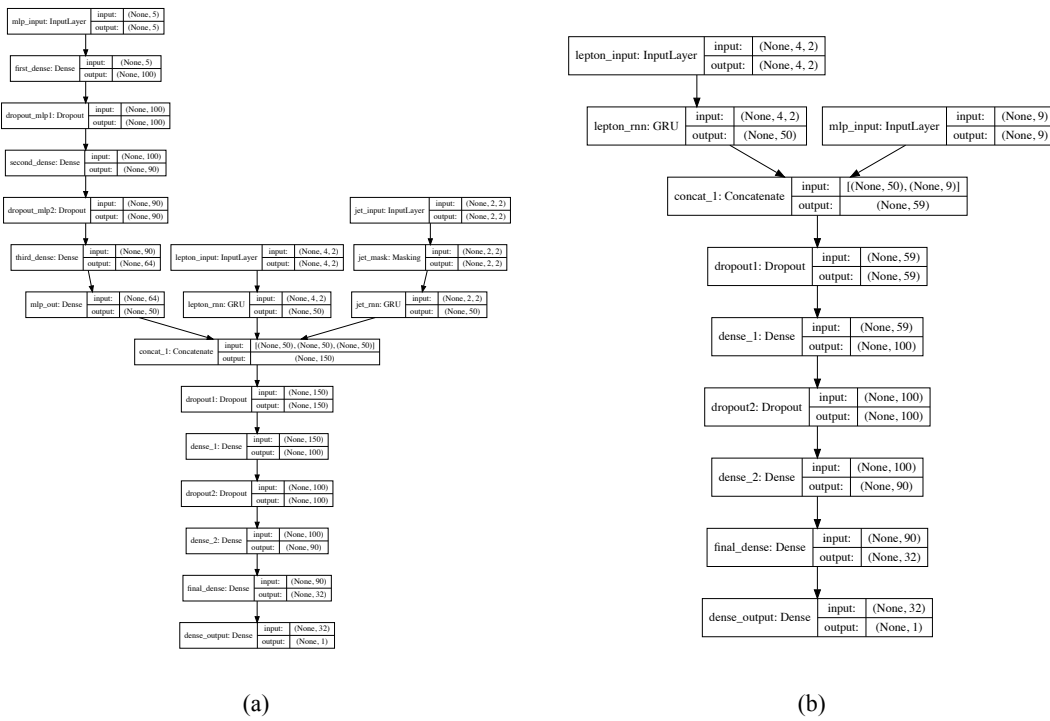


Fig. 6.1 (a) VBF DNN architecture diagram. (b) ggF DNN architecture.

600, 700, 800, 900, 1000, 1200, 1400 GeV are used with positive label. The VBF (ggF) signals are only used for VBF (ggF) classifier. The background (with negative labels) uses simulated samples of QCD and EW $q\bar{q} \rightarrow ZZ$ processes as well as $gg \rightarrow ZZ$ process summed according to their cross section. In addition to the selections described in section 6.3.2, the events used for VBF network are required to have $N_{\text{jets}} \geq 2$, while $N_{\text{jets}} < 2$ is required to events for ggF network.

In order to assign equivalent importance to signals and background, during the training, signal events are reweighted to follow the $m_{4\ell}$ distribution from background, as shown in figure 6.2 (figure 6.3) before (left) and after (right) reweighting for VBF (ggF) samples.

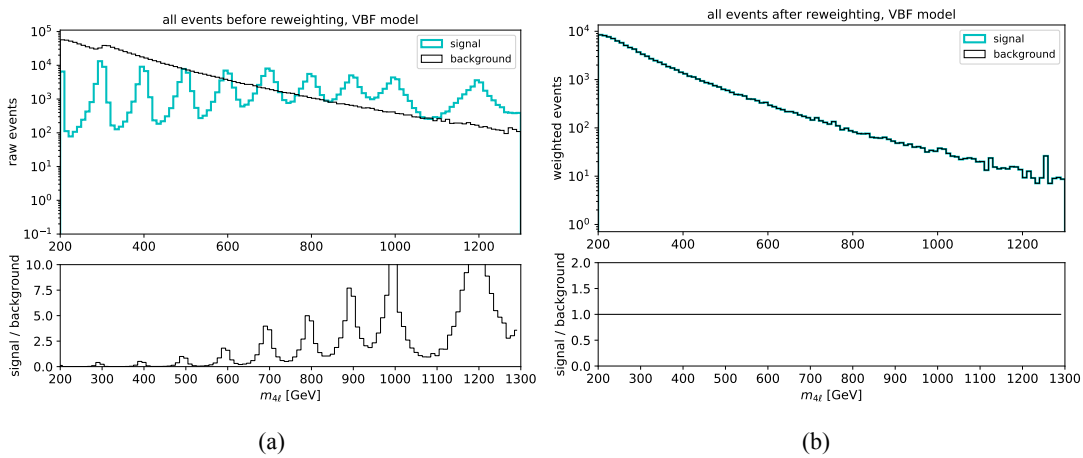


Fig. 6.2 (a) $m_{4\ell}$ distribution of raw (unweighted) training events for VBF signal (blue) and background (black); (b) $m_{4\ell}$ distribution of weighted VBF signal (blue) and background (black) used at training time.

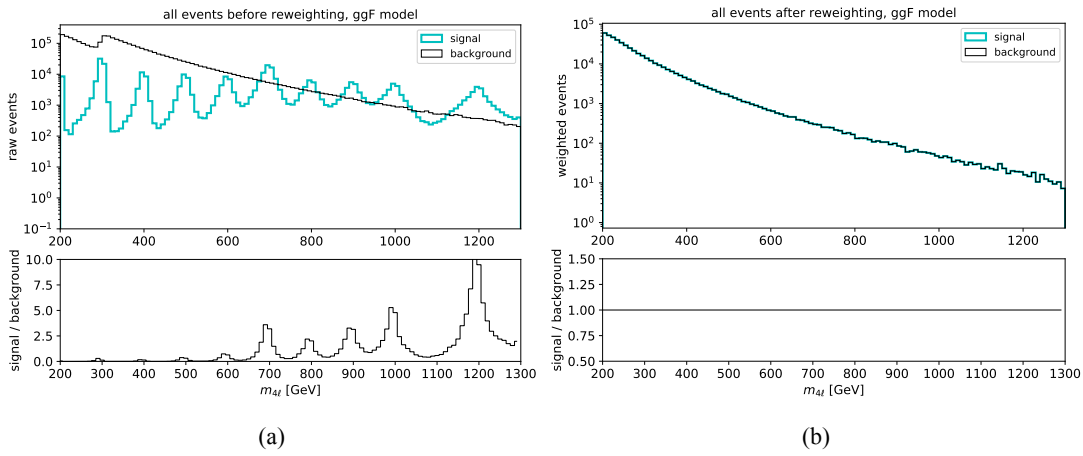


Fig. 6.3 (a) $m_{4\ell}$ distribution of raw (unweighted) training events for ggF signal (blue) and background (black); (b) $m_{4\ell}$ distribution of weighted ggF signal (blue) and background (black) used at training time.

Input features

Table 6.5 (table 6.6) lists the input features used for VBF (ggF) network during the training. For VBF network, one RNN (the other one) takes the p_T and \square of p_T -ordered four leptons (two leading jets) as input features, which intends to study the time relationship from particle decay between leptons (jets). For ggF network, the only one RNN model takes as input features of the p_T and \square of p_T -ordered four leptons.

Table 6.5 Input features for the VBF network.

Variable	Description
$m_{4\ell}$	4ℓ invariant mass
m_{jj}	dijet invariant mass
p_T^{jj}	dijet transverse momentum
$\Delta\eta_{H,j}$	difference in pseudorapidities between the 4ℓ system and the leading jet
$\min \Delta R_{jZ}$	minimum angular separation between one of the two $\ell\ell$ pairs and a jet
p_T^j	transverse momenta of the two leading jets
η^j	pseudorapidities of the two leading jets
p_T^ℓ	transverse momenta of the four leptons
η^ℓ	pseudorapidities of the four leptons

Table 6.6 Input features for the ggF network.

Variable	Description
$m_{4\ell}$	4ℓ invariant mass
$\cos\theta_1$	decay angle of the leading Z
$\cos\theta_2$	decay angle of the sub-leading Z
$\cos\theta^*$	production angle of the ZZ system
ΔR_{jH}	angular separation between the 4ℓ system and the leading jet
ϕ	azimuthal angle of the ZZ system
$p_T^{4\ell}$	transverse momentum of the 4ℓ system
$\eta^{4\ell}$	pseudorapidity of the 4ℓ system
p_T^j	transverse momentum of up to one jet
η^j	pseudorapidity of up to one jet
p_T^ℓ	transverse momenta of the four leptons
η^ℓ	pseudorapidities of the four leptons

Evaluation of models

Figure 6.4 shows the classifier response output of background samples (QCD and EW $q\bar{q} \rightarrow ZZ$ and $gg \rightarrow ZZ$) as well as VBF (left) and ggF (right) signal sample at 700 GeV.

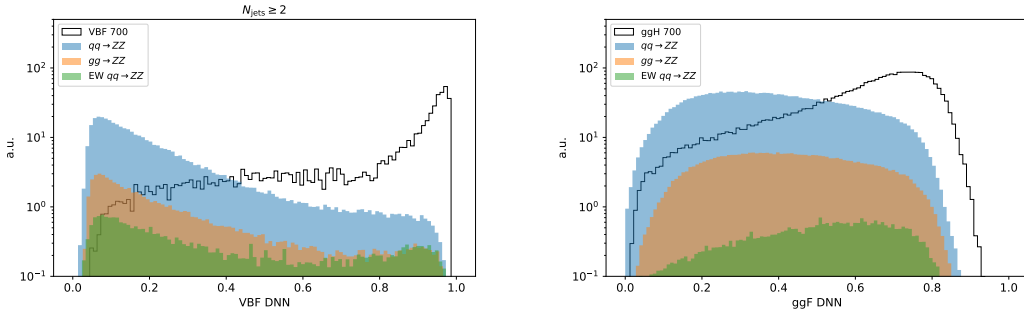


Fig. 6.4 VBF (left) and ggF (right) output of the background samples (filled) and the 700 GeV signal sample (black).

Then the optimal cut at DNN output score is chosen based on an overall good performance of classifier to have a large significance improvement while retaining a high signal efficiency. Figure 6.5 shows the significance improvements of DNN-based cuts when comparing with cut-based one at different VBF (left) and ggF (right) mass samples, where the significance is calculated as:

$$Z = \sqrt{2 \left(n \ln \left[\frac{nb + \sigma^2}{b^2 + n\sigma^2} \right] - \frac{b^2}{\sigma^2} \ln \left[1 + \frac{\sigma^2(n-b)}{b(b+\sigma^2)} \right] \right)} \quad (6.1)$$

Cut at 0.5 (0.8) for VBF (ggF) classifier is chosen as shown in solid lines.

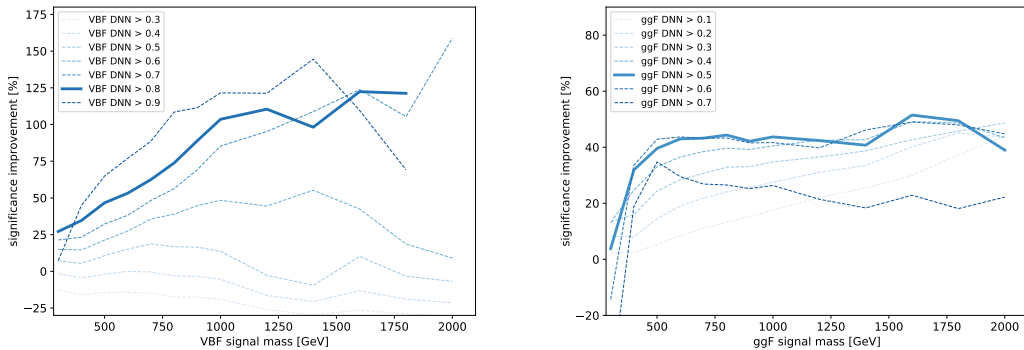


Fig. 6.5 Significance improvements of the DNN-based over the cut-based categorization of the VBF (ggF) category for VBF (ggF) signal samples between 300 and 2000 GeV for seven different cuts on the VBF (ggF) DNN score. The optimal cut of 0.8 (0.5) for VBF (ggF) DNN is chosen by a solid line, while other alternative cuts are plotted with dashed lines. For VBF category, results at 2000 GeV for cuts of 0.8 and 0.9 are missing due to a lack of background events passing this tight selection.

Then the events passing VBF classifier are categorized into VBF-enriched category.

Otherwise, the events failing VBF classifier but passing ggF classifier are categorized into ggF-enriched category, which is further split into 3 channels. All remaining events are sorted into one additional category called ‘rest’. Thus there are five categories defined in DNN-based categorization, named: VBF, ggF_2e2 μ , ggF_4e, ggF_4 μ and rest. In summary, cuts applied in categorization are defined as follow, and these phase spaces are also illustrated in figure 6.6.

- VBF-enriched category: Events have at least two selected jets ($N_{\text{jets}} \geq 2$), and with $DNN_{\text{VBF}} > 0.8$;
- ggF-enriched categories: $(N_{\text{jets}} \geq 2 \text{ \&\& } DNN_{\text{VBF}} \leq 0.8 \text{ \&\& } DNN_{\text{ggF}} > 0.5) \text{ || } (N_{\text{jets}} < 2 \text{ \&\& } DNN_{\text{ggF}} > 0.5)$;
- rest category: All remaining events that fail VBF and ggF cuts mentioned above.

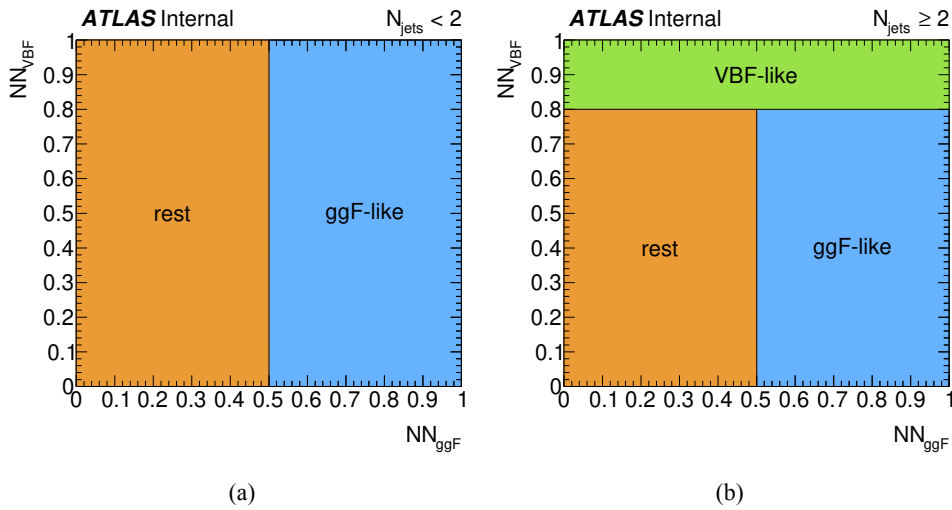


Fig. 6.6 Illustration of the DNN-based VBF and ggF event classification for events with (a) $N_{\text{jets}} < 2$ and (b) $N_{\text{jets}} \geq 2$.

6.3.4 Signal acceptance

The signal acceptance is defined as the ratio of events passing all analysis selection in each category to the total number of simulated events in whole phase space. In denominator, the events with τ final states are not taken into account. And the contribution of τ -lepton decay to electrons and muons final states is found to be negligible.

Figure 6.7 and 6.8 show the acceptance of NWA signal in DNN- and Cut- based categorization, estimated by merging the three signal MC campaigns, mc16a, mc16d and mc16e. A 3-rd order polynomial fit is applied for each category.

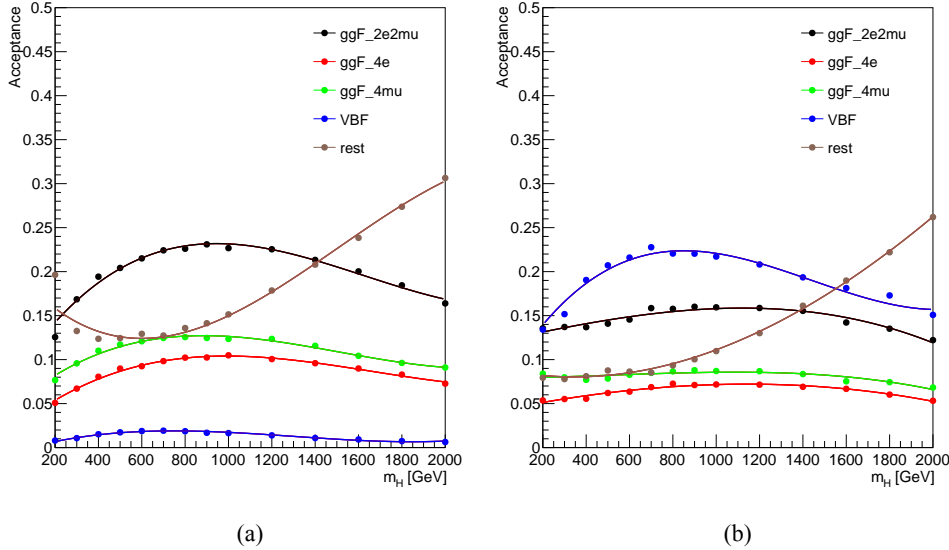


Fig. 6.7 NWA acceptance as a function of m_H for the DNN-based categorization for the samples of (a) ggF production mode; (b) VBF production mode.

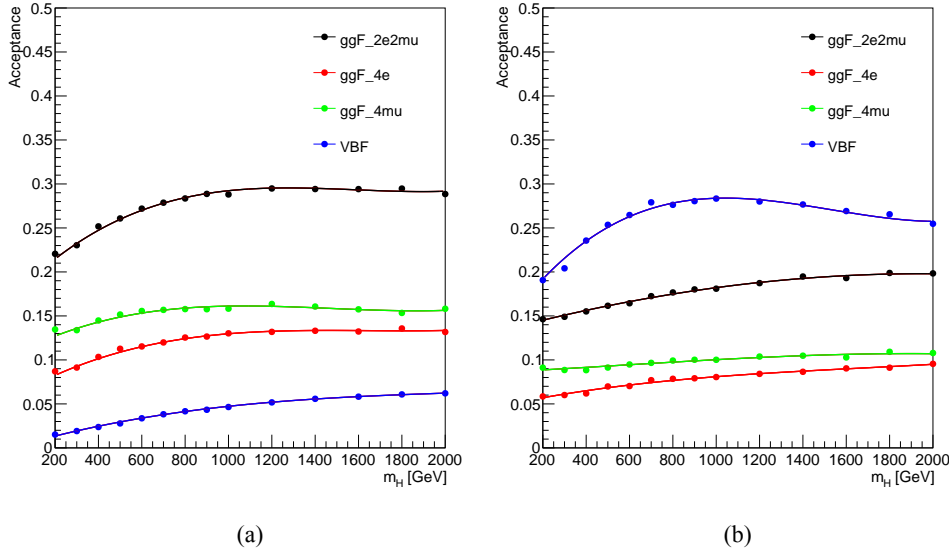


Fig. 6.8 NWA acceptance as a function of m_H for the Cut-based categorization for the samples of (a) ggF production mode; (b) VBF production mode.

6.4 Background estimation

In this analysis, 97% of total expected background events are from irreducible ZZ backgrounds, which includes about 86% quark-antiquark annihilation ($q\bar{q} \rightarrow ZZ$), 10% of gluon-initiated production ($gg \rightarrow ZZ$) and around 1% of EW vector boson scattering ($q\bar{q} \rightarrow ZZ$ EW) contribution. For $q\bar{q} \rightarrow ZZ$ EW, although it has small contribution in total background events after analysis selection, it's more important for VBF category

with about 16% contribution.

In addition to irreducible backgrounds, events from $Z+jets$ and $t\bar{t}$ processes, represent as reducible backgrounds, have contributions at a few percent level and can be measured using data driven method that will be described briefly later. Additional background called 'Others', which includes ttV and triple-V (VVV) processes, has tiny contribution and is estimated from MC simulation directly.

6.4.1 Irreducible backgrounds

The Irreducible backgrounds have events with four prompt lepton. The normalization of two dominant backgrounds $q\bar{q} \rightarrow ZZ$ and $gg \rightarrow ZZ$ are taken from data by the likelihood fit, and the normalization of small $q\bar{q} \rightarrow ZZ$ EW background is measured from MC simulation directly.

The $m_{4\ell}$ shapes of all three background components are token from MC samples and then parameterized by an empirical function for each of them in each category separately. Details of background modelling is introduced as below:

Background modelling of ZZ backgrounds

The empirical function used for background parameterization is:

$$f(m_{4\ell}) = C_0 H(m_0 - m_{4\ell}) f_1(m_{4\ell}) + H(m_{4\ell} - m_0) f_2(m_{4\ell}), \quad (6.2)$$

where,

$$\begin{aligned} f_1(x) &= \left(\frac{x - a_4}{a_3} \right)^{a_1-1} \left(1 + \frac{x - a_4}{a_3} \right)^{-a_1-a_2}, \\ f_2(x) &= \exp \left[b_0 \left(\frac{x - b_4}{b_3} \right)^{b_1-1} \left(1 + \frac{x - b_4}{b_3} \right)^{-b_1-b_2} \right], \\ C_0 &= \frac{f_2(m_0)}{f_1(m_0)}. \end{aligned}$$

The function consists of two parts, the first part f_1 describes the $m_{4\ell}$ spectrum in low mass region where both Z bosons decay on-shell, while the second one f_2 covers distribution at high mass tail. The transition between the low- and high- mass parts is presented in function 6.2 by the Heaviside step function $H(x)$ at the transition point m_0 . The m_0 is chosen to optimize the smoothness of the function, and practically $m_0 = 260$ (350) GeV is used for $q\bar{q} \rightarrow ZZ$ ($gg \rightarrow ZZ$ and $q\bar{q} \rightarrow ZZ$ EW). Besides, the continuity of two functions at m_0 is ensured by the factor C_0 applied to f_1 . The coefficients a_i in f_1 and b_i in f_2 are shape parameters obtained by fitting to $m_{4\ell}$ distribution from each MC simulated sample.

Figure 6.9 to 6.11 shows the fitting results of $q\bar{q} \rightarrow ZZ$, $gg \rightarrow ZZ$, $q\bar{q} \rightarrow ZZ$ EW backgrounds in 4 cut-based categories (ggF_2e2μ, ggF_4e, ggF_4μ and VBF). Figure 6.12 to 6.14 shows the fitting results of those backgrounds in 5 DNN-based categories (ggF_2e2μ, ggF_4e, ggF_4μ, VBF and rest).

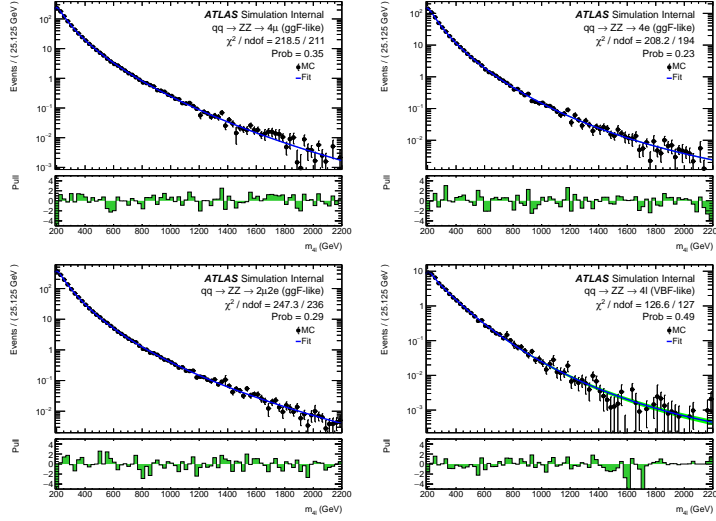


Fig. 6.9 Distributions of the $m_{4\ell}$ invariant mass fit projections of the $q\bar{q} \rightarrow ZZ$ background samples for the 4μ , $4e$ and $2\mu2e$ final states in the ggF category, and the 4ℓ inclusive VBF category. Cut-based categorization is used.

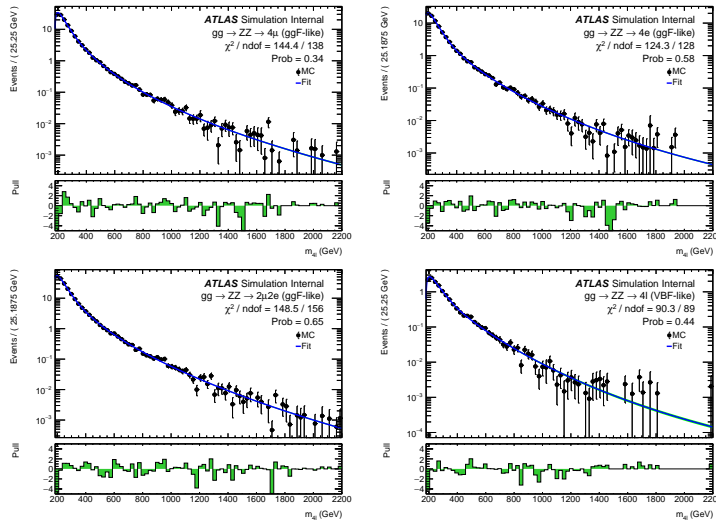


Fig. 6.10 Distributions of the $m_{4\ell}$ invariant mass fit projections of the $gg \rightarrow ZZ$ background samples for the 4μ , $4e$ and $2\mu2e$ final states in the ggF category, and the 4ℓ inclusive VBF category. Cut-based categorization is used.

6.4.2 Reducible backgrounds

Similar as 5.4, the reducible backgrounds include $Z+jets$ (consists of both heavy- and light-flavour jets), top quark pair, and WZ production, which contain fake and non-

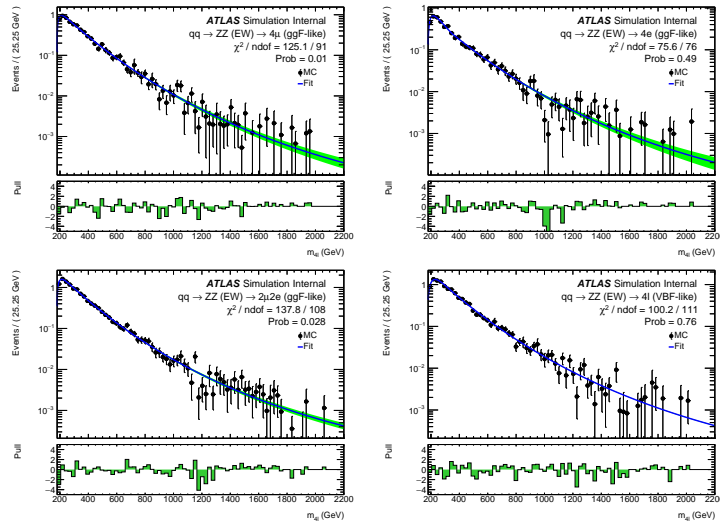


Fig. 6.11 Distributions of the $m_{4\ell}$ invariant mass fit projections of the $q\bar{q} \rightarrow ZZ$ (EW) background samples for the 4μ , $4e$ and $2\mu2e$ final states in the ggF category, and the 4ℓ inclusive VBF category. Cut-based categorization is used.

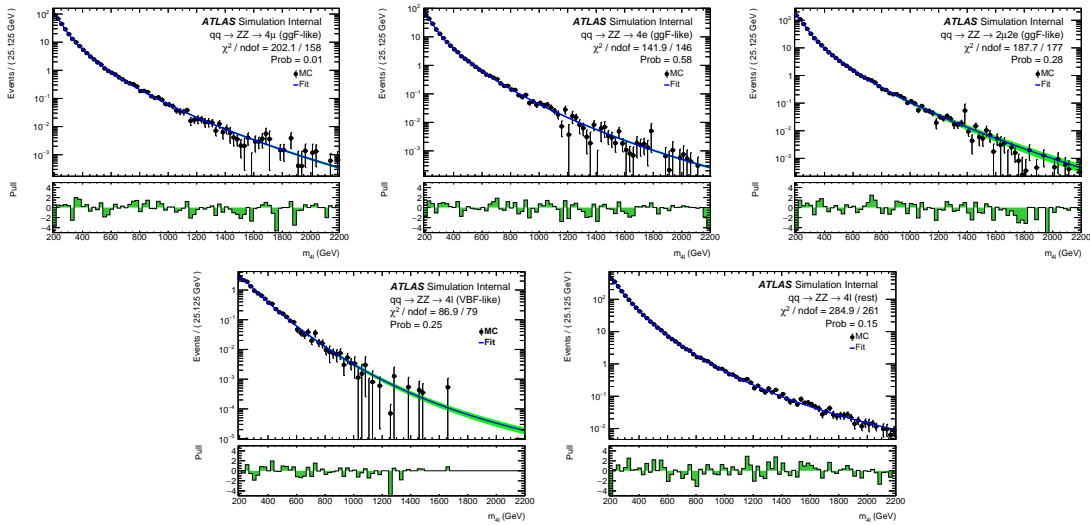


Fig. 6.12 Distributions of the $m_{4\ell}$ invariant mass fit projections of the $q\bar{q} \rightarrow ZZ$ background samples for the 4μ , $4e$ and $2\mu2e$ final states in the ggF category, the 4ℓ inclusive VBF category, and the “rest” category. DNN-based categorization is used.

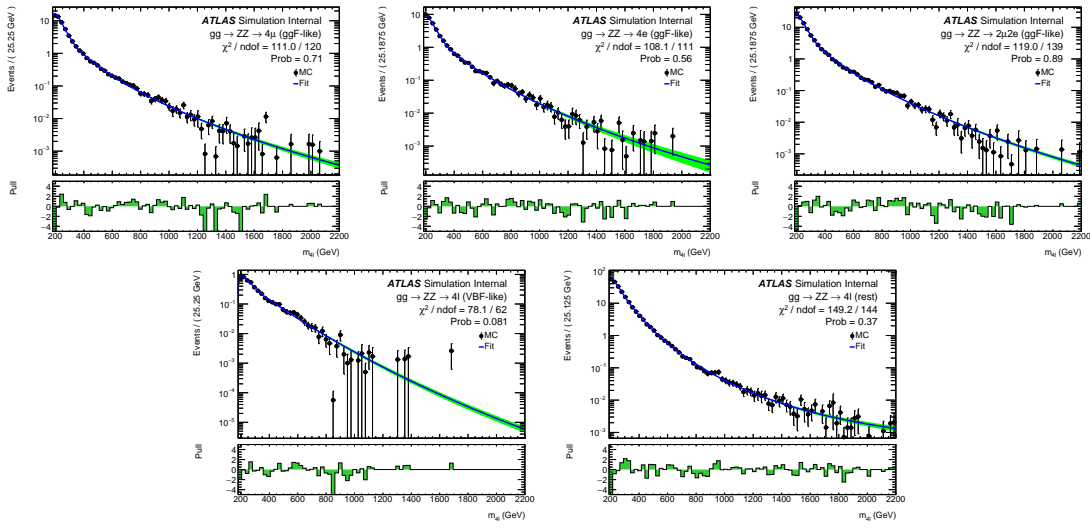


Fig. 6.13 Distributions of the $m_{4\ell}$ invariant mass fit projections of the $gg \rightarrow ZZ$ background samples for the 4μ , $4e$ and $2\mu2e$ final states in the ggF category, the 4ℓ inclusive VBF category, and the “rest” category. DNN-based categorization is used.

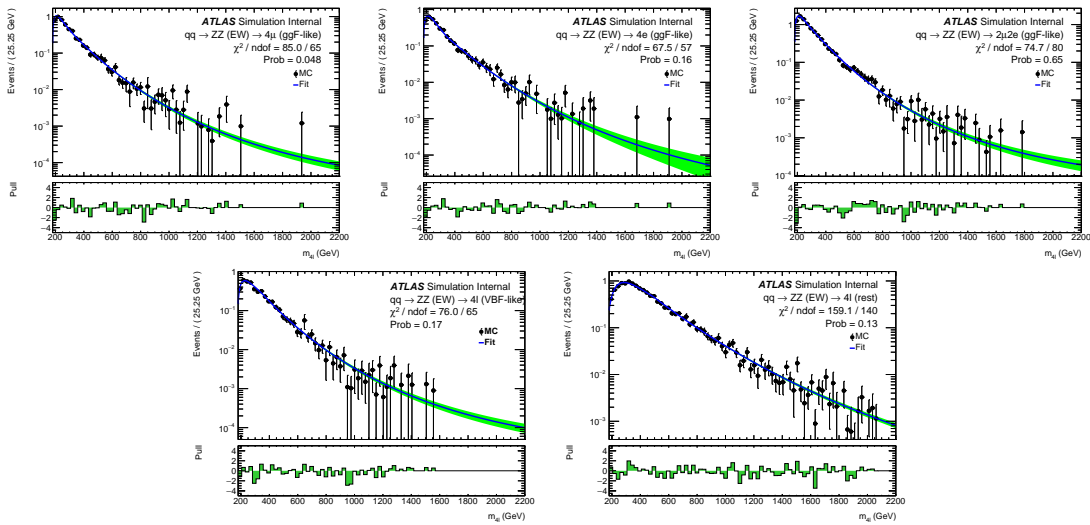


Fig. 6.14 Distributions of the $m_{4\ell}$ invariant mass fit projections of the $q\bar{q} \rightarrow ZZ$ (EW) background samples for the 4μ , $4e$ and $2\mu2e$ final states in the ggF category, the 4ℓ inclusive VBF category, and the “rest” category. DNN-based categorization is used.

isolated leptons. The simulations are not very robust in terms of the selection efficiencies. Thus, the data-driven method is applied to estimate the normalization of those processes in different control regions (CRs). The estimations in this analysis are performed separately for $\ell\ell + \mu\mu$ and $\ell\ell + ee$ final states, with slightly different approaches for “muon” and “electron” backgrounds.

The “electron” background mostly comes from process of a Z boson with light-flavour jets ($Z+LF$) that are misidentified as electrons. The large contribution of “muon” background comes from heavy-flavour jets produced in association with a Z boson ($Z+HF$) or in the decays of top quark. The estimations are done following the common H4l studies without a specific $m_{4\ell}$ range requirement^[102], and then the corresponding fraction of event yield in $m_{4\ell} > 200$ GeV is calculated from MC simulation.

$\ell\ell + \mu\mu$ final states

The normalizations of “muon” backgrounds are extracted from simultaneous fits of the leading lepton pair’s invariant mass (m_{12}) in four orthogonal CRs:

- **Inverted d_0 CR:** this CR is formed by inverting the d_0 selection for at least one lepton in subleading lepton pair while the leptons in leading pair are required to pass all standard selection. This CR enhances $Z+HF$ and $t\bar{t}$ as leptons from heavy-flavour hadronic decays are characterised by large d_0 .
- **$e\mu + \mu\mu$ CR:** this CR is formed using an opposite-charge different-flavour dilepton in leading pair. It aims to enhance $t\bar{t}$ background as the leading lepton pair cannot come from Z boson decay.
- **Inverted isolation CR:** in this CR, leptons in leading pair are required to satisfy all standard analysis selection, while for leptons in subleading pair, they are required to pass d_0 selection but have at least one of them failing isolation selection. This CR enhances the events from $Z+LF$ processes while suppress $Z+HF$ by d_0 cut.
- **Same-sign CR:** in this CR, the leptons in subleading pair are required to have same-charge, while the leading pair still passes standard selection. This CR is not dominant by any specific background since all of reducible backgrounds could have sizable contribution in it.

The fit results of normalizations are then propagated to signal region (SR) by applying transfer factors to account the difference of selection efficiencies between SR and CRs. The transfer factors are computed using $Z + \mu$ MC samples.

$\ell\ell + ee$ final states

The “electron” backgrounds are estimated in $3\ell + X$ CR, where X denotes the lower p_T electron in the subleading pair. The selection and identification criteria for X are relaxed

, while other three leptons must satisfy the standard selection. In this case, X could be a light-flavour jet, a photon conversion or an electron from heavy-flavour hadron decay. Moreover, the subleading pair is required to have same charge dilepton to ensure the orthogonality to the signal region. The normalization of backgrounds are obtained based on a fit to the number of hits in the innermost ID layer in CR, and the transfer factors are computed from $Z + e$ simulated sample.

The $m_{4\ell}$ shapes of reducible backgrounds are obtained from MC simulation in signal region, and then smoothed by an one-dimensional kernel estimation, which model the input data as a superposition of Gaussian kernels, one for each data point with contributing $1/N$ to total integral N ^[103]. Additional shape uncertainty from using different smoothing strength (ρ) in kernel estimation is token into account for these backgrounds.

6.5 Signal modelling

The parameterization based on simulated samples of $m_{4\ell}$ distributions for signals are described in this section. Several signal models are studied in this analysis, including heavy Higgs like narrow-width signal (NWA) and large-width signal (LWA), as well as the modelling of Randall-Sundrum graviton (RSG) signal.

6.5.1 Modelling of narrow-width signal

For narrow-width (NWA) signal, the $m_{4\ell}$ width is totally determined by detector resolution, which is modelled by the sum of a Crystal Ball (C) function^[104–105] and a Gaussian (G) function:

$$P_s(m_{4\ell}) = f_C \cdot C(m_{4\ell}; \mu, \sigma_C, \alpha_C, n_C) + (1 - f_C) \cdot G(m_{4\ell}; \mu, \sigma_G) \quad (6.3)$$

The two functions share the same central value μ , while the resolution parameters, σ_C and σ_G , are different. In the Crystal Ball function, the parameters α_C and n_C model the shape of non-Gaussian tail, and the fraction parameter f_C is used to ensure the relative normalization between two functions.

The parameters are obtained by fitting to signal MC simulations combining the mc16a, mc16d and mc16e campaigns for each category separately at each mass points from 200 GeV to 2000 GeV, and the shape of ggF and VBF signals are found to be similar. Figure 6.15 shows the $m_{4\ell}$ distribution and fitted curves for ggF production at mass from 200 GeV to 2000 GeV in $2e2\mu$ channel as examples.

Then the $C + G$ parameters are fitted with a polynomial as functions of generated mass

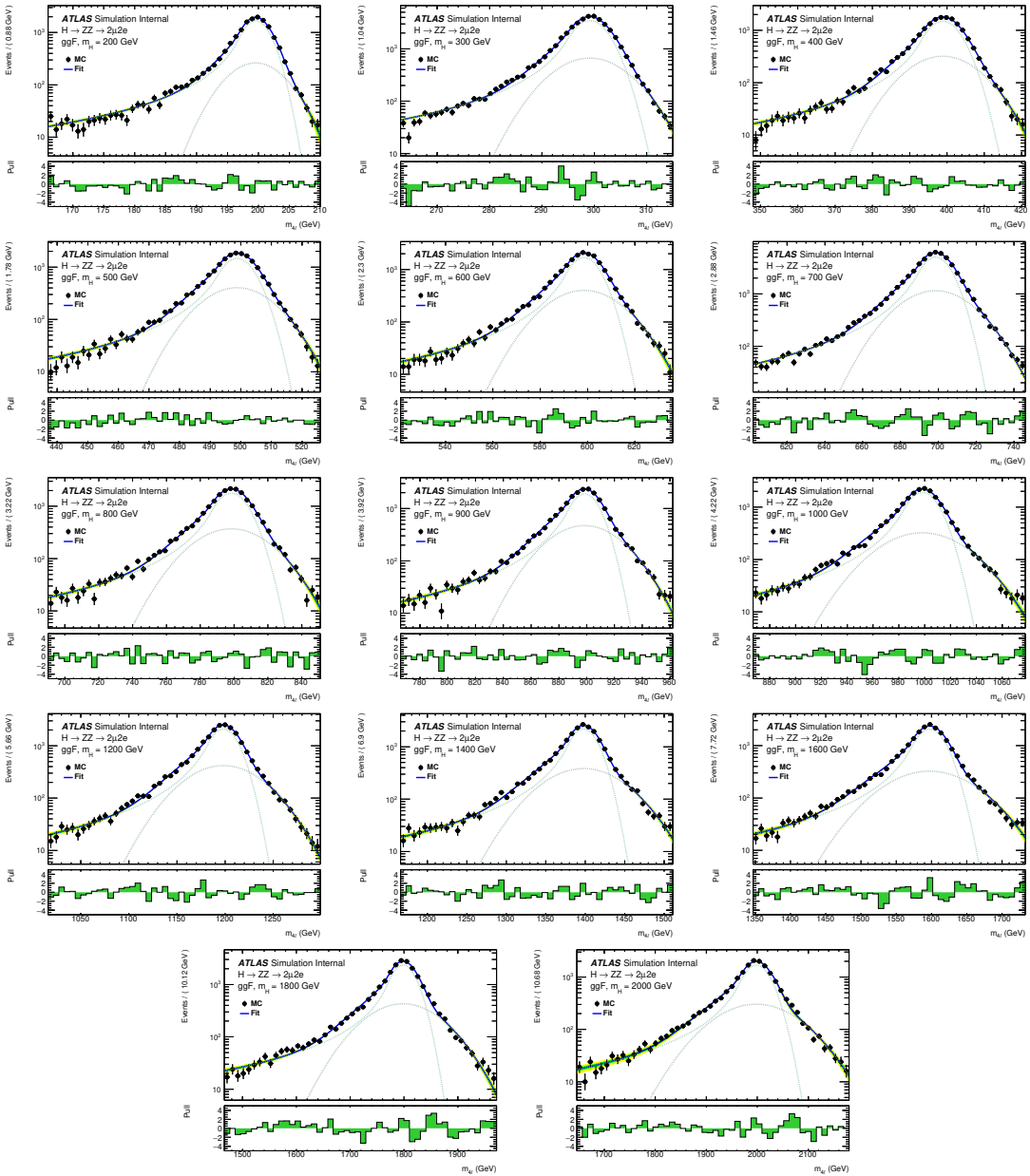


Fig. 6.15 Distributions of the $m_{2\mu 2e}$ and fit projection for signal samples between 200 to 3000 GeV for ggF production mode. Three MC campaigns, mc16a, mc16d and mc16e, are combined. The lower panel in each plot shows the pull distribution.

points (m_H) for samples, as an example shown in figure 6.16 for $2e2\mu$ channel. The fitting quality can be measured by the Pearson’s χ^2 , which is within 3 (2) for $2e2\mu$ ($4e$ and 4μ) channel.

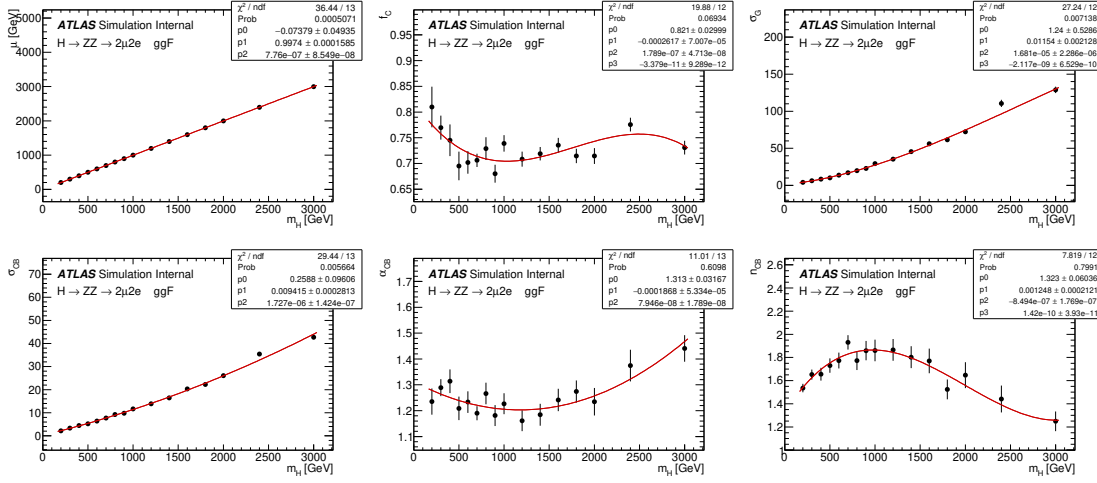


Fig. 6.16 Polynomial fits of the parameters μ , f_C , σ_G , σ_C , n_C and α_C for the signal $\mathcal{C} + \mathcal{G}$ model in the $2\mu 2e$ channel as a function of m_H for the ggF production mode. The combination of the mc16a, mc16d and mc16e MC campaigns is used.

In addition, possible difference on the signal yield extracted from parameterization and MC simulation is studied. Figure 6.17 shows this difference by computing $\frac{N_{\text{reco}} - N_{\text{fit}}}{N_{\text{fit}}}$, where N_{reco} denotes the total number of reconstructed events observed from MC simulation at that mass point and N_{fit} depicts the number of events obtained from the fitted PDF. The differences are treated as an additional systematic uncertainty with the value of 2% (1%) for $2e2\mu$ ($4e$ and 4μ) channel in the analysis.

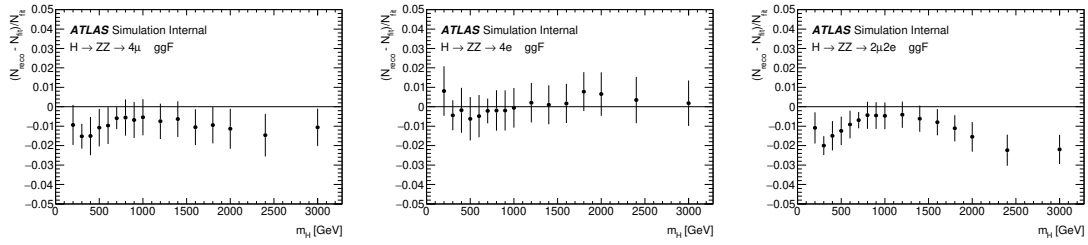


Fig. 6.17 The difference between MC simulation and parameterization of 4μ (left), $4e$ (middle) and $2\mu 2e$ (right) for the ggF production mode. The combination of the mc16a, mc16d and mc16e MC campaigns is used.

In summary, the final interpolated signal shapes for the ggF production mode are shown together in figure 6.18 for mass points with step of 100 GeV from 200 GeV to 3000 GeV.

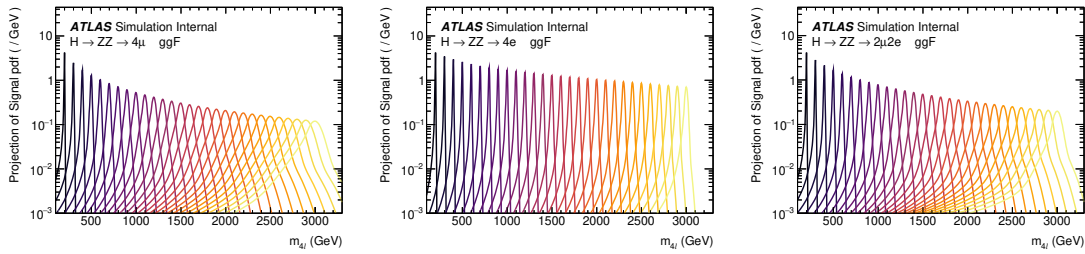


Fig. 6.18 The final signal shapes for the ggF production mode, interpolated from the polynomial fit parameters.

6.5.2 Modelling of large-width signal

The $m_{4\ell}$ shape of heavy Higgs model in large-width (LWA) hypothesis can be described by a convolution of a truth distribution with a resolution from detector effect. The detector resolution effect can be modelled by the function described in NWA parameterization, as in NWA model the truth level width is negligible and the shape is dominant by detector effect.

The differential parton cross section for the heavy Higgs model can be written as^[106]:

$$\sigma_{gg \rightarrow H \rightarrow ZZ}(s) = \frac{1}{2s} \int d\Omega |A_{gg \rightarrow H}(s, \Omega)|^2 \frac{1}{|s - s_H|^2} |A_{H \rightarrow ZZ}(s, \Omega)|^2 \quad (6.4)$$

where $A_{gg \rightarrow H}(s, \Omega)$ and $A_{H \rightarrow ZZ}(s, \Omega)$ are corresponding Higgs production and decay amplitudes, and $\frac{1}{|s - s_H|}$ denotes the Higgs propagator and Ω represents the phase space of the process.

Using the definition of a partial width,

$$\Gamma_{H \rightarrow F}(s) = \frac{1}{2\sqrt{s}} \int d\Omega |A_{H \rightarrow F}(s, \Omega)|^2 \quad (6.5)$$

the parton cross section can be rewritten as,

$$\sigma_{gg \rightarrow H \rightarrow ZZ}(s) = 2 \frac{1}{|s - s_H|^2} \times \Gamma_{H \rightarrow gg}(s) \times \Gamma_{H \rightarrow ZZ}(s) \quad (6.6)$$

with the components computed in Ref^[106-107]:

$$\begin{aligned} \frac{1}{s - s_H} &= \frac{1 + i \cdot \bar{\Gamma}_H / \bar{m}_H}{s - \bar{m}_H^2 + i \cdot s \cdot \bar{\Gamma}_H / \bar{m}_H} \\ \bar{m}_H &= \sqrt{\bar{\Gamma}_H^2 + m_H^2} \\ \bar{\Gamma}_H &= \bar{m}_H \cdot \frac{\Gamma_H}{m_H} \end{aligned} \quad (6.7)$$

$$\Gamma_{H \rightarrow ZZ}(s) = C \cdot s^{\frac{3}{2}} \cdot \left[1 - \frac{4m_Z^2}{s} + \frac{3}{4} \left(\frac{4m_Z^2}{s} \right)^2 \right] \cdot \left[1 - \frac{4m_Z^2}{s} \right]^{\frac{1}{2}} \quad (6.8)$$

$$\begin{aligned} \Gamma_{H \rightarrow gg}(s) &= C \cdot s^{\frac{3}{2}} \cdot |A_t(\tau_t)|^2 \\ A_t(\tau) &= 2 \frac{\tau + (\tau - 1)f(\tau)}{\tau^2} \\ \tau_t &= \frac{s}{4m_t^2} \\ f(\tau) &= \begin{cases} \arcsin^2(\sqrt{\tau}), & \tau \leq 1 \\ -\frac{1}{4} \left[\log \frac{1+\sqrt{1-\tau^{-1}}}{1-\sqrt{1-\tau^{-1}}} - i\pi \right]^2, & \tau > 1 \end{cases} \end{aligned} \quad (6.9)$$

where m_f stands for the mass of a fermion f , and Γ_H denotes an assumed total width of the heavy Higgs boson.

At the LHC, the $m_{4\ell}$ line shape can be defined by a hadron cross section that is derived from equation 6.6 by multiplication with gluon-gluon luminosity \mathcal{L}_{gg} described in^[108]. Meanwhile, the cross section is rewritten as a function of $m_{4\ell}$ instead of s , which will give an extra power of mass dependence in the formula:

$$\sigma_{pp \rightarrow H \rightarrow ZZ}(m_{4\ell}) = 2 \cdot m_{4\ell} \cdot \mathcal{L}_{gg} \cdot \frac{1}{|s - s_H|^2} \cdot \Gamma_{H \rightarrow gg}(m_{4\ell}^2) \cdot \Gamma_{H \rightarrow ZZ}(m_{4\ell}^2) \quad (6.10)$$

The analytical shapes of truth level $m_{4\ell}$ distribution of gg2VV MC samples is shown on figure 6.19.

The reconstruction level signal shape can then be modelled by the analytical truth shape convoluted with detector effects modelled in section 6.5.1. A comparison between the modelled shape and reconstruction level MC simulation for signal mass above 400 GeV(for ggF production in $2e2\mu$ channel as an example) are shown in figure 6.20, the shapes are well compatible between each other. This modelling is not valid for lower masses due to the rapid change of detector resolution and it is incorrect to assume a constant detector resolution under the peak.

6.5.3 Modelling of interference

There are three processes sharing the same gg initial state and $Z Z$ final state:

- The SM $gg \rightarrow ZZ$ process with an amplitude A_B
- The SM (light) Higgs at mass of around 125 GeV with an amplitude A_h
- The BSM heavy Higgs we are searching in this analysis with an amplitude A_H

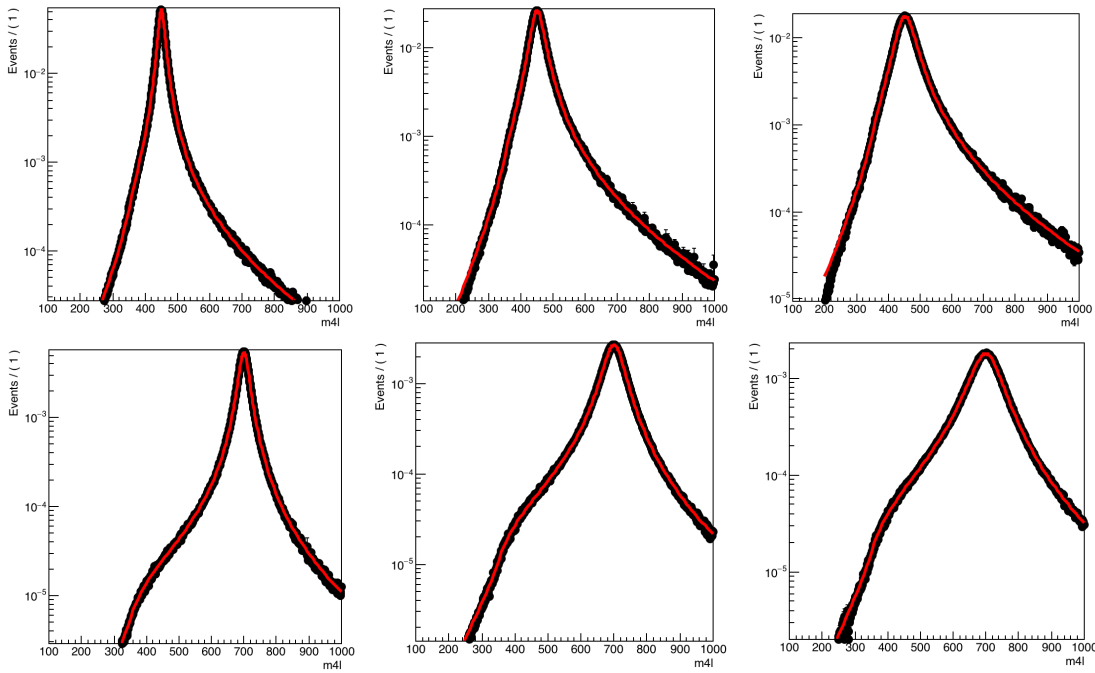


Fig. 6.19 Comparison of the analytical shape to a truth $m_{4\ell}$ distribution of gg2VV MC samples for $m_H = 450$ GeV (top), 700 GeV (bottom) and width equal to 5% (left), 10% (middle), 15% (right) of the mass.

The three processes can interfere with each other due to the same initial and final states. The parton cross section for these processes can be written as:

$$\begin{aligned}
 \sigma_{gg \rightarrow (X) \rightarrow ZZ}(s) &= \frac{1}{2s} \int d\Omega |A_h(s, \Omega) + A_H(s, \Omega) + A_B(s, \Omega)|^2 \\
 &= \frac{1}{2s} \int d\Omega \left(|A_h(s, \Omega)|^2 + |A_H(s, \Omega)|^2 + |A_B(s, \Omega)|^2 \right) + \\
 &+ \frac{1}{s} \int d\Omega \left(\text{Re}[A_h(s, \Omega) \cdot A_B^*(s, \Omega)] \right. \\
 &\quad \left. + \text{Re}[A_H(s, \Omega) \cdot A_B^*(s, \Omega)] + \text{Re}[A_H(s, \Omega) \cdot A_h^*(s, \Omega)] \right) \\
 &+ \frac{1}{s} \text{Re} \left[\frac{1}{s - s_H} \int d\Omega \cdot A_H^P(s, \Omega) \cdot A_H^D(s, \Omega) \cdot A_B^*(s, \Omega) \right] \\
 &+ \frac{1}{s} \int d\Omega \cdot \text{Re} \left[A_H^P(s, \Omega) \cdot \frac{1}{s - s_H} \cdot A_H^D(s, \Omega) \cdot A_h^{P*}(s, \Omega) \cdot \frac{1}{(s - s_h)^*} \cdot A_h^{D*}(s, \Omega) \right]
 \end{aligned} \tag{6.11}$$

The first term in equation 6.11 denotes the on-shell SM Higgs contribution at around 125 GeV, which is negligible in this analysis. The second term corresponds to the heavy Higgs contribution, whose line shape has been described in previous section. The third term is the $gg \rightarrow ZZ$ continuum process, while the forth term is the interference between SM Higgs and $gg \rightarrow ZZ$ continuum. The fifth and sixth terms are the interferences between heavy Higgs and $gg \rightarrow ZZ$ continuum (H-B), and between heavy Higgs and

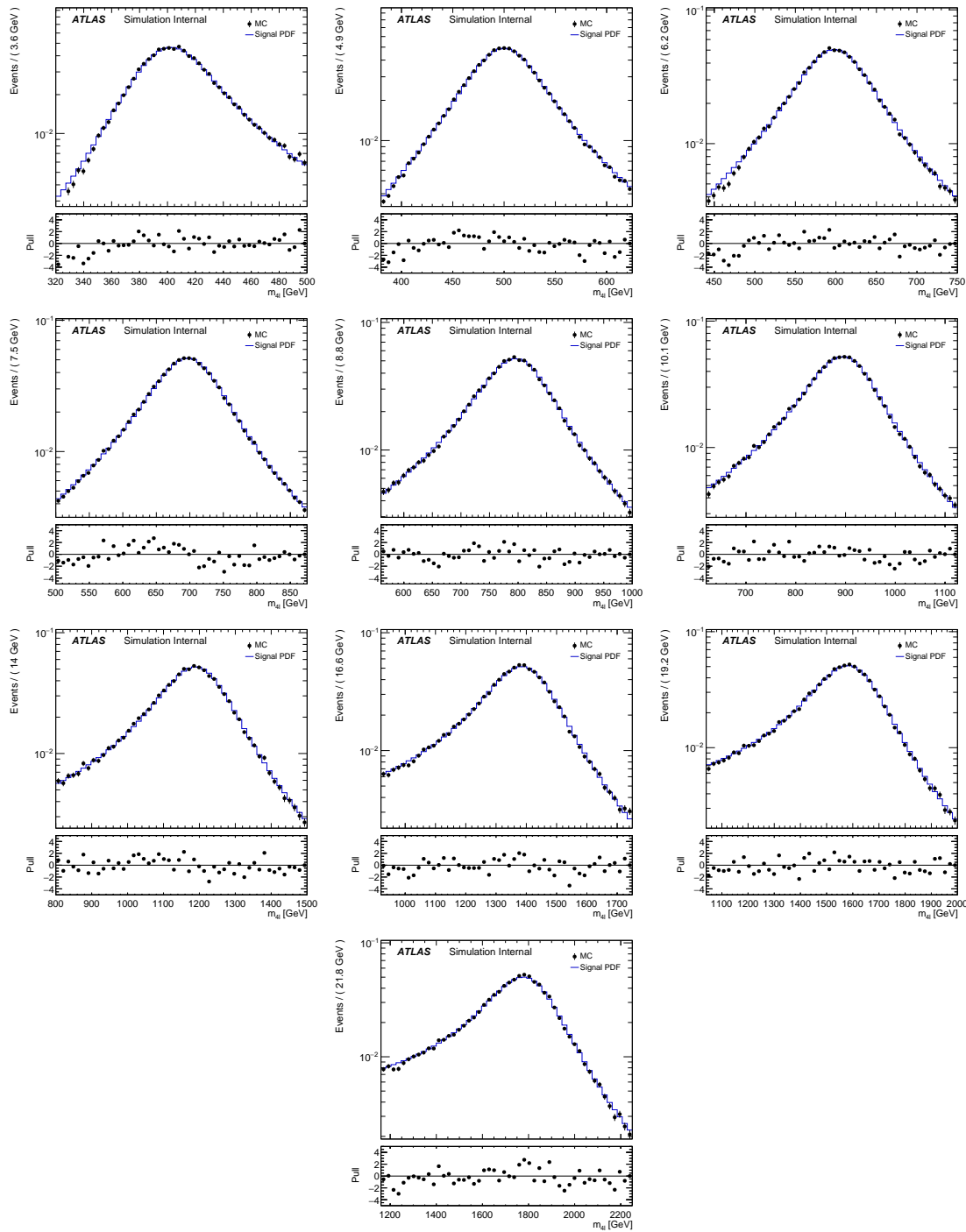


Fig. 6.20 Comparison between the analytical shape convoluted with detector effects and the reconstructed $m_{2\mu 2e}$ MC distribution for mass points ranging from 400 to 1800 GeV and width equal to 15% of the mass.

SM Higgs (H - h) that this analysis is interested in. More details about the parameterization of these two interferences are described as below.

1. Interference between heavy Higgs and $gg \rightarrow ZZ$ continuum

The parton cross section of this interference term has been written down in equation 6.11. By assuming that this function has a smooth behaviour, it can be replaced with complex polynomial:

$$\int d\Omega \cdot A_H^P(s, \Omega) \cdot A_H^D(s, \Omega) \cdot A_B^*(s, \Omega) \approx (a_0 + a_1 \cdot \sqrt{s} + \dots) + i \cdot (b_0 + b_1 \cdot \sqrt{s} + \dots) \quad (6.12)$$

The parameters a_i and b_i can be extracted by fitting to the $m_{4\ell}$ distribution from truth level MC simulation after analysis selection. Since the signal mass and width does not enter into this function, the parameters should be independent for every tested signal hypothesis.

Same as description for equation 6.10, the parton cross section can be transformed into a hadron cross section as a function of $m_{4\ell}$:

$$\sigma_{pp}(m_{4\ell}) = \mathcal{L}_{gg} \cdot \frac{1}{m_{4\ell}} \cdot \text{Re} \left[\frac{1}{s - s_H} \cdot ((a_0 + a_1 \cdot m_{4\ell} + \dots) + i \cdot (b_0 + b_1 \cdot m_{4\ell} + \dots)) \right] \quad (6.13)$$

where the propagators are shown in equation 6.7.

Figure 6.21 shows the distributions of interference function obtained by simultaneous fitting to $m_{4\ell}$ shape from truth level H-B interference simulation at different mass in $2e2\mu$ channel as an example.

2. Interference between heavy Higgs and SM Higgs

The parton cross section of this interference term has been written down in equation 6.11. By assuming the production and decay amplitudes are the same for heavy Higgs boson and SM Higgs boson, the cross section function can be simplified to:

$$\sigma_{gg}(s) = \frac{1}{s} \int d\Omega \cdot \text{Re} \left[\frac{1}{s - s_H} \cdot \frac{1}{(s - s_h)^*} \right] \cdot |A_{gg \rightarrow H}(s, \Omega)|^2 |A_{H \rightarrow ZZ}(s, \Omega)|^2 \quad (6.14)$$

Taking into account Equation 6.5:

$$\sigma_{gg}(s) = 4 \cdot \text{Re} \left[\frac{1}{s - s_H} \cdot \frac{1}{(s - s_h)^*} \right] \cdot \Gamma_{H \rightarrow gg}(s) \cdot \Gamma_{H \rightarrow ZZ}(s) \quad (6.15)$$

where the propagators are described in equation 6.7, and the partial widths are described in equations 6.8 and 6.9.

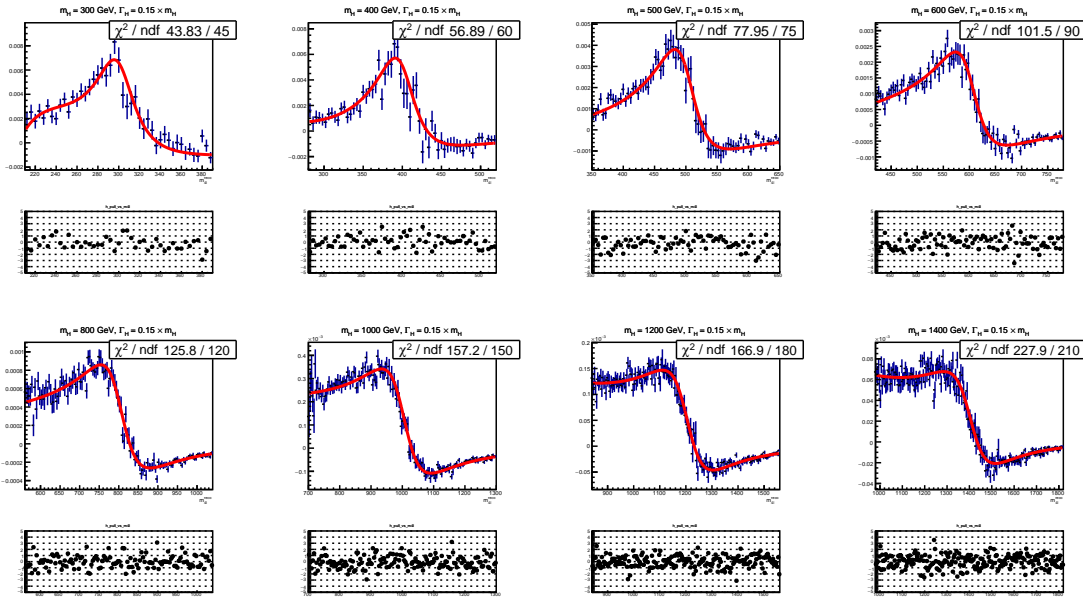


Fig. 6.21 The interference (H-B) model fitted to the truth $m_{4\ell}$ MC distribution after signal region selection for $2\mu 2e$ channel.

Same as previous procedure, the parton cross section can be transformed to a hadron cross section as a function of $m_{4\ell}$:

$$\sigma_{pp}(m_{4\ell}) = 4 \cdot m_{4\ell} \cdot \mathcal{L}_{gg} \cdot \text{Re} \left[\frac{1}{s - s_H} \cdot \frac{1}{(s - s_h)^*} \right] \cdot \Gamma_{H \rightarrow gg}(m_{4\ell}) \cdot \Gamma_{H \rightarrow ZZ}(m_{4\ell}) \quad (6.16)$$

The modelling procedure of interference is the same as the way for large-width signal described in section 6.5.2. The truth line shape is measured as analytical function from equation 6.16, and then convolute with detector effect from NWA parameterization to get the reconstruction level shape.

For LWA signal model, these two interferences are carefully taken into account, and the integration of the pure LWA signal with the interferences is used for further studies. Figure 6.22 shows the signal model for large-width scenario at mass points of 400 GeV, 600 GeV, 800 GeV, for three different signal widths: 5%, 10%, 15%, with and without interference. Additionally, the contribution of the interference between heavy Higgs and SM Higgs (H-h) is shown together with the one between heavy Higgs and SM $gg \rightarrow ZZ$ background (H-b). One can see the interference effect on signal shape becomes less important when going to higher mass.

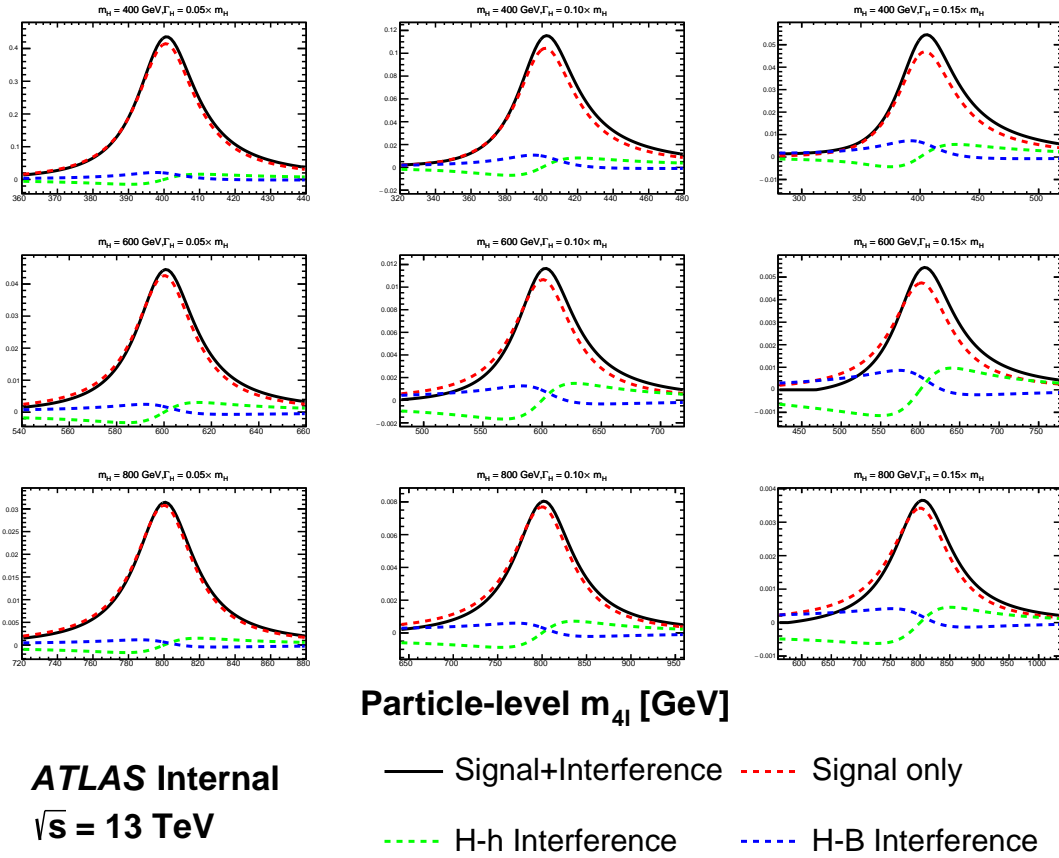


Fig. 6.22 The signal modelling for the large-width scenario at m_H of 400 GeV (top), 600 GeV (middle) and 800 GeV (bottom), as well as three different signal width: 5% (left), 10% (middle) and 15% (right). The contribution of the interference between heavy Higgs and SM Higgs (H-h) is shown together with the one between heavy Higgs and SM $gg \rightarrow ZZ$ background (H-b).

6.5.4 Modelling of spin-2 RS Graviton signal

The search for Randall-Sundrum (RS) graviton is performed in mass region between 600 to 2000 GeV. The width of resonance is determined by the $k/\overline{M}_{\text{Planck}}$, which, as mentioned in section 6.2.3, is set to be 1. In this configuration, the width of signal is expected to be about 6% of its mass.

The reconstructed $m_{4\ell}$ lineshape of graviton is also built by convolving the truth-level lineshape with a detector resolution function, where the detector resolution effect is modelled by a Gaussian + Crystal Ball function, whose parameters are taken from the NWA signal parameterization in section 6.5.1. And for truth-level shape, for graviton, it's modelled as the product of a relativistic Breit-Wigner (RBW) term, a term corresponding to the squared matrix element of the production process and a parton luminosity term \mathcal{L}

as given in [109]. So the truth lineshape of $m_{4\ell}$ is taken from:

$$m_{4\ell}^{\text{Truth}} \sim \mathcal{L}_{gg} \cdot s^2 \cdot \frac{s(1+s)(1+2s+2s^2)}{(s^2 - m_G^2)^2 + m_G^2 \Gamma^2}$$

The truth-level signal model is extracted by fit to MC simulation at truth-level with the mass m_G and width Γ parameters floating at each mass points respectively. And then the two parameters are parameterized as the function of m_H by a linear fit as shown in figure 6.23.

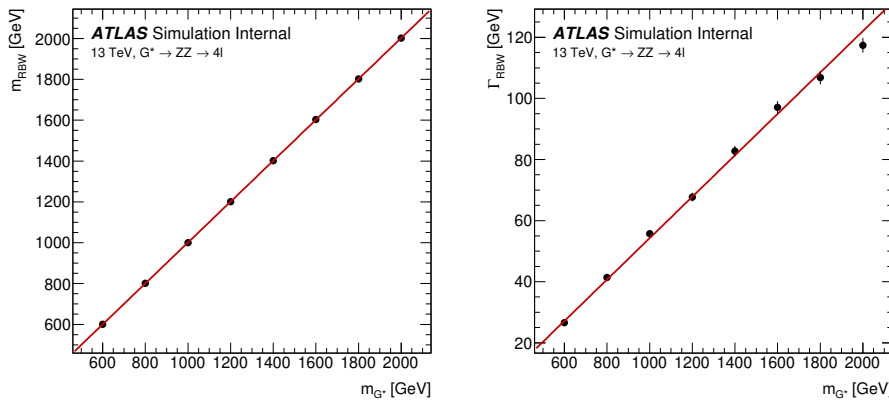


Fig. 6.23 Fitted parameters of the graviton RBW, m_{RBW} and Γ_{RBW} , as a function of the graviton resonance mass, m_G .

The final signal model is obtained by convolving the truth-level lineshape with the detector resolution function. To verify the result, figure 6.24 compares the $m_{4\ell}$ lineshape from parameterization with the one observed from reconstructed-level MC simulation in $2e2\mu$ channel at masses of 600 GeV, 1600 GeV and 2000 GeV as examples.

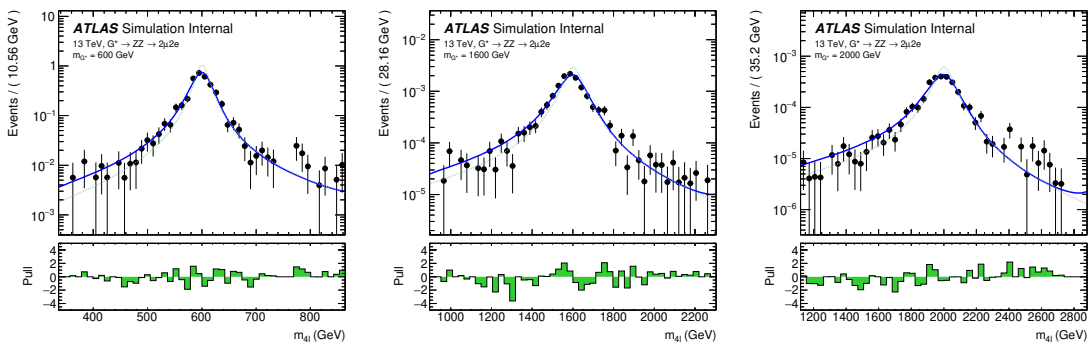


Fig. 6.24 Reconstructed $m_{4\ell}$ distributions in the $2\mu 2e$ channel with the final signal model superimposed for each RS graviton signal sample at masses of 600 GeV, 1600 GeV and 2000 GeV. The lower panel in each plot shows the pull distribution. The dashed green lines show the truth-level graviton signal models for reference.

6.6 Systematic uncertainties

This section describes the sources and value of theoretical and experimental systematic uncertainties considered in this analysis. In addition, as mentioned in previous sections, the uncertainties of irreducible background modelling, reducible background shape smoothing procedure and signal yield difference between simulation and parameterization are all taken into account.

6.6.1 Theoretical uncertainties

The theoretical modelling uncertainties include the PDF variations, missing QCD higher-order corrections via the variations of factorisation and renormalization scales, and the parton showering uncertainties.

1. Theoretical uncertainties for signal

The PDF, QCD scale and parton showering uncertainties affecting the acceptance difference originating from analysis selection for signal are taken into account in different categories. The acceptance uncertainties are calculated on the acceptance factor which extrapolates from the fiducial space to the full phase space by a simple ratio:

$$A = \frac{N_{fiducial}}{N_{total}} \quad (6.17)$$

For PDF uncertainties, the standard derivations of 100 PDF replicas of NNPDF3.0 NNLO, as well as comparison to two external PDF sets: MMHT2014 NNLO, CT14 NNLO are considered. For missing QCD higher-order corrections, the effects are studied with truth events by comparing weights corresponding to variations of the renormalization and factorization scale factors, up and down by a factor of two, and the envelop of different variations are used. The parton showering uncertainties are estimated by comparing events with different setting via Pythia8.

Systematic uncertainties are studied for both cut- and DNN- based event categorizations respectively, in two different categories: the inclusive ggF and VBF category for cut-based analysis and three different categories: inclusive ggF, VBF, “rest” category for DNN-based one. Only DNN-based results are shown in this section as examples.

Table 6.7 and 6.8 show the theoretical uncertainties mentioned above for ggF and VBF signal respectively in DNN-based categorization.

2. Theoretical uncertainties for SM background processes

The theoretical uncertainties of irreducible $Z Z$ backgrounds are considered in terms of both the variations of shape of $m_{4\ell}$ distributions and the acceptance originating from

Table 6.7 Summary of acceptance uncertainties of PDF, QCD scale and parton shower variations for ggF production. The DNN-based categorization is used.

Categories	PDF	QCD Scale	Parton Shower
ggF	0.40%	0.06%	2.03%
rest	0.56%	0.07%	4.86%
VBF	0.53%	0.09%	3.43%

Table 6.8 Summary of acceptance uncertainties of PDF, QCD scale and parton shower variations for VBF production. The DNN-based categorization is used.

Categories	PDF	QCD Scale	Parton Shower
ggF	0.18%	1.20%	0.41%
resr	0.43%	0.26%	0.36%
VBF	0.23%	3.19%	0.85%

the event selection.

The PDF and QCD scale uncertainties are considered by using the same method as described for signal in section 1. The parton showering uncertainties for those Sherpa samples are evaluated by varying the resummation scale by a factor of 2, changing the CKKW setting and using different showering option, following the PMG recommendation in ref.^[110], and the quadratic sum between the uncertainties in different kinds of showering option is taken as final result of uncertainties. Moreover, the shape uncertainty associated with electroweak higher-order correction for $q\bar{q} \rightarrow ZZ$ process is also taken into account.

Same as for signals, these theoretical uncertainties for irreducible backgrounds are studied for both cut- and DNN- based event categorizations. The value of shape uncertainties vary from less than 1% at low mass region to 50% at high mass tail due to large statistic fluctuation at tail. As for acceptance uncertainties, the values vary from about 1% for PDF variations to 40% for parton showering variations in DNN-based analysis for VBF category.

As an example, table 6.9 summarizes the acceptance uncertainties of PDF, QCD scale, and parton showering variations for the dominant background: $q\bar{q} \rightarrow ZZ$ process.

Table 6.9 Summary of acceptance uncertainties of PDF, scale, and parton showering variations for QCD $q\bar{q} \rightarrow ZZ$ background. The DNN-based categorization is used.

Categories	PDF	QCD Scale	Parton showering
ggF	1.15%	10.16 %	3.71%
rest	1.04%	3.26 %	3.80%
VBF	2.91%	27.90 %	23.82%

6.6.2 Experimental systematics

The signal and background predictions used in this analysis are also affected by various sources of experimental systematic uncertainties. Similar as described in section 5.5.2 in VBS ZZ analysis, the dominant experimental uncertainties in this analysis come from the energy/momenta scales and reconstruction and identification efficiencies of the leptons and jets, as well as the luminosity uncertainty. The systematic uncertainties are calculated using the recommendations from the Combined Performance (CP) groups. Table 6.10 summarizes the experimental systematics considered in this analysis that affect either the normalization of total event yield or the shape of $m_{4\ell}$ distribution. The impact of those systematics in statistical fit will be studied in section 6.7.

6.7 Results in $\ell\ell\ell\ell$ channel

The statistical treatment to search for heavy resonances in signal region is described in this section. Results are presented in both cut- and DNN- based analysis.

6.7.1 Statistical procedure

The upper limits on heavy resonances are obtained using the unbinned profile likelihood fits. $m_{4\ell}$ is the discriminant. The likelihood function is a product of a Poisson term representing the probability of observing n events and a weighted sum of both signal and background probability distribution functions (PDFs) evaluated at all observed events.

$$L(x_1..x_n | \sigma_{ggF}, \sigma_{VBF}) = \text{Pois}(n | S_{ggF} + S_{VBF} + B) \left[\prod_{i=1}^n \frac{S_{ggF} f_{ggF}(x_i) + S_{VBF} f_{VBF}(x_i) + B f_B(x_i)}{S_{ggF} + S_{VBF} + B} \right] \quad (6.18)$$

where f_X s are the probability distribution functions of signal and backgrounds modelled in section 6.5 and 6.4, and S_X and B are the normalizations of signal and sum of backgrounds.

The parameters of interest (POI) in the search is σ_{ggF} (and σ_{VBF} only for NWA signal), which is the cross section of signal model in ggF (and VBF) production mode. When setting a limit on one POI, the other is either fixed at 0, or profiled along with other nuisance parameters (except left unconstrained) during the minimization. These POIs enter the likelihood inside the expected signal yields S_{ggF} and S_{VBF} as follows:

$$S_{ggF(VBF)} = \sigma_{ggF(VBF)} \times BR(S \rightarrow ZZ \rightarrow 4\ell) \times A \times C \times \int \mathcal{L} \quad (6.19)$$

where $A \times C$ is the signal acceptance as parameterized in 6.3.4, and $\int \mathcal{L} = 139 \text{ fb}^{-1}$ is the integrated luminosity of the dataset.

The dependence of the expected number of signal and background events (normalizations) and the shape of the PDFs on the systematic uncertainties measured in section 6.6 is described by a set of nuisance parameters (NP) θ_i . The Gaussian constraints are applied to those NPs. The constraints are implemented as additional ‘penalty’ terms added to the likelihood which will increase the negative log-likelihood when any nuisance parameter is shifted from its nominal value. The final likelihood function $L(\sigma_{ggF}, \sigma_{VBF}, m_H, \theta_i)$, is therefore a function of σ_{ggF} , σ_{VBF} , m_H , and θ_i .

Furthermore, the normalization of SM background $pp \rightarrow ZZ$, which include both $q\bar{q} \rightarrow ZZ$ and $gg \rightarrow ZZ$, is a free parameter (μ_{ZZ}) and profiled when fitting to the data. Floating $Z Z$ normalization in fit takes the advantage of reducing the dependence on theory predictions and their associated uncertainties, especially given that the increased data luminosity would provide precise determination of the SM $Z Z$ background rate.

At the end, the upper limit for the cross-section $\sigma_{ggF(VBF)}$ at a given heavy resonance model is obtained by setting the mass of signal m_H parameter as constant at the desired value, and maximising the likelihood function with respect to nuisance parameters. The $CL_s^{[111]}$ method is used to obtain exclusion limits.

6.7.2 Likelihood fit under background-only hypothesis for DNN-based analysis

Both DNN- and cut-based analysis are studied by performing likelihood fit to the (pseudo-)data under the background-only hypothesis and under different signal models. Due to the same background estimation and modelling procedures, as well same method of systematic measurements, as an example, this section only shows the results from background-only fits for DNN-based analysis under the model of heavy Higgs resonance with narrow-width. The final results of interpretation in both DNN- and cut- based analysis in all signal models described in section 6.5 will be measured in next section.

First of all, table 6.11 summarized the expected and observed number of events for region of $m_{4\ell} > 200$ GeV together with their systematic uncertainties after background only fit.

To inspect the likelihood model, pulls and constraints as well as the correlation matrix of nuisance paraemters (NP) are studied by performing a background only fit. Figure 6.25 shows the pulls and constraints when fitting to Asimov (top) and observed (bottom) data. Figure 6.26 shows the correlation matrix, only for NPs with correlation greater than 0.1. The normalization of $Z Z$ background is taken from data for one category each, as shown in table 6.12.

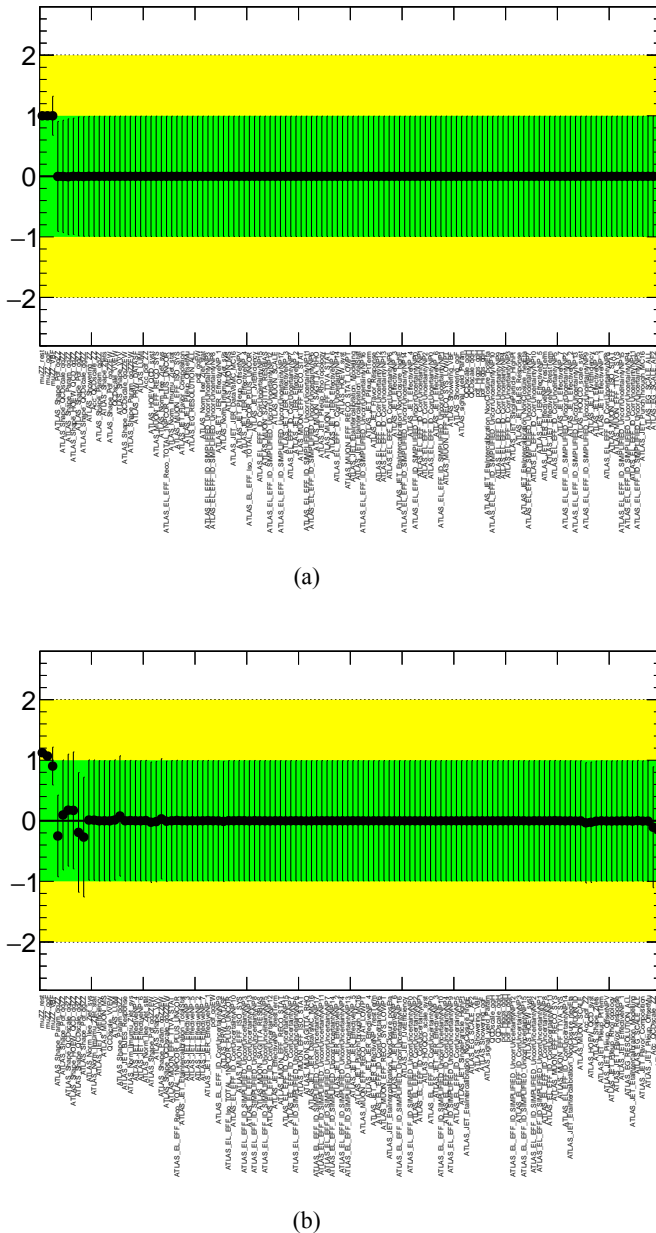
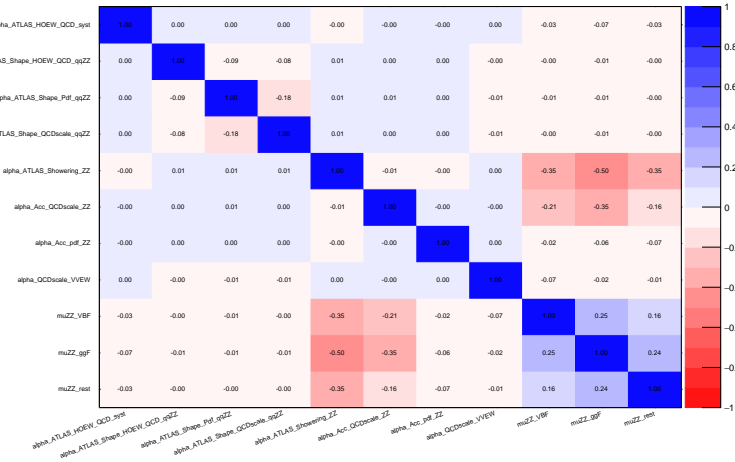


Fig. 6.25 Pulls and constraints of nuisance parameters after a background only fit to (a) Asimov data and (b) observed data in the $\ell\ell\ell\ell$ channel. The Asimov data is generated with background data only, and the observed data includes datasets from 2015 to 2018.

The impact of a systematic uncertainty on the result depends on the production mode as well as the mass hypothesis. To check the impact of systematic uncertainties on expected signal sensitivity, a NP ranking study is performed using signal injected Asimov data with the injected cross section close to 95% CLs upper limit at two masses: 400 GeV and 1000 GeV. The results are shown in Fig. 6.27 (6.28) for ggF (VBF) production mode. For ggF production, at lower masses, the systematic uncertainties of parton showering variation for signal, the luminosity uncertainty, and the parametrization of signal acceptance dominate, while at higher masses, the shape uncertainties from PDF variation



(a)

Fig. 6.26 Correlation of nuisance parameters after a background only fit to Asimov data in the $\ell\ell\ell\ell$ channel. The Asimov data is generated with background data only.

for ZZ ($q\bar{q} \rightarrow ZZ$ and $gg \rightarrow ZZ$) background become important, as also seen in VBF production mode. For VBF production, jet related uncertainties become more important comparing to ggF production. In addition, the dominate uncertainties include the acceptance uncertainty from QCD scale variation for signal and the luminosity uncertainty.

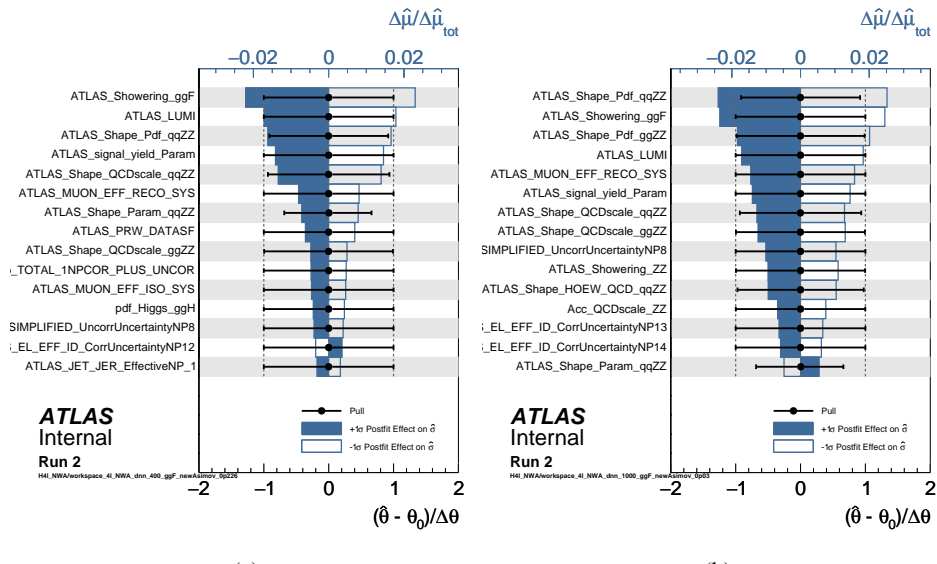


Fig. 6.27 NP ranking plot for the σ_{ggF} fit to Asimov data in the $\ell\ell\ell\ell$ channel. The Asimov data is injected with $\sigma_{ggF} = 0.226$ fb for $m_H = 400$ GeV (left) and $\sigma_{ggF} = 0.030$ fb for $m_H = 1000$ GeV (right).

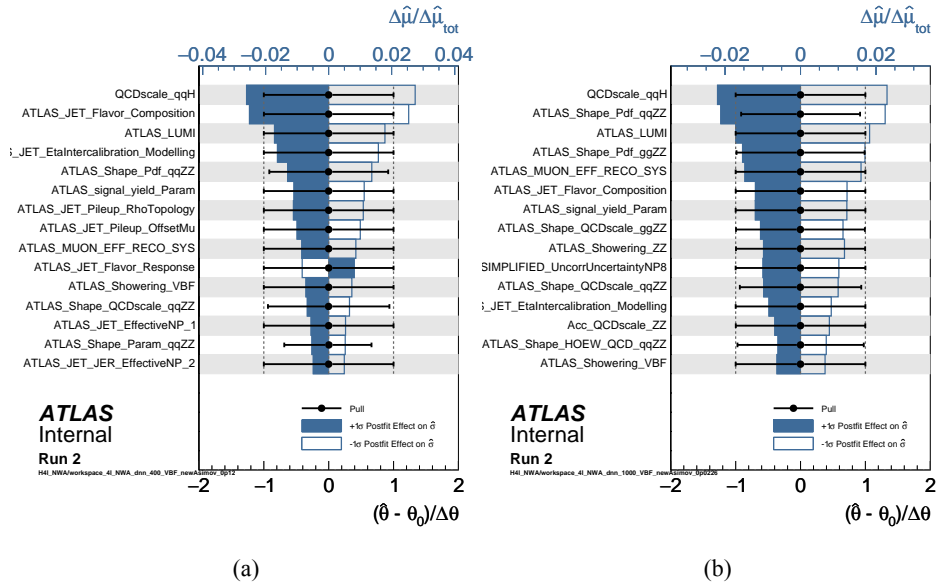


Fig. 6.28 NP ranking plot for the σ_{VBF} fit to Asimov data in the $\ell\ell\ell\ell$ channel. The Asimov data is injected with $\sigma_{VBF} = 0.120 \text{ fb}$ for $m_H = 400 \text{ GeV}$ (left) and $\sigma_{VBF} = 0.0226 \text{ fb}$ for $m_H = 1000 \text{ GeV}$ (right).

6.7.3 Interpretations

1. Spin-0 resonance with NWA

In the absence of a specific model, the ratio of ggF and VBF production mode is unknown for this additional heavy scalar. For this reason, the fits for ggF and VBF processes are done separately, and in each case the cross section of the other process is allowed to be a free parameter in fit. The observed and expected upper limit at 95% confidence level (CL) on the $\sigma \times BR(H \rightarrow ZZ)$ of a narrow scalar resonance for both ggF (left) and VBF (right) production mode with the integrated luminosity of 139 fb^{-1} is shown in figure 6.29 (6.30) for DNN- (cut-) based analysis. No excess over 2σ is found.

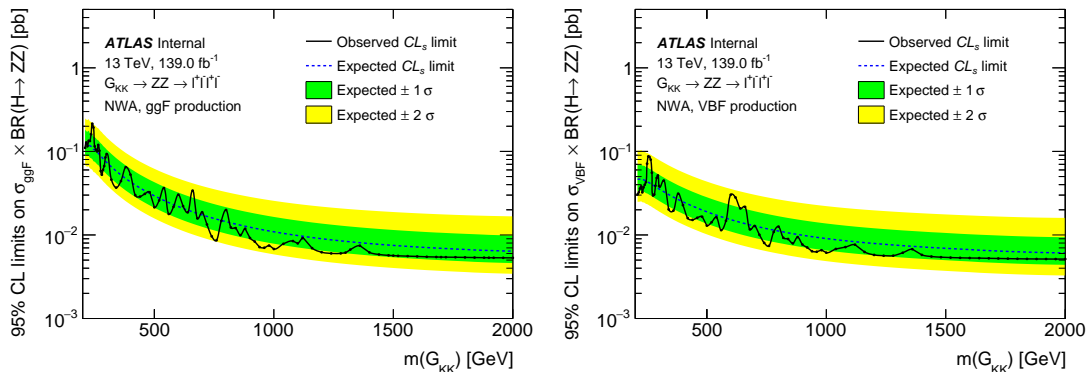


Fig. 6.29 The expected and observed upper limits at 95% CL on $\sigma \times BR(H \rightarrow ZZ)$ using the DNN-based analysis for ggF (left) and VBF (right) production. The green and yellow bands represent the $\pm 1\sigma$ and $\pm 2\sigma$ uncertainties in the expected limits.

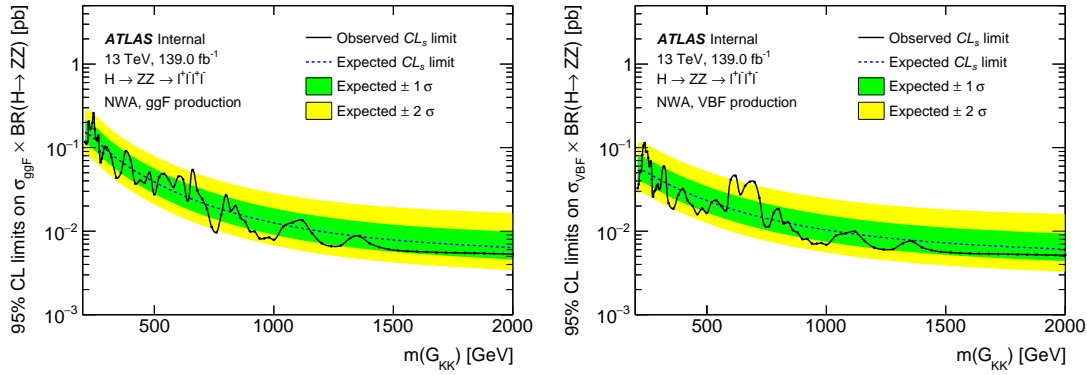


Fig. 6.30 The expected and observed upper limits at 95% CL on $\sigma \times BR(H \rightarrow ZZ)$ using the cut-based analysis for ggF (left) and VBF (right) production. The green and yellow bands represent the $\pm 1\sigma$ and $\pm 2\sigma$ uncertainties in the expected limits.

2. Spin-0 resonance with LWA

In the case of LWA model, only ggF production mode is studied. The interference between the heavy scalar and SM Higgs boson (H-h), as well as the heavy scalar and SM $gg \rightarrow ZZ$ continuum background (H-B) as modelled in section 6.5.3 are considered. The upper limit at 95% confidence level (CL) on ggF cross section times branch ratio ($\sigma_{ggF} \times BR(H \rightarrow ZZ)$) is shown in figure 6.31 for a width of 1%, 5%, 10% and 15% of m_H .

3. Spin-2 RS Graviton resonance

The observed and expected 95% upper limit on the cross section times branching ratio for RS Graviton (RSG) scenarios is shown in figure 6.32. Same as LWA case, for RSG interpretation, only $4e$, 4μ and $2e2\mu$ channel of ggF production are used. On top of the results in this analysis, a predicted cross section as function of mass provided by theorist is also shown. Comparing with the observed result provided by $ZZ \rightarrow \ell\ell\ell\ell$ decay, this spin-2 graviton is excluded up to a mass of around 1500 GeV.

4. Comparison between different models

As a summary, figure 6.33 shows the comparison of expected and observed 95% CL upper limits between different models described above.

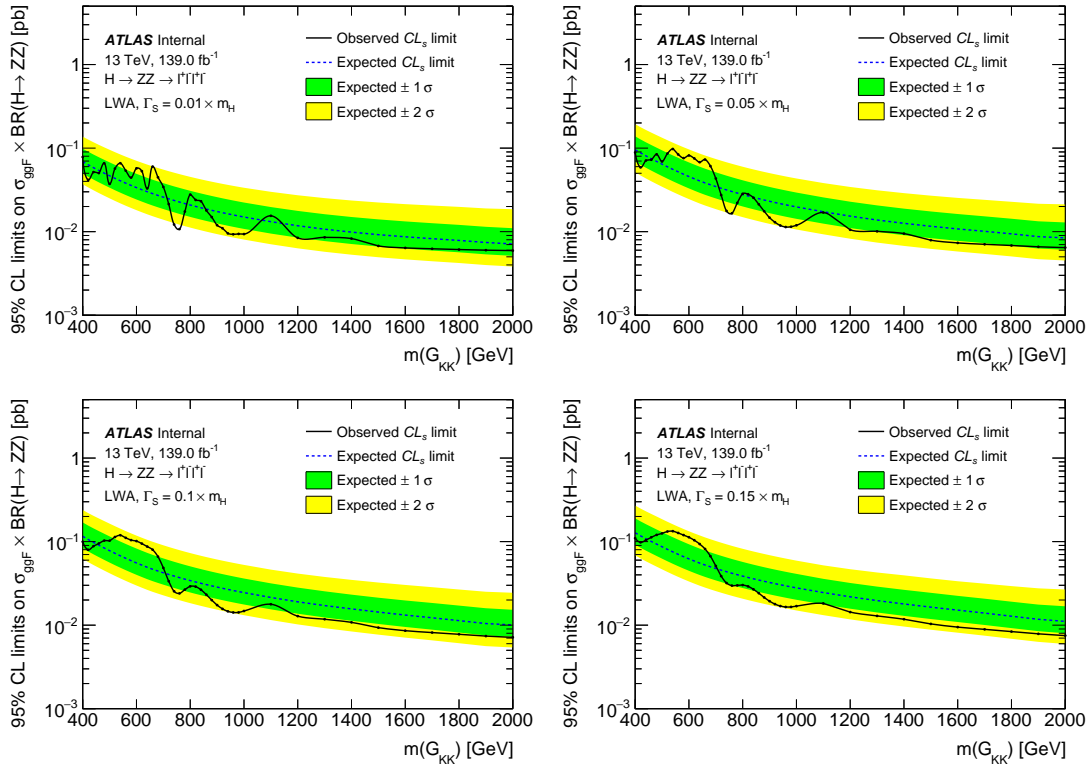


Fig. 6.31 The upper limits at 95% confidence level on $\sigma_{ggF} \times BR(H \rightarrow ZZ)$ as a function of the heavy resonance mass m_H for the ggF production mode with an intrinsic width of 1% (top left), 5% (top right), 10% (bottom left) and 15% (bottom right) for both the case where interference with Standard Model processes is considered. The green and yellow bands represent the $\pm 1\sigma$ and $\pm 2\sigma$ uncertainties in the expected limits.

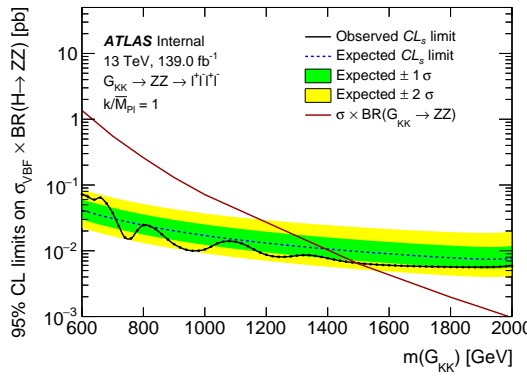


Fig. 6.32 The upper limits at 95% confidence level on $\sigma_{ggF} \times BR(G_{KK} \rightarrow ZZ)$ as a function of the heavy resonance mass $m(G_{KK})$ for the ggF production mode in RS Graviton model. The green and yellow bands represent the $\pm 1\sigma$ and $\pm 2\sigma$ uncertainties in the expected limits.

Table 6.10 A list of the experimental systematics considered in this analysis. The NPs have been separated by whether they only affect the normalisation (left column) or if they affect the shape (right column) of the $m_{4\ell}$ distribution. They are further subdivided into the primary objects that they affect.

Normalisation NPs	Shape NPs
Electrons	
EL_EFF_ID_CorrUncertaintyNP[0–15]	EG_RESOLUTION_ALL
EL_EFF_ID_SIMPLIFIED_UncorrUncertaintyNP[0–17]	EG_SCALE_ALLCORR
EL_EFF_Iso_TOTAL_1NPCOR_PLUS_UNCOR	EG_SCALE_E4SCINTILLATOR
EL_EFF_Reco_TOTAL_1NPCOR_PLUS_UNCOR	EG_SCALE_LARCALIB_EXTRA2015PRE
	EG_SCALE_LARTEMPERATURE_EXTRA2015PRE
	EG_SCALE_LARTEMPERATURE_EXTRA2016PRE
Muons	
MUON_EFF_ISO_STAT	MUON_ID
MUON_EFF_ISO_SYS	MUON_MS
MUON_EFF_RECO_STAT	MUON_SAGITTA_RESBIAS
MUON_EFF_RECO_STAT_LOWPT	MUON_SAGITTA_RHO
MUON_EFF_RECO_SYS	MUON_SCALE
MUON_EFF_RECO_SYS_LOWPT	
MUON_EFF_TTVA_STAT	
MUON_EFF_TTVA_SYS	
Jets	
	JET_BJES_Response
	JET_EffectiveNP_[1–7]
	JET_EffectiveNP_8restTerm
	JET_EtaIntercalibration_Modelling
	JET_EtaIntercalibration_NonClosure_highE
	JET_EtaIntercalibration_NonClosure_negEta
	JET_EtaIntercalibration_NonClosure_posEta
	JET_EtaIntercalibration_TotalStat
	JET_Flavor_Composition
	JET_Flavor_Response
	JET_JER_DataVsMC
	JET_JER_EffectiveNP_[1–6]
	JET_JER_EffectiveNP_7restTerm
	JET_Pileup_OffsetMu
	JET_Pileup_OffsetNPV
	JET_Pileup_PtTerm
	JET_Pileup_RhoTopology
	JET_PunchThrough_MC16
	JET_SingleParticle_HighPt
Other	
HOEW_QCD_syst	
HOEW_syst	
HOQCD_scale_syst	
PRW_DATASF	

Table 6.11 Expected and observed numbers of events for $m_{4\ell} > 200$ GeV, together with their uncertainties, for the VBF-enriched, ggF-enriched and the “rest” categories. The expected number of events, as well as their uncertainties, are obtained from a likelihood fit to the data under the background-only hypothesis.

Process	VBF-enriched category	ggF-enriched categories			rest category
		4μ channel	$2e2\mu$ channel	$4e$ channel	
$q\bar{q} \rightarrow ZZ$	10 ± 4	231 ± 10	387 ± 17	154 ± 7	2007 ± 47
$gg \rightarrow ZZ$	4 ± 2	38 ± 6	65 ± 11	26 ± 4	250 ± 19
ZZ (EW)	4.1 ± 0.4	4.5 ± 0.2	7.5 ± 0.4	3 ± 0.2	14.3 ± 0.7
$Z+jets/t\bar{t}/WZ$	0.08 ± 0.02	0.6 ± 0.1	1.7 ± 0.4	0.8 ± 0.1	8.8 ± 0
Other backgrounds	0.96 ± 0.03	9.8 ± 0.3	17.5 ± 0.4	7.7 ± 0.2	21.9 ± 0.5
Total background	19 ± 5	284 ± 12	478 ± 20	191 ± 8	2302 ± 51
Observed	19		955		2301

Table 6.12 $Z Z$ normalization factor in each category, obtained from a likelihood fit to the data under the background-only hypothesis.

Normalization factor	Fitted value
<code>muZZ_ggF</code>	1.07 ± 0.047
<code>muZZ_VBF</code>	0.91 ± 0.314
<code>muZZ_rest</code>	1.12 ± 0.026

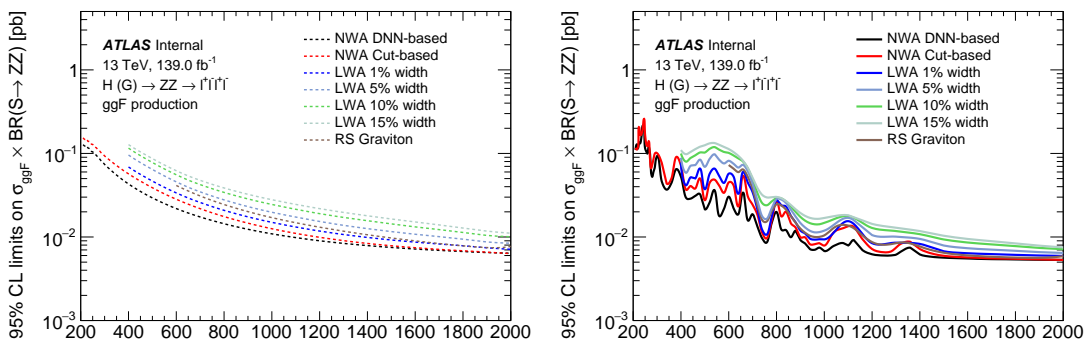


Fig. 6.33 The expected (left) and observed (right) upper limits at 95% confidence level on $\sigma \times BR(S \rightarrow ZZ)$ for ggF production mode at different assumptions.

6.8 Conclusion

A search of heavy resonances decaying into a pair of Z boson to $\ell\ell\ell\ell$ final state are performed using 139 fb^{-1} of 13 TeV pp collision data collected by ATLAS experiment at the LHC. The results are interpreted as 95% CL upper limits on the production cross section of a spin-0 or spin-2 resonance. The search range of the hypothetical resonances is between 200 GeV to 2000 GeV depending on the signal model. The spin-0 resonance is assumed to be a heavy *Higgs* like scalar dominantly from gluon–gluon fusion (ggF) and vector-boson fusion (VBF) decays, and it is studied under both the narrow-width approximation and with the large-width assumption. For narrow-width approximation, limits on cross section of heavy scalar decaying into two Z bosons are set separately for ggF and VBF production modes, under DNN- and cut- based analysis. In DNN-based analysis, the 95% CL upper limit range is from 210 fb at $m_H = 240$ GeV to 5.3 fb at $m_H = 2000$ GeV for ggF production mode, and from 87 fb at $m_H = 255$ GeV to 5.1 fb at $m_H = 1960$ GeV for VBF production mode. In cut-based analysis, the 95% CL upper limit range is from 259 fb at $m_H = 245$ GeV to 5.3 fb at $m_H = 2000$ GeV for ggF production mode, and from 113 fb at $m_H = 240$ GeV to 5.1 fb at $m_H = 2000$ GeV for VBF production mode. DNN-based analysis gains about 20% improvement on upper limits at lower mass region, while for mass above 1500 GeV, both analyses perform closely. For large-width approximation, limits are studied on ggF production rate at four different widths assumptions: 1%, 5%, 10% and 15% of resonance’s mass, with the interference between the heavy scalar and the SM Higgs boson as well as the heavy scalar and the SM $gg \rightarrow ZZ$ continuum background taken into account. The maximum and minimum of upper limits are obtained as 78 fb at $m_H = 400$ GeV to 5.9 fb at $m_H = 2000$ GeV for 1% width; 98 fb at $m_H = 540$ GeV to 6.4 fb at $m_H = 2000$ GeV for 5% width; 119 fb at $m_H = 540$ GeV to 7.1 fb at $m_H = 2000$ GeV for 10% width; 133 fb at $m_H = 540$ GeV to 7.5 fb at $m_H = 2000$ GeV for 15% width. Last but not least, the framework of the Randall–Sundrum model with a graviton excitation spin-2 resonance with $m(G_{KK}) < 1500$ GeV is excluded at 95% CL.

Bibliography

- [1] LANGACKER P. Introduction to the Standard Model and Electroweak Physics[C/OL]// Proceedings of Theoretical Advanced Study Institute in Elementary Particle Physics on The dawn of the LHC era (TASI 2008): Boulder, USA, June 2-27, 2008. 2010: 3-48. DOI: [10.1142/9789812838360_0001](https://doi.org/10.1142/9789812838360_0001).
- [2] PICH A. Electroweak Symmetry Breaking and the Higgs Boson[J/OL]. Acta Phys. Polon., 2016, B47:151. DOI: [10.5506/APhysPolB.47.151](https://doi.org/10.5506/APhysPolB.47.151).
- [3] DREMIN I M. Soft and hard processes in QCD[J/OL]. JETP Lett., 2005, 81:307-310. DOI: [10.1134/I.1944068](https://doi.org/10.1134/I.1944068).
- [4] WOMERSLEY J. QCD at the Tevatron: Status and prospects[C/OL]//Proceedings, 5th International Symposium on Radiative Corrections - RADCOR 2000. 2000. <http://www.slac.stanford.edu/econf/C000911/>.
- [5] LIN H W, et al. Parton distributions and lattice QCD calculations: a community white paper [J/OL]. Prog. Part. Nucl. Phys., 2018, 100:107-160. DOI: [10.1016/j.ppnp.2018.01.007](https://doi.org/10.1016/j.ppnp.2018.01.007).
- [6] COLLINS J C, SOPER D E, STERMAN G F. Factorization of Hard Processes in QCD[J/OL]. Adv. Ser. Direct. High Energy Phys., 1989, 5:1-91. DOI: [10.1142/9789814503266_0001](https://doi.org/10.1142/9789814503266_0001).
- [7] STIRLING W J. Perturbative QCD[J/OL]. 2000(CERN-OPEN-2000-296):40 p. <https://cds.cern.ch/record/1194745>. DOI: [10.5170/CERN-2000-007.305](https://doi.org/10.5170/CERN-2000-007.305).
- [8] GROJEAN C. Higgs Physics[J/OL]. 2017(arXiv:1708.00794):143-158. 12 p. <https://cds.cern.ch/record/2243593>. DOI: [10.5170/CERN-2016-005.143](https://doi.org/10.5170/CERN-2016-005.143).
- [9] Cern yellow reports: Monographs: Handbook of LHC Higgs Cross Sections: 4. Deciphering the Nature of the Higgs Sector[M/OL]. 2016. <https://cds.cern.ch/record/2227475>. DOI: [10.23731/CYRM-2017-002](https://doi.org/10.23731/CYRM-2017-002).
- [10] HEINEMEYER S. Cern yellow reports: Monographs: Handbook of LHC Higgs Cross Sections: 3. Higgs Properties: Report of the LHC Higgs Cross Section Working Group[M/OL]. 2013. <https://cds.cern.ch/record/1559921>. DOI: [10.5170/CERN-2013-004](https://doi.org/10.5170/CERN-2013-004).
- [11] CHANG J, CHEUNG K, LU C T, et al. ww scattering in the era of post-higgs-boson discovery [J/OL]. Phys. Rev. D, 2013, 87:093005. <https://link.aps.org/doi/10.1103/PhysRevD.87.093005>.
- [12] BRUNING O S, COLLIER P, LEBRUN P, et al. LHC Design Report Vol.1: The LHC Main Ring[J]. 2004.
- [13] BUNING O, COLLIER P, LEBRUN P, et al. LHC Design Report. 2. The LHC infrastructure and general services[J]. 2004.
- [14] BENEDIKT M, COLLIER P, MERTENS V, et al. LHC Design Report. 3. The LHC injector

- chain[J]. 2004.
- [15] EVANS L, BRYANT P. LHC machine[J/OL]. Journal of Instrumentation, 2008, 3(08):S08001-S08001. <https://doi.org/10.1088%2F1748-0221%2F3%2F08%2Fs08001>. DOI: [10.1088/1748-0221/3/08/s08001](https://doi.org/10.1088/1748-0221/3/08/s08001).
- [16] MOBS E. The CERN accelerator complex. Complexe des accélérateurs du CERN[J/OL]. 2016. <https://cds.cern.ch/record/2197559>.
- [17] COLLABORATION A. The ATLAS experiment at the CERN large hadron collider[J/OL]. Journal of Instrumentation, 2008, 3(08):S08003-S08003. <https://doi.org/10.1088%2F1748-0221%2F3%2F08%2Fs08003>. DOI: [10.1088/1748-0221/3/08/s08003](https://doi.org/10.1088/1748-0221/3/08/s08003).
- [18] PEREZ G. Unitarization models for vector boson scattering at the lhc[D/OL]. 2018. DOI: [10.5445/IR/1000082199](https://doi.org/10.5445/IR/1000082199).
- [19] PEQUENAO J. Computer generated image of the whole ATLAS detector[Z/OL]. 2008. <https://cds.cern.ch/record/1095924>.
- [20] MCFAYDEN J. The lhc and atlas detector. in: Third generation susy and $t\bar{t} + z$ productin. [D/OL]. 2014. DOI: [10.1007/978-3-319-07191-6_2](https://doi.org/10.1007/978-3-319-07191-6_2).
- [21] COLLABRATION A. Operation and performance of the ATLAS semiconductor tracker. Operation and performance of the ATLAS semiconductor tracker[J/OL]. JINST, 2014, 9(CERN-PH-EP-2014-049. CERN-PH-EP-2014-049):P08009. 80 p. <https://cds.cern.ch/record/1698966>. DOI: [10.1088/1748-0221/9/08/P08009](https://doi.org/10.1088/1748-0221/9/08/P08009).
- [22] MULLIER G. The upgraded pixel detector of the atlas experiment for run-2 at the large hadron collider[J/OL]. Journal of Instrumentation, 2016, 11:C02061-C02061. DOI: [10.1088/1748-0221/11/02/C02061](https://doi.org/10.1088/1748-0221/11/02/C02061).
- [23] SULTAN D M S. Development of small-pitch, thin 3d sensors for pixel detector upgrades at hl-lhc[D/OL]. 2017. DOI: [10.13140/RG.2.2.36253.82403/1](https://doi.org/10.13140/RG.2.2.36253.82403/1).
- [24] The ATLAS transition radiation tracker (TRT) proportional drift tube: design and performance [J/OL]. Journal of Instrumentation, 2008, 3(02):P02013-P02013. <https://doi.org/10.1088%2F1748-0221%2F3%2F02%2Fp02013>. DOI: [10.1088/1748-0221/3/02/p02013](https://doi.org/10.1088/1748-0221/3/02/p02013).
- [25] BUCHANAN N, CHEN L, GINGRICH D, et al. Design and implementation of the front end board for the readout of the atlas liquid argon calorimeters[J/OL]. Journal of Instrumentation, 2008, 3:P03004. DOI: [10.1088/1748-0221/3/03/P03004](https://doi.org/10.1088/1748-0221/3/03/P03004).
- [26] Technical design report atlas: ATLAS liquid-argon calorimeter: Technical Design Report [M/OL]. Geneva: CERN, 1996. <https://cds.cern.ch/record/331061>.
- [27] AAD G, ABBOTT B, ABDALLAH J, et al. Readiness of the atlas tile calorimeter for lhc collisions[J]. European Physical Journal C, 2010.
- [28] SLIWA K. "ATLAS Overview and Main Results"[C]//Proceedings, International School on

- High Energy Physics : Workshop on High Energy Physics in the near Future. (LISHEP 2013): Rio de Janeiro, Brazil, March 17-24, 2013. 2013.
- [29] RUIZ-MARTINEZ A, COLLABORATION A. The Run-2 ATLAS Trigger System: ATL-DAQ-PROC-2016-003[R/OL]. Geneva: CERN, 2016. <https://cds.cern.ch/record/2133909>. DOI: [10.1088/1742-6596/762/1/012003](https://doi.org/10.1088/1742-6596/762/1/012003).
- [30] PÁSZTOR G. The Upgrade of the ATLAS Electron and Photon Triggers towards LHC Run 2 and their Performance: ATL-DAQ-PROC-2015-053. arXiv:1511.00334[R/OL]. Geneva: CERN, 2015. <https://cds.cern.ch/record/2063746>.
- [31] COLLABORATION A. Atlas computing: Technical design report[R/OL]. Geneva: CERN. <http://atlas-computing.web.cern.ch/atlas-computing/packages/athenaCore/athenaCore.php>.
- [32] AAD G, et al. The ATLAS Simulation Infrastructure[J/OL]. Eur. Phys. J., 2010, C70:823-874. DOI: [10.1140/epjc/s10052-010-1429-9](https://doi.org/10.1140/epjc/s10052-010-1429-9).
- [33] HOCHE S. Introduction to parton-shower event generators[C/OL]//Proceedings, Theoretical Advanced Study Institute in Elementary Particle Physics: Journeys Through the Precision Frontier: Amplitudes for Colliders (TASI 2014): Boulder, Colorado, June 2-27, 2014. 2015: 235-295. DOI: [10.1142/9789814678766_0005](https://doi.org/10.1142/9789814678766_0005).
- [34] GLEISBERG T, HöCHE S, KRAUSS F, et al. Event generation with SHERPA 1.1[J/OL]. Journal of High Energy Physics, 2009, 2009(02):007-007. <https://doi.org/10.1088%2F1126-6708%2F2009%2F02%2F007>. DOI: [10.1088/1126-6708/2009/02/007](https://doi.org/10.1088/1126-6708/2009/02/007).
- [35] BÄHR M, GIESEKE S, GIGG M A, et al. Herwig++ physics and manual[J/OL]. The European Physical Journal C, 2008, 58(4):639-707. <https://doi.org/10.1140/epjc/s10052-008-0798-9>.
- [36] NASON P. A New method for combining NLO QCD with shower Monte Carlo algorithms [J/OL]. JHEP, 2004, 11:040. DOI: [10.1088/1126-6708/2004/11/040](https://doi.org/10.1088/1126-6708/2004/11/040).
- [37] FRIXIONE S, WEBBER B R. Matching NLO QCD computations and parton shower simulations[J/OL]. Journal of High Energy Physics, 2002, 2002(06):029-029. <https://doi.org/10.1088%2F1126-6708%2F2002%2F06%2F029>. DOI: [10.1088/1126-6708/2002/06/029](https://doi.org/10.1088/1126-6708/2002/06/029).
- [38] SJOSTRAND T, MRENNA S, SKANDS P Z. A Brief Introduction to PYTHIA 8.1[J/OL]. Comput. Phys. Commun., 2008, 178:852-867. DOI: [10.1016/j.cpc.2008.01.036](https://doi.org/10.1016/j.cpc.2008.01.036).
- [39] BARBERIO E, et al. The Geant4-Based ATLAS Fast Electromagnetic Shower Simulation [C/OL]//Astroparticle, particle and space physics, detectors and medical physics applications. Proceedings, 10th Conference, ICATPP 2007, Como, Italy, October 8-12, 2007. 2008: 802-806. <http://cdsweb.cern.ch/record/1064665/files/soft-conf-2007-002.pdf>. DOI: [10.1142/9789812819093_0133](https://doi.org/10.1142/9789812819093_0133).
- [40] RICHTER-WAS E, FROIDEVAUX D, POGGIOLI L. ATLFAST 2.0 a fast simulation package for ATLAS: ATL-PHYS-98-131[R/OL]. Geneva: CERN, 1998. <https://cds.cern.ch/record/683>

- 751.
- [41] EDMONDS K, FLEISCHMANN S, LENZ T, et al. The Fast ATLAS Track Simulation (FATRAS): ATL-SOFT-PUB-2008-001. ATL-COM-SOFT-2008-002[R/OL]. Geneva: CERN, 2008. <https://cds.cern.ch/record/1091969>.
 - [42] BOYD J T, COSTA M J, TONOVAN A, et al. Commissioning of the ATLAS reconstruction software with first data[J/OL]. Journal of Physics: Conference Series, 2010, 219(3):032059. <https://doi.org/10.1088%2F1742-6596%2F219%2F3%2F032059>. DOI: [10.1088/1742-6596/219/3/032059](https://doi.org/10.1088/1742-6596/219/3/032059).
 - [43] CORNELISSEN T, ELSING M, FLEISCHMANN S, et al. Concepts, Design and Implementation of the ATLAS New Tracking (NEWT): ATL-SOFT-PUB-2007-007. ATL-COM-SOFT-2007-002[R/OL]. Geneva: CERN, 2007. <https://cds.cern.ch/record/1020106>.
 - [44] AAD G, et al. Muon reconstruction performance of the ATLAS detector in proton-proton collision data at $\sqrt{s} = 13$ TeV[J/OL]. Eur. Phys. J., 2016, C76(5):292. DOI: [10.1140/epjc/s10052-016-4120-y](https://doi.org/10.1140/epjc/s10052-016-4120-y).
 - [45] ILLINGWORTH J, KITTLER J. A survey of the hough transform[J/OL]. Computer Vision, Graphics, and Image Processing, 1988, 44(1):87 - 116. <http://www.sciencedirect.com/science/article/pii/S0734189X88800331>. DOI: [https://doi.org/10.1016/S0734-189X\(88\)80033-1](https://doi.org/10.1016/S0734-189X(88)80033-1).
 - [46] Vertex Reconstruction Performance of the ATLAS Detector at 13 TeV: ATL-PHYS-PUB-2015-026[R/OL]. Geneva: CERN, 2015. <https://cds.cern.ch/record/2037717>.
 - [47] AABOUD M, et al. Reconstruction of primary vertices at the ATLAS experiment in Run 1 proton-proton collisions at the LHC[J/OL]. Eur. Phys. J., 2017, C77(5):332. DOI: [10.1140/epjc/s10052-017-4887-5](https://doi.org/10.1140/epjc/s10052-017-4887-5).
 - [48] Electron efficiency measurements with the ATLAS detector using the 2015 LHC proton-proton collision data: ATLAS-CONF-2016-024[R/OL]. Geneva: CERN, 2016. <https://cds.cern.ch/record/2157687>.
 - [49] LAMPL W, LAPLACE S, LELAS D, et al. Calorimeter Clustering Algorithms: Description and Performance: ATL-LARG-PUB-2008-002. ATL-COM-LARG-2008-003[R/OL]. Geneva: CERN, 2008. <https://cds.cern.ch/record/1099735>.
 - [50] CORNELISSEN T G, ELSING M, GAVRILENKO I, et al. The global χ^2 track fitter in ATLAS [J/OL]. Journal of Physics: Conference Series, 2008, 119(3):032013. <https://doi.org/10.1088%2F1742-6596%2F119%2F3%2F032013>. DOI: [10.1088/1742-6596/119/3/032013](https://doi.org/10.1088/1742-6596/119/3/032013).
 - [51] Electron efficiency measurements with the ATLAS detector using the 2012 LHC proton-proton collision data: ATLAS-CONF-2014-032[R/OL]. Geneva: CERN, 2014. <http://cds.cern.ch/record/1706245>.
 - [52] LIMPER M. Track and vertex reconstruction in the ATLAS inner detector[D/OL]. 2009. <http://cds.cern.ch/record/1091969>.

- //cds.cern.ch/record/1202457.
- [53] AAD G, et al. Topological cell clustering in the ATLAS calorimeters and its performance in LHC Run 1[J/OL]. *Eur. Phys. J.*, 2017, C77:490. DOI: [10.1140/epjc/s10052-017-5004-5](https://doi.org/10.1140/epjc/s10052-017-5004-5).
- [54] ZHENG Z. Identification of very-low transverse momentum muons with the ATLAS experiment: ATL-MUON-PROC-2018-018[R/OL]. Geneva: CERN, 2018. <https://cds.cern.ch/record/2649299>.
- [55] CACCIARI M, SALAM G P. Pileup subtraction using jet areas[J/OL]. *Physics Letters B*, 2008, 659(1):119 - 126. <http://www.sciencedirect.com/science/article/pii/S0370269307011094>. DOI: <https://doi.org/10.1016/j.physletb.2007.09.077>.
- [56] CACCIARI M, SALAM G P, SOYEZ G. The anti-k_Tjet clustering algorithm[J/OL]. *Journal of High Energy Physics*, 2008, 2008(04):063-063. <https://doi.org/10.1088%2F1126-6708%2F2008%2F04%2F063>. DOI: [10.1088/1126-6708/2008/04/063](https://doi.org/10.1088/1126-6708/2008/04/063).
- [57] CACCIARI M, SALAM G P, SOYEZ G. Fastjet user manual[J/OL]. *The European Physical Journal C*, 2012, 72(3):1896. <https://doi.org/10.1140/epjc/s10052-012-1896-2>.
- [58] AAD G, et al. Jet energy measurement and its systematic uncertainty in proton-proton collisions at $\sqrt{s} = 7$ TeV with the ATLAS detector[J/OL]. *Eur. Phys. J.*, 2015, C75:17. DOI: [10.1140/epjc/s10052-014-3190-y](https://doi.org/10.1140/epjc/s10052-014-3190-y).
- [59] AABOUD M, et al. Jet energy scale measurements and their systematic uncertainties in proton-proton collisions at $\sqrt{s} = 13$ TeV with the ATLAS detector[J/OL]. *Phys. Rev.*, 2017, D96(7): 072002. DOI: [10.1103/PhysRevD.96.072002](https://doi.org/10.1103/PhysRevD.96.072002).
- [60] Optimisation of the ATLAS *b*-tagging performance for the 2016 LHC Run: ATL-PHYS-PUB-2016-012[R/OL]. Geneva: CERN, 2016. <https://cds.cern.ch/record/2160731>.
- [61] PIACQUADIO G, WEISER C. A new inclusive secondary vertex algorithm for *b*-jet tagging in ATLAS[J/OL]. *Journal of Physics: Conference Series*, 2008, 119(3):032032. <https://doi.org/10.1088%2F1742-6596%2F119%2F3%2F032032>. DOI: [10.1088/1742-6596/119/3/032032](https://doi.org/10.1088/1742-6596/119/3/032032).
- [62] SPECKMAYER P, HöCKER A, STELZER J, et al. The toolkit for multivariate data analysis, TMVA 4[J/OL]. *Journal of Physics: Conference Series*, 2010, 219(3):032057. <https://doi.org/10.1088%2F1742-6596%2F219%2F3%2F032057>. DOI: [10.1088/1742-6596/219/3/032057](https://doi.org/10.1088/1742-6596/219/3/032057).
- [63] Performance of missing transverse momentum reconstruction with the atlas detector using proton–proton collisions at $\sqrt{s}=13$ TeV[J/OL]. *The European Physical Journal C*, 2018, 78(11):903. <https://doi.org/10.1140/epjc/s10052-018-6288-9>.
- [64] Observation of a new particle in the search for the standard model higgs boson with the atlas detector at the lhc[J/OL]. *Physics Letters B*, 2012, 716(1):1 - 29. <http://www.sciencedirect.com/science/article/pii/S037026931200857X>. DOI: <https://doi.org/10.1016/j.physletb.2012.08.020>.
- [65] Observation of a new boson at a mass of 125 gev with the cms experiment at the lhc[J/OL].

- Physics Letters B, 2012, 716(1):30 - 61. <http://www.sciencedirect.com/science/article/pii/S0370269312008581>. DOI: <https://doi.org/10.1016/j.physletb.2012.08.021>.
- [66] LEE B W, QUIGG C, THACKER H B. The Strength of Weak Interactions at Very High-Energies and the Higgs Boson Mass[J/OL]. Phys. Rev. Lett., 1977, 38:883-885. DOI: [10.1103/PhysRevLett.38.883](https://doi.org/10.1103/PhysRevLett.38.883).
- [67] CHANOWITZ M S, GAILLARD M K. The TeV Physics of Strongly Interacting W's and Z's [J/OL]. Nucl. Phys., 1985, B261:379-431. DOI: [10.1016/0550-3213\(85\)90580-2](https://doi.org/10.1016/0550-3213(85)90580-2).
- [68] SZLEPER M. The Higgs boson and the physics of WW scattering before and after Higgs discovery[J]. 2014.
- [69] Evidence for electroweak production of $W^\pm W^\pm jj$ in pp collisions at $\sqrt{s} = 8$ TeV with the atlas detector[J/OL]. Phys. Rev. Lett., 2014, 113:141803. <https://link.aps.org/doi/10.1103/PhysRevLett.113.141803>.
- [70] Observation of electroweak production of a same-sign w boson pair in association with two jets in pp collisions at $\sqrt{s} = 13$ TeV with the atlas detector[J/OL]. Phys. Rev. Lett., 2019, 123: 161801. <https://link.aps.org/doi/10.1103/PhysRevLett.123.161801>.
- [71] SIRUNYAN A M, et al. Observation of electroweak production of same-sign W boson pairs in the two jet and two same-sign lepton final state in proton-proton collisions at $\sqrt{s} = 13$ TeV [J/OL]. Phys. Rev. Lett., 2018, 120(8):081801. DOI: [10.1103/PhysRevLett.120.081801](https://doi.org/10.1103/PhysRevLett.120.081801).
- [72] Observation of electroweak $w\pm z$ boson pair production in association with two jets in pp collisions at $s=13$ tev with the atlas detector[J/OL]. Physics Letters B, 2019, 793:469 - 492. <http://www.sciencedirect.com/science/article/pii/S0370269319303211>. DOI: <https://doi.org/10.1016/j.physletb.2019.05.012>.
- [73] Measurement of vector boson scattering and constraints on anomalous quartic couplings from events with four leptons and two jets in proton–proton collisions at $s=13$ tev[J/OL]. Physics Letters B, 2017, 774:682 - 705. <http://www.sciencedirect.com/science/article/pii/S0370269317308328>. DOI: <https://doi.org/10.1016/j.physletb.2017.10.020>.
- [74] ALWALL J, FREDERIX R, FRIXIONE S, et al. The automated computation of tree-level and next-to-leading order differential cross sections, and their matching to parton shower simulations[J/OL]. JHEP, 2014, 07:079. DOI: [10.1007/JHEP07\(2014\)079](https://doi.org/10.1007/JHEP07(2014)079).
- [75] BALL R D, et al. Parton distributions with LHC data[J/OL]. Nucl. Phys. B, 2013, 867:244-289. DOI: [10.1016/j.nuclphysb.2012.10.003](https://doi.org/10.1016/j.nuclphysb.2012.10.003).
- [76] GLEISBERG T, HÖCHE S, KRAUSS F, et al. Event generation with SHERPA 1.1[J/OL]. JHEP, 2009, 02:007. DOI: [10.1088/1126-6708/2009/02/007](https://doi.org/10.1088/1126-6708/2009/02/007).
- [77] BALL R D, et al. Parton distributions for the LHC run II[J/OL]. JHEP, 2015, 04:040. DOI: [10.1007/JHEP04\(2015\)040](https://doi.org/10.1007/JHEP04(2015)040).

Bibliography

- [78] CAOLA F, MELNIKOV K, RÖNTSCH R, et al. Qcd corrections to zz production in gluon fusion at the lhc[J/OL]. Phys. Rev. D, 2015, 92:094028. <https://link.aps.org/doi/10.1103/PhysRevD.92.094028>.
- [79] FRIXIONE S, RIDOLFI G, NASON P. A positive-weight next-to-leading-order Monte Carlo for heavy flavour hadroproduction[J/OL]. JHEP, 2007, 09:126. DOI: [10.1088/1126-6708/2007/09/126](https://doi.org/10.1088/1126-6708/2007/09/126).
- [80] LAI H L, et al. New parton distributions for collider physics[J/OL]. Phys. Rev. D, 2010, 82: 074024. DOI: [10.1103/PhysRevD.82.074024](https://doi.org/10.1103/PhysRevD.82.074024).
- [81] ALIOLI S, NASON P, OLEARI C, et al. NLO single-top production matched with shower in POWHEG: s- and t-channel contributions[J/OL]. JHEP, 2009, 09:111. DOI: [10.1088/1126-6708/2009/09/111](https://doi.org/10.1088/1126-6708/2009/09/111).
- [82] FREDERIX R, RE E, TORRIELLI P. Single-top t-channel hadroproduction in the four-flavour scheme with POWHEG and aMC@NLO[J/OL]. JHEP, 2012, 09:130. DOI: [10.1007/JHEP09\(2012\)130](https://doi.org/10.1007/JHEP09(2012)130).
- [83] RE E. Single-top Wt-channel production matched with parton showers using the POWHEG method[J/OL]. Eur. Phys. J. C, 2011, 71:1547. DOI: [10.1140/epjc/s10052-011-1547-z](https://doi.org/10.1140/epjc/s10052-011-1547-z).
- [84] COLLABORATION A. ATLAS Pythia 8 tunes to 7 TeV data[M/OL]. 2014. <https://cds.cern.ch/record/1966419>.
- [85] ATLAS Collaboration. Performance of pile-up mitigation techniques for jets in pp collisions at $\sqrt{s} = 8$ TeV using the ATLAS detector[J/OL]. Eur. Phys. J. C, 2016, 76:581. DOI: [10.1140/epjc/s10052-016-4395-z](https://doi.org/10.1140/epjc/s10052-016-4395-z).
- [86] BELLM J, et al. Herwig 7.0/Herwig++ 3.0 release note[J/OL]. Eur. Phys. J. C, 2016, 76(4): 196. DOI: [10.1140/epjc/s10052-016-4018-8](https://doi.org/10.1140/epjc/s10052-016-4018-8).
- [87] BAHR M, et al. Herwig++ Physics and Manual[J/OL]. Eur. Phys. J. C, 2008, 58:639-707. DOI: [10.1140/epjc/s10052-008-0798-9](https://doi.org/10.1140/epjc/s10052-008-0798-9).
- [88] Luminosity determination in pp collisions at $\sqrt{s} = 13$ TeV using the ATLAS detector at the LHC: ATLAS-CONF-2019-021[R/OL]. Geneva: CERN, 2019. <http://cds.cern.ch/record/2677054>.
- [89] The new LUCID-2 detector for luminosity measurement and monitoring in ATLAS[J/OL]. Journal of Instrumentation, 2018, 13(07):P07017-P07017. <https://doi.org/10.1088%2F1748-0221%2F13%2F07%2Fp07017>. DOI: [10.1088/1748-0221/13/07/p07017](https://doi.org/10.1088/1748-0221/13/07/p07017).
- [90] COADOU Y. Boosted decision trees and applications[J/OL]. EPJ Web of Conferences, 2013, 55:02004-. DOI: [10.1051/epjconf/20135502004](https://doi.org/10.1051/epjconf/20135502004).
- [91] COLLABORATION T A. Observation of electroweak production of two jets in association with a Z -boson pair in pp collisions at $\sqrt{s} = 13$ TeV with the ATLAS detector[J]. 2019.

- [92] COLLABORATION A. Technical Design Report for the ATLAS Inner Tracker Pixel Detector: CERN-LHCC-2017-021. ATLAS-TDR-030[R/OL]. Geneva: CERN, 2017. <https://cds.cern.ch/record/2285585>.
- [93] COLLABORATION A. Technical Design Report for the Phase-II Upgrade of the ATLAS Muon Spectrometer: CERN-LHCC-2017-017. ATLAS-TDR-026[R/OL]. Geneva: CERN, 2017. <https://cds.cern.ch/record/2285580>.
- [94] COLLABORATION A. Technical Proposal: A High-Granularity Timing Detector for the ATLAS Phase-II Upgrade: CERN-LHCC-2018-023. LHCC-P-012[R/OL]. Geneva: CERN, 2018. <https://cds.cern.ch/record/2623663>.
- [95] Expected performance for an upgraded ATLAS detector at High-Luminosity LHC: ATL-PHYS-PUB-2016-026[R/OL]. Geneva: CERN, 2016. <https://cds.cern.ch/record/2223839>.
- [96] HILL A, VAN DER BIJ J J. Strongly interacting singlet-doublet higgs model[J/OL]. Phys. Rev. D, 1987, 36:3463-3473. <https://link.aps.org/doi/10.1103/PhysRevD.36.3463>.
- [97] BRANCO G, FERREIRA P, LAVOURA L, et al. Theory and phenomenology of two-higgs-doublet models[J/OL]. Physics Reports, 2012, 516(1):1 - 102. <http://www.sciencedirect.com/science/article/pii/S0370157312000695>. DOI: <https://doi.org/10.1016/j.physrep.2012.02.002>.
- [98] DAVOUDIASL H, HEWETT J, RIZZO T. Bulk gauge fields in the randall–sundrum model1work supported by the department of energy, contract de-ac03-76sf00515.1[J/OL]. Physics Letters B, 2000, 473(1):43 - 49. <http://www.sciencedirect.com/science/article/pii/S0370269399014306>. DOI: [https://doi.org/10.1016/S0370-2693\(99\)01430-6](https://doi.org/10.1016/S0370-2693(99)01430-6).
- [99] FREDERIX R, FRIXIONE S. Merging meets matching in MC@NLO[J/OL]. JHEP, 2012, 12: 061. DOI: [10.1007/JHEP12\(2012\)061](10.1007/JHEP12(2012)061).
- [100] AGASHE K, DAVOUDIASL H, PEREZ G, et al. Warped Gravitons at the LHC and Beyond [J/OL]. Phys.Rev., 2007, D76:036006. DOI: <10.1103/PhysRevD.76.036006>.
- [101] ATLAS Collaboration. Jet reconstruction and performance using particle flow with the ATLAS Detector[J/OL]. Eur. Phys. J. C, 2017, 77:466. DOI: <10.1140/epjc/s10052-017-5031-2>.
- [102] Measurements of higgs boson production and couplings in the four-lepton channel in pp collisions at center-of-mass energies of 7 and 8 tev with the atlas detector[J/OL]. Phys. Rev. D, 2015, 91:012006. <https://link.aps.org/doi/10.1103/PhysRevD.91.012006>.
- [103] CRANMER K S. Kernel estimation in high-energy physics[J/OL]. Comput. Phys. Commun., 2001, 136:198-207. DOI: [10.1016/S0010-4655\(00\)00243-5](10.1016/S0010-4655(00)00243-5).
- [104] OREGLIA M. A Study of the Reactions $\psi' \rightarrow \gamma\gamma\psi$ [M/OL]. SLAC, 1980. <https://www.slac.stanford.edu/cgi-wrap/getdoc/slac-r-236.pdf>.
- [105] GAISER J. Charmonium Spectroscopy From Radiative Decays of the J/ψ and ψ' [M/OL]. SLAC, 1982. <https://www.slac.stanford.edu/cgi-wrap/getdoc/slac-r-255.pdf>.

Bibliography

- [106] GORIA S, PASSARINO G, ROSCO D. The Higgs Boson Lineshape[J/OL]. Nucl.Phys., 2012, B864:530-579. DOI: [10.1016/j.nuclphysb.2012.07.006](https://doi.org/10.1016/j.nuclphysb.2012.07.006).
- [107] SPIRA M, DJOUADI A, GRAUDENZ D, et al. Higgs boson production at the LHC[J]. Nucl. Phys., 1995, B 453:17-82.
- [108] BALL R D, et al. Parton Distribution Benchmarking with LHC Data[J/OL]. JHEP, 2013, 04: 125. DOI: [10.1007/JHEP04\(2013\)125](https://doi.org/10.1007/JHEP04(2013)125).
- [109] BIJNENS J, EEROLA P, MAUL M, et al. Qcd signatures of narrow graviton resonances in hadron colliders[J/OL]. Physics Letters B, 2001, 503(3-4):341-348. DOI: [10.1016/s0370-2693\(01\)00238-6](https://doi.org/10.1016/s0370-2693(01)00238-6).
- [110] ATLAS Collaboration. PMG Systematic Uncertainty Recipes[EB/OL]. <https://twiki.cern.ch/twiki/bin/view/AtlasProtected/PmgSystematicUncertaintyRecipes>.
- [111] READ A L. Presentation of search results: The CL(s) technique[J]. J. Phys. G, 2002, 28: 2693-2704.